Simulation of Rapidly Varying and Dry Bed Flow using the Serre equations solved by a Finite Element Volume Method.

Jordan Peter Anthony Pitt

January 2019

A thesis submitted for the degree of Doctor of Philosophy
of the Australian National University

To my mother and father who have provided me with everything.

Declaration

The work in this thesis is my own except where otherwise stated.

Jordan Peter Anthony Pitt

Acknowledgements

I would like to thank my lead supervisor Professor Stephen Roberts for his insight, suggestions and time spent improving my research. Dr Chris Zoppou who put a tremendous amount of time and effort into reading and editing my work. The remainder of my supervisory panel Professor Markus Hegland and Professor John Urbas.

I would also like to thank our fellow researchers who provided us with experimental data:

- Dr David George, Cascades Volcano Observatory, U.S. Geological Survey for providing the digitised data for the negative rectangular wave experiment.
- Professor Sedar Beji, Department of Naval Architecture and Ocean Engineering, Istanbul Technical University for providing the data for the periodic waves over a submerged bar experiment.
- Dr Volker Roeber, Department of Physical Oceanography, University of Hawai'i at Mānoa for providing the data for the solitary wave over a fringing reef experiment.

Finally, I would like to thank my dear friend Joseph Gibson who donated a computer that hosted many numerical experiments.

Abstract

Recent research in numerical wave modelling has focused on developing computational methods for solving non-linear, dispersive wave equations as an extension to methods solving the non-linear shallow water wave equations. These equations contain extra terms that allow for dispersion; improving its modelling capabilities for water waves. An interesting example of these non-linear dispersive equations for modelling water waves are the Serre equations.

In this work an efficient and robust numerical method for the one-dimensional Serre equations was developed. This method uses a finite element method to solve an elliptic equation and a finite volume method to solve the remaining conservation equations and is hence termed the Finite Element Volume Method (FEVM). The use of a finite element method and a finite volume method makes the FEVM adaptable to unstructured meshes and parrallelisable. The FEVM allows for the recovery of the lake at rest steady state and the simulation of flow over dry beds.

The convergence and dispersion properties of the FEVM was determined using a linear analysis. The FEVM was validated against analytic and forced solutions of the Serre equations, demonstrating its convergence properties. Finally, it was validated against experimental data for a wide array of physical scenarios, establishing its utility as a realistic model.

All these analyses and validations were also conducted on other methods allowing comparisons between them and the FEVM. Overall the FEVM was found to be the most robust whilst being adequately accurate and is therefore, the recommended approach for solving the Serre equations.

Contents

Chapter 1

Introduction

A significant portion of the world's people and critical infrastructure is located near the coast. While the ocean provides many opportunities it also poses significant hazards from tsunamis and storm surges. Furthermore, the dynamics of ocean waves significantly impacts our understanding of other physical phenomena; such as the break-up of sea-ice and the erosion of beaches. Therefore, accurate modelling of ocean waves is important to our society.

The physics of water can be described using Newton's second law. From which the partial differential equations initially presented by Euler in 1757 [1] can be derived. The Euler equations were then extended to include viscosity, producing the full Navier-Stokes equations [2, 3]. Numerical methods [4, 5, 6] have been developed to solve the Euler equations; however due to their complexity these methods can only accurately resolve fluid behaviour over small scales and not the scales required to model tsunamis along a coastline.

For this reason the central focus of water wave modelling has been simplified water wave theories that approximate the behaviour of the free surface of water governed by the Euler equations. The most popular class of these approximate water wave theories are the shallow water wave theories where the characteristic water depth h_0 is far smaller than the characteristic wave length λ_0, so that $\sigma = h_0/\lambda_0 \ll 1$. For tsunamis and storm surges h_0 is typically $4km$ far from the coastline and λ_0 can be $100km$ and so $\sigma \ll 1$.

Neglecting all terms of order $\mathcal{O}(\sigma^2)$ the full Euler equations reduce to the Shallow Water Wave Equations (SWWE) [7] which describe fully non-linear non-dispersive waves. Retaining higher powers of σ leads to a class of equations known as 'Boussinesq-type' equations. Boussinesq-type equations are then classified by the powers of σ they retain and their retained non-linearity; which is based on

the size of $\epsilon = a_0/h_0$ which compares the characteristic amplitude of the waves a_0 to the water depth h_0. These wave models form a spectrum with the SWWE being the simplest and most restrictive model and the Boussinesq-type models retaining the highest powers of σ and largest ϵ being the most complex and least restrictive. The Serre equations are one particular Boussinesq-type equation that retains all terms of order $\mathcal{O}(\sigma^4)$ and makes no assumption on the size of ϵ [7]. This allows the Serre equations to model water waves better than the SWWE in intermediate water depths where σ^2 terms can be significant but σ^4 terms are not. These intermediate water depths tend to occur as tsunamis and storm surges approach the coastline and interact with the varying bathymetry. Since the Serre equations allow arbitrary wave height they are the most appropriate model for water waves for the $\mathcal{O}(\sigma^4)$ class of Boussinesq-type equations.

There has previously been a significant amount of research into developing large scale, efficient and robust computational methods for the SWWE [8, 9, 10]. The SWWE neglect all terms of order $\mathcal{O}(\sigma^2)$ in the Euler equations and so do not capture all water wave behaviour; in particular dispersion. Recent research has highlighted the need for dispersive wave models for the evolution of tsunamis [11, 12]. For the purposes of ocean wave modelling the Serre equations are the best placed [7]; retaining high-order σ terms and allowing arbitrary wave amplitude. Hence the overarching goal of our research is the development of large-scale, efficient and robust computational methods for the Serre equations for the purposes of wave modelling.

1.1 Objectives of the Thesis

In view of the overarching goal, the primary motivation of this thesis was the development of a numerical method for solving the one-dimensional Serre equations that is robust to steep gradients in the free surface, can handle dry beds and can be readily extended to the two-dimensional Serre equations using unstructured meshes.

Some of these goals were achieved through the development of the Finite Element Volume Method (FEVM). The FEVM is an improvement of the Finite Difference Volume Methods described by Zoppou [13]. The FEVM can adequately handle dry beds and uses a finite element method instead of a finite difference method, making it suitable for unstructured meshes.

The FEVM was assessed with a linear analysis, a validation against analytic

and forced solutions and experimental results. At all stages of this assessment the method is compared to at least one other method to demonstrate its strengths and weaknesses. Overall, the method is found to be superior to others and satisfies all the objectives of the thesis.

1.2 Original Contribution of the Thesis

My research made the following original contributions to the field:

- Implementation of the third-order finite difference volume method.
- Observation and justification of a new structure in the solution of the Serre equations in the presence of steep gradients in the free surface.
- Extension of the second-order finite difference volume method to allow for dry beds.
- Development and description of the well-balanced second-order finite element volume method that can handle dry beds.
- A linear analysis of convergence for all developed finite volume based methods as well as some finite difference methods.
- A complete linear analysis of the dispersion properties for all developed finite volume based methods as well as some finite difference methods.
- Validation of the method using forced solutions where all terms of the Serre equations are present for both wet and dry beds.
- Comparison of numerical solutions of the Serre equations with experimental results in the presence of dry beds and with wave breaking.

1.2.1 Publications

My research contributed to the following publications in chronological order.

A Solution of the Conservation Law Form of the Serre Equations

Australia and New Zealand Industrial and Applied Mathematics Journal (2016)
C. Zoppou, S.G. Roberts and J. Pitt

My Contribution: I validated the results of my coauthors with my own implementation of the methods. These methods were created to be consistent with a SWWE solver allowing the computational cost of solving the Serre equations and the SWWE to be compared.

Numerical Solution of the Fully Non-Linear Weakly Dispersive Serre Equations for Steep Gradient Flows

Applied Mathematical Modelling (2017)
C. Zoppou, J. Pitt and S.G. Roberts

My Contribution:

The methods, linear dispersion analysis and numerical solutions were all produced by me; these results were then written up into this paper by my coauthors.

Importance of Dispersion for Shoaling Waves

22nd International Congress on Modelling and Simulation (2017)
J. Pitt, C. Zoppou and S.G. Roberts

My Contribution:

This paper was produced by me with the support of my coauthors based on my own work.

Behaviour of the Serre Equations in the Presence of Steep Gradients Revisited

Wave Motion (2018)
J.P.A. Pitt, C. Zoppou and S.G. Roberts

My Contribution:

This paper was produced by me with the support of my coauthors based on my own work.

1.3 Organisation of the Thesis

Chapter 2 proceeds by presenting the one-dimensional Serre equations in conservation law form with a source term. It's dispersion and conservation properties and known analytic solutions are also presented. The forced Serre equations and the concept of forced solutions are introduced. Followed by a summary of the main results of my investigation into the behaviour of the Serre equations in the presence of steep gradients in the free surface [14].

This is followed by Chapter 3 which describes in detail the FEVM. In this thesis the results of other numerical methods are also provided. Descriptions of these methods can be found in the literature [14, 15].

Chapter 4 provides a linear analysis of the convergence and dispersion properties of the FEVM in detail. The analysis begins with the linearised Serre equations over a horizontal bed and then derives the evolution matrix; through which the convergence and dispersion properties of the methods can be studied. The results of the linear analysis are also provided for all the methods used by Pitt et al. [14] for comparison.

The convergence and conservation properties of the numerical methods of Pitt et al. [14] are then assessed in Chapter 5 using analytic and forced solutions of the Serre equations. While in Chapter 6 the numerical methods are validated against experimental results.

Finally, Chapter 7 summarises the major contributions and findings of the thesis and provides ideas for future work.

Chapter 2

The Serre Equations

In this chapter the Serre equations are introduced and their relevant properties are presented.

The Serre equations are a system of partial differential equations that describe the free-surface waves of fluids whose motion is dominated by gravitational forces. They are an approximation to the Euler equations [1]; describing waves in shallow water when the characteristic depth of the water h_0 is much smaller than the characteristic wavelength of the waves λ_0 so that the shallowness parameter $\sigma = h_0/\lambda_0 \ll 1$. Typically, water is considered to be shallow when $\sigma \leq 1/20$ [16]. Tsunamis and storm surges are shallow water waves as the typical ocean depth is $4km$ and both can have wavelengths up to $100km$ long, even 100's of kilometres long for tsunamis.

The Serre equations for one-dimensional flows over horizontal beds were first derived by Serre [17] using asymptotic expansion, then later using depth integration by Su and Gardner [18]. They are equivalent to the Green-Naghdi equations [19] derived using the theory of directed fluid sheets. The Serre equations were then extended to spatially varying bathymetry by Seabra-Santos et al. [20].

The Serre equations are fully non-linear and thus applicable across the entire range of wave amplitudes a_0 which are usually characterised using the non-linearity parameter $\epsilon = a_0/h_0$. The fluid described by the Serre equations possesses a non-hydrostatic pressure distribution and is dispersive in nature, as are real fluids. Furthermore, the dispersion relationship of linear waves of the Serre equations well approximates the linear wave theory for the Euler equations [21]. For these reasons the Serre equations are considered one of the best approximate water wave models up to wave-breaking [7, 22].

In this chapter we present the one-dimensional Serre equations and a reformu-

lation of these equations into conservation law form with a source term. We then present the relevant properties of the Serre equations and introduce the forced solutions which are used to assess the validity of the numerical methods. Finally, the contribution of my research to understanding the behaviour of steep gradients in the free-surface for the Serre equations is summarised.

2.1 The One-Dimensional Serre Equations

In this thesis we take the Serre equations as derived from the depth-integration approach [18, 20]. Given the extent of the literature already available for the derivation of these equations we will only introduce the relevant quantities and present the equations. The one-dimensional Serre equations describe the behaviour of unsteady free surface fluid flow for an inviscid fluid with a constant density ρ neglecting wave-breaking. In this thesis we will also neglect bottom friction effects as they can be incorporated into our methods after solving the Serre equations without them.

The primitive variables of the Serre equations are the height $h(x,t)$ of a column of fluid above the stationary bed profile given by $b(x)$ and the horizontal velocity $u(x,t)$ of the column of fluid which are all shown in Figure 2.1. The stage $w(x,t) = h(x,t)+b(x)$ gives the absolute location of the free surface. Additionally, to relate the primitive variables of the Serre equations to the intuitive variables of the Euler equations we introduce the horizontal velocity $u'(x,z,t)$ and the vertical velocity $v'(x,z,t)$ of a fluid particle.

The derivation is similar to that of the Shallow Water Wave Equations (SWWE) [23]. In particular, we assume that the horizontal velocity of a particle of fluid $u'(x,z,t)$ inside a column of fluid equals the horizontal velocity of the column of fluid $u(x,t)$. By integrating the conservation of mass equation for an invscid fluid we obtain the distribution of the vertical velocity of a fluid particle throughout a column of fluid [13]

$$v'(x,z,t) = u\frac{\partial b}{\partial x} - (z-b)\frac{\partial u}{\partial x}. \tag{2.1}$$

Unlike the SWWE the vertical velocity of fluid particle in the Serre equations is not zero throughout the depth of water. This leads to a non-hydrostatic pressure distribution on the fluid particles which is derived by integrating the conservation of vertical momentum equation given by the Euler equations [13]

$$p'(x,z,t) = \underbrace{\rho g\left(h+b-z\right)}_{\text{hydrostatic pressure}} + \rho\left(h+b-z\right)\Psi + \frac{1}{2}\rho\left(h^2-\left[z-b\right]^2\right)\Phi \tag{2.2}$$

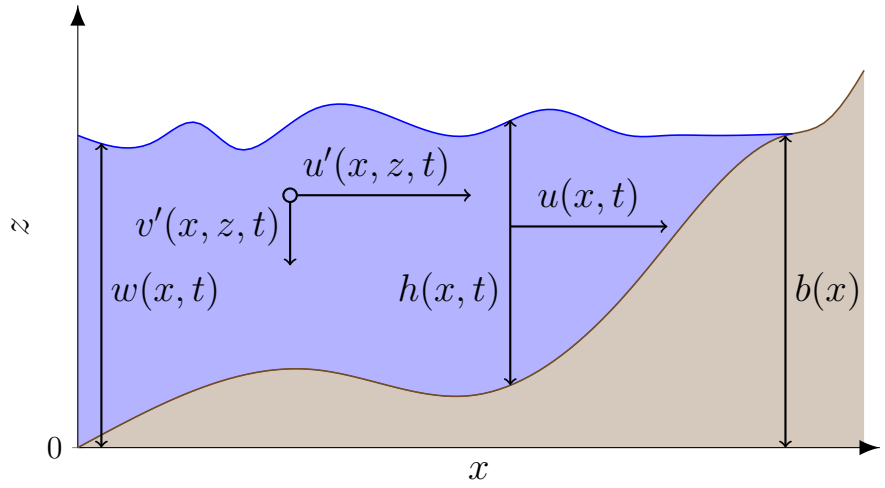

Figure 2.1: Diagram demonstrating a free surface flow (■) over a bed (■) where $w(x,t)$ is the absolute location of the free surface, $v'(x,z,t)$ is the vertical velocity of a particle of fluid, $u'(x,z,t)$ is the horizontal velocity of a particle of fluid, $h(x,t)$ is the height of a column of fluid, $u(x,t)$ is the horizontal velocity of a column of fluid and $b(x)$ is the stationary bed profile.

where

$$\Psi = \frac{\partial b}{\partial x}\left(\frac{\partial u}{\partial t} + u\frac{\partial u}{\partial x}\right) + u^2\frac{\partial^2 b}{\partial x^2}, \tag{2.3a}$$

$$\Phi = \frac{\partial u}{\partial x}\frac{\partial u}{\partial x} - u\frac{\partial^2 u}{\partial x^2} - \frac{\partial^2 u}{\partial x \partial t}. \tag{2.3b}$$

The hydrostatic pressure term $\rho g\,(h + b - z)$ is the pressure due to the weight of water above the fluid particle. The non-hydrostatic pressure terms are a consequence of the non-zero vertical velocity which modifies the underlying hydrostatic pressure distribution producing dispersive waves in the free surface.

Integrating the Euler equations [13, 18] over the entire depth with a no-slip condition at the bed, a free surface condition at the free surface, the vertical velocity relation (2.1) and the pressure distribution (2.2) we obtain the Serre equations

$$\frac{\partial h}{\partial t} + \frac{\partial (uh)}{\partial x} = 0, \tag{2.4a}$$

$$\frac{\partial (uh)}{\partial t} + \frac{\partial}{\partial x}\left(u^2 h + \frac{gh^2}{2} + \frac{h^2}{2}\Psi + \frac{h^3}{3}\Phi\right) + \frac{\partial b}{\partial x}\left(gh + h\Psi + \frac{h^2}{2}\Phi\right) = 0 \tag{2.4b}$$

which are a depth integrated approximation to the conservation of mass and horizontal momentum equations. When $\Phi = \Psi = 0$ the Serre equations reduce to the SWWE where the vertical velocity is zero over the depth, the pressure distribution is hydrostatic and there is no dispersion.

Due to the presence of the Φ and Ψ terms the Serre equations are more difficult to solve analytically and numerically than the SWWE. The primary reason for this is that whilst the SWWE are hyperbolic the Serre equations are neither hyperbolic nor parabolic. Furthermore, the Serre equations are not in conservation law form due to the presence of temporal derivatives in Φ and Ψ, although they are derived from conservation equations.

For a horizontal bed $\partial b/\partial x = 0$, $\Psi = 0$ and so the Serre equations reduce to

$$\frac{\partial h}{\partial t} + \frac{\partial (uh)}{\partial x} = 0, \tag{2.5a}$$

$$\frac{\partial (uh)}{\partial t} + \frac{\partial}{\partial x}\left(u^2 h + \frac{gh^2}{2} + \frac{h^3}{3}\Phi\right) = 0. \tag{2.5b}$$

For a horizontal bed the Serre equations are more challenging to solve analytically and numerically than the SWWE.

2.1.1 Alternative Form

A major hurdle for developing numerical methods for the Serre equations is the presence of the temporal derivative in Φ and Ψ (2.3). By rewriting the Serre equations and introducing a new conserved quantity G [13, 24, 25] the Serre equations can be written in conservation law form with a source term

$$\frac{\partial h}{\partial t} + \frac{\partial (uh)}{\partial x} = 0, \tag{2.6a}$$

$$\begin{aligned}\frac{\partial G}{\partial t} + \frac{\partial}{\partial x}\left(uG + \frac{gh^2}{2} - \frac{2}{3}h^3\left[\frac{\partial u}{\partial x}\right]^2 + h^2 u \frac{\partial u}{\partial x}\frac{\partial b}{\partial x}\right) \\ \underbrace{+ \frac{1}{2}h^2 u \frac{\partial u}{\partial x}\frac{\partial^2 b}{\partial x^2} - h u^2 \frac{\partial b}{\partial x}\frac{\partial^2 b}{\partial x^2} + gh\frac{\partial b}{\partial x}}_{\text{source term}} = 0\end{aligned} \tag{2.6b}$$

with

$$G = uh\left(1 + \frac{\partial h}{\partial x}\frac{\partial b}{\partial x} + \frac{1}{2}h\frac{\partial^2 b}{\partial x^2} + \left[\frac{\partial b}{\partial x}\right]^2\right) - \frac{\partial}{\partial x}\left(\frac{1}{3}h^3\frac{\partial u}{\partial x}\right) \tag{2.7}$$

which resembles h multiplied by the irrotationality [26, 27].

This conservation law form makes the Serre equations well suited to be numerically solved using the finite volume method for the conservation of h and G equations, provided one can solve for the remaining primitive variable u given h, G and b.

For a horizontal bed $\partial b/\partial x = 0$ the conservation law form of the Serre equations using the new quantity G is

$$\frac{\partial h}{\partial t} + \frac{\partial (uh)}{\partial x} = 0, \tag{2.8a}$$

$$\frac{\partial G}{\partial t} + \frac{\partial}{\partial x}\left(uG + \frac{gh^2}{2} - \frac{2}{3}h^3 \left[\frac{\partial u}{\partial x}\right]^2 \right) = 0 \tag{2.8b}$$

with

$$G = uh - \frac{\partial}{\partial x}\left(\frac{1}{3}h^3 \frac{\partial u}{\partial x} \right). \tag{2.8c}$$

2.2 Properties

The Serre equations possess a number of desirable properties for the modelling of water waves; in particular their conservation of fundamental quantities and dispersion relation. If a numerical method accurately approximates the Serre equations then the numerical method should reproduce the conservation and dispersion properties of the Serre equations. Furthermore, the numerical method should accurately reproduce the analytic solutions of the Serre equations. In this thesis the conservation and dispersion properties and the analytic solutions of the Serre equations are used to assess the veracity of numerical methods.

2.2.1 Conservation Properties

A quantity is conserved if the total amount of a quantity q in a closed system remains constant through time.

Definition 2.1. The total amount of a quantity q in a system occurring on the interval $[a, b]$ at time t is

$$\mathcal{C}_q(t) = \int_a^b q(x,t)\, dx.$$

Using this notation conservation of a quantity q implies that $\mathcal{C}_q(0) = \mathcal{C}_q(t)$ for all t.

Integrating the Serre equations in both non-conservation law form (2.4) and conservation law form (2.6) for a closed system we get that h, uh and G are conserved by the Serre equations. Additionally, the Green-Naghdi equations [19] which are equivalent to the Serre equations for one-dimensional flows were derived by conserving the energy

$$\mathcal{H}(x,t) = \frac{1}{2}\left(gh\left(h+2b\right) + hu^2 + \frac{h^3}{3}\left[\frac{\partial u}{\partial x}\right]^2 + u^2 h\left[\frac{\partial b}{\partial x}\right]^2 - uh^2\frac{\partial u}{\partial x}\frac{\partial b}{\partial x}\right).$$

Therefore, the one-dimensional Serre equations should also conserve $\mathcal{H}$. The energy $\mathcal{H}$ is the sum of the gravitational potential energy

$$\frac{1}{2}\int_b^{h+b} gz\, dx = \frac{1}{2}gh\left(h+2b\right),$$

the horizontal kinetic energy

$$\frac{1}{2}\int_b^{h+b} (u')^2\, dx = \frac{1}{2}hu^2$$

and the vertical kinetic energy

$$\frac{1}{2}\int_b^{h+b} (v')^2\, dx = \frac{1}{2}\left(\frac{h^3}{3}\left[\frac{\partial u}{\partial x}\right]^2 + u^2 h\left[\frac{\partial b}{\partial x}\right]^2 - uh^2\frac{\partial u}{\partial x}\frac{\partial b}{\partial x}\right)$$

for a column of fluid. Where the vertical velocity v' in the Serre equations is given by (2.1). For horizontal beds $\mathcal{H}$ is the Hamiltonian of the Serre equations [28].

For the system to be closed the flux terms of the equations for h and uh (2.4) at the boundaries must cancel and the integral of the source term over the domain must vanish.

2.2.2 Dispersion Properties

The dispersion properties are studied by linearising the Serre equations with a horizontal bed, assuming periodic wave solutions and then deriving a relationship between the frequency ω and the wave number k of these solutions. For the Serre equations the dispersion relation [25] is

$$\omega^{\pm} = Uk \pm k\sqrt{gH}\sqrt{\frac{3}{\left(kH\right)^2+3}} \tag{2.9}$$

where U and H are the mean velocity and height of the fluid respectively and the subscript $\pm$ denotes the positive and negative branches of the dispersion relation. Barthélemy [21] compared this dispersion relation to the dispersion relation given by the linear theory for water waves and demonstrated its utility when k is small. However, when k is large the difference between the dispersion relation of the Serre equations and that of the linear water wave theory increases.

From the dispersion relation (2.9) the phase velocity $v_p^{\pm} = \omega^{\pm}/k$ and the group velocity $v_g^{\pm} = \partial\omega^{\pm}/\partial k$ can be written in terms of the wave number as

$$v_p^{\pm} = U \pm \sqrt{gH}\sqrt{\frac{3}{(kH)^2 + 3}},$$

$$v_g^{\pm} = U \pm \sqrt{gH}\left(\sqrt{\frac{3}{(kH)^2 + 3}} \mp (kH)^2 \sqrt{\frac{3}{\left([kH]^2 + 3\right)^3}}\right).$$

Since both the phase and group velocities depend on the wave number, waves of different wavelengths travel at different speeds indicating that the Serre equations describe dispersive waves.

Fortunately, the phase velocity and the group velocity of waves are bounded, since as $k \to 0$ then $v_p^{\pm}$ and $v_g^{\pm} \to U \pm \sqrt{gH}$ and as $k \to \infty$ then $v_p^{\pm}$ and $v_g^{\pm} \to U$. Therefore, we have that

$$U - \sqrt{gH} \leq v_p^- \leq U \leq v_p^+ \leq U + \sqrt{gH}, \tag{2.10a}$$

$$U - \sqrt{gH} \leq v_g^- \leq U \leq v_g^+ \leq U + \sqrt{gH} \tag{2.10b}$$

so that the speed of waves in the Serre equations are bounded by the speed of waves in the SWWE.

2.2.3 Analytic Solutions

Currently few analytic solutions have been discovered for the Serre equations. There is a travelling wave solution for a horizontal bed [29] and the trivial stationary lake at rest solution for arbitrary bathymetry.

Solitary Travelling Wave Solution

The Serre equations admit a travelling wave solution that propagates at a constant speed without deformation due to a balance between the non-linear and dispersive

effects. Unlike the Euler equations this travelling wave solution has a closed form

$$h(x,t) = a_0 + a_1 \text{sech}^2\left(\kappa\left[x - ct\right]\right), \tag{2.11a}$$

$$u(x,t) = c\left(1 - \frac{a_0}{h(x,t)}\right), \tag{2.11b}$$

$$b(x) = 0 \tag{2.11c}$$

with

$$\kappa = \frac{\sqrt{3a_1}}{2a_0\sqrt{(a_0 + a_1)}},$$

$$c = \sqrt{g(a_0 + a_1)}.$$

From these equations the total amounts of h (A.1a), uh (A.1b), G (A.1c) and $\mathcal{H}$ (A.1d) at $t = 0s$ can be derived.

This solitary wave solution has an amplitude of a_1, an infinite wavelength and propagates on water a_0 deep. It is one member of a family of smooth periodic travelling wave solutions [29]. Note that these solitary wave solutions are not true solitons, due to their inelastic collisions with one another [30].

This analytic solution can only be reproduced with the appropriate order of accuracy if all terms of the Serre equations with a horizontal bed (2.8) are adequately approximated by the numerical method. Furthermore, since this solution is maintained by a balance between non-linear and dispersive effects it tests the balance of these effects in the numerical method. Therefore, this analytic solution is a good test for assessing the accuracy of numerical methods for solving the Serre equations with a horizontal bed (2.8).

Lake at Rest

The lake at rest solution is a trivial stationary solution of the Serre equations that exists for all bathymetry $b(x)$. It is a consequence of a balance between the hydrostatic pressure distribution and the forcing of the bed slope. The lake at rest solution is

$$h(x,t) = \max\left\{a_0 - b(x), 0\right\}, \tag{2.12a}$$

$$u(x,t) = 0, \tag{2.12b}$$

$$G(x,t) = 0. \tag{2.12c}$$

It represents a quiescent body of water with a horizontal water surface or stage $w(x,t) = h(x,t) + b(x)$ over any bathymetry. With the maximum function included in the water depth to allow for dry regions of the bed when $b(x) > a_0$. We write these quantities in terms of $b(x)$ as this solution holds for all bed profiles. The corresponding total amounts of h and $\mathcal{H}$ can be calculated by summing their total amounts in wet (A.2) regions. While the total amounts of u and G are zero.

Since $w(x,t)$ is constant when $h > 0$ then $\partial w/\partial x = \partial h/\partial x + \partial b/\partial x = 0$ and $u = 0$ so that the Serre equations (2.6) reduce to

$$\frac{\partial h}{\partial t} = 0, \qquad \frac{\partial G}{\partial t} = 0.$$

Therefore, G and h are constant in time and so is u and thus the solution is stationary.

For naive numerical methods of the Serre equations the hydrostatic pressure terms do not balance the bed slope terms. This causes the numerical solutions of an initially still lake to produce non-physical velocities, degrading their convergence to the solution. To combat this, modifications are made to the flux and source term approximations so that these terms do balance, leading to a so called 'well-balanced' method. This analytic solution then provides a test for the effectiveness of these well-balancing modifications to the numerical methods.

2.3 Forced Solutions

The known analytic solutions of the Serre equations provide a stringent test when the bed is horizontal, as all terms in the equations are non-zero and vary in space and time. For varying bathymetry there is only the lake at rest solution where all terms are constant in time and some vanish. Therefore, the accuracy of the approximations of all terms of the Serre equations in the numerical method is not adequately assessed using only the currently available analytic solutions.

Currently the verification of the order of accuracy of the numerical methods for transient solutions with varying bathymetry requires the use of forced solutions. To do this we select some particular functions for all of the primitive quantities; h, u and b which we denote h^*, u^* and b^* respectively. To force these functions h^*, u^* and b^* to be solutions of the Serre equations (2.6) we add the terms S_h

and S_G to obtain the forced Serre equations

$$\frac{\partial h}{\partial t} + \frac{\partial (uh)}{\partial x} + S_h = 0, \tag{2.13a}$$

$$\begin{aligned}\frac{\partial G}{\partial t} + \frac{\partial}{\partial x}\left(uG + \frac{gh^2}{2} - \frac{2}{3}h^3\left[\frac{\partial u}{\partial x}\right]^2 + h^2 u \frac{\partial u}{\partial x}\frac{\partial b}{\partial x}\right) \\ + \frac{1}{2}h^2 u \frac{\partial u}{\partial x}\frac{\partial^2 b}{\partial x^2} - hu^2 \frac{\partial b}{\partial x}\frac{\partial^2 b}{\partial x^2} + gh\frac{\partial b}{\partial x} + S_G = 0\end{aligned} \tag{2.13b}$$

where

$$S_h = -\frac{\partial h^*}{\partial t} - \frac{\partial (u^* h^*)}{\partial x},$$

$$S_G = -\frac{\partial G^*}{\partial t} - \frac{\partial}{\partial x}\left(u^* G^* + \frac{g\left[h^*\right]^2}{2} - \frac{2}{3}\left[h^*\right]^3\left[\frac{\partial u^*}{\partial x}\right]^2 + \left[h^*\right]^2 u^* \frac{\partial u^*}{\partial x}\frac{\partial b^*}{\partial x}\right)$$

$$-\frac{1}{2}\left[h^*\right]^2 u^* \frac{\partial u^*}{\partial x}\frac{\partial^2 b^*}{\partial x^2} + h^*[u^*]^2 \frac{\partial b^*}{\partial x}\frac{\partial^2 b^*}{\partial x^2} - gh^*\frac{\partial b^*}{\partial x}.$$

These forced Serre equations are then numerically solved by solving the Serre equations (2.6) with the analytic values of S_h and S_G given h^*, u^* and b^*. So that, the only error present in the numerical solutions of the forced Serre equations is the error produced by the numerical methods used to solve the Serre equations.

Note that since the choice of the forced solutions h^*, u^* and b^* is arbitrary the solutions of the forced Serre equations need not be conservative or retain any of the properties of the underlying Serre equations.

2.4 Behaviour in the Presence of Steep Gradients

To ensure that the developed numerical methods are robust, their capability to handle initial condition problems with quantities possessing discontinuities must be tested. One group of these initial condition problems that has been of particular interest to the water wave community is the dam-break problem [24, 29, 31, 32, 33]; where a body of water is initially still with a discontinuous

jump in its surface between two depth values. So that

$$h(x,0) = \begin{cases} h_l & x < x_0 \\ h_r & x \geq x_0, \end{cases} \tag{2.14a}$$

$$u(x,0) = 0, \tag{2.14b}$$

$$G(x,0) = 0, \tag{2.14c}$$

$$b(x) = 0 \tag{2.14d}$$

where h_l and h_r are the height to the left and right of x_0, respectively.

Currently, these dam-break problems (2.14) have no known analytic solutions for the Serre equations. However, some insight into the behaviour of the evolution of these initial condition problems has been gained from asymptotic [29] and linear [34] analyses.

There have also been a number of numerical solutions to dam-break problems presented in the literature [24, 29, 31, 32, 33] which have used a variety of numerical methods. Some of these numerical methods could not handle discontinuous initial conditions [29, 31, 32, 33] and so smooth approximations to the initial conditions (2.14) were employed. The variety of numerical approaches has lead to different conclusions about the behaviour of the evolution of dam-break problems in the Serre equations in the literature. To resolve these differences a comprehensive review of a particular dam-break problem with a variety of numerical methods and smoothing of the initial conditions was performed [14].

The relevant results garnered from the asymptotic [29] and linear [34] analyses for the evolution of the dam-break problem are presented here, followed by a summary of the numerical results [14], which constituted a significant portion of my research.

Asymptotic and Linear Results

The asymptotic analysis of El et al. [29] used Whitham modulation to study the evolution of dispersive shock waves of the Serre equations as $t \to \infty$. Because, a dispersive shock wave is generated in the evolution of the dam-break problem in the Serre equations; these results are very useful. In particular, they provide a relationship between the initial heights of the dam-break problem h_l and h_r and the amplitude A^+ and speed S^+ of the leading wave in the resulting dispersive

wave train which are obtained by solving

$$\frac{\Delta}{(A^+ + 1)^{1/4}} - \left(\frac{3}{4 - \sqrt{A^+ + 1}}\right)^{21/10} \left(\frac{2}{1 + \sqrt{A^+ + 1}}\right)^{2/5} = 0, \tag{2.15a}$$

$$S^+ = \sqrt{g\,(A^+ + 1)} \tag{2.15b}$$

where

$$\Delta = \frac{1}{4h_r}\left(\sqrt{\frac{h_l}{h_r}} + 1\right)^2.$$

These estimates were found to agree well with numerical simulations provided that $\Delta < 1.43$ [29].

For the linearised Serre equations we obtain the dispersion relation (2.9) from which the phase and group velocities can be determined (2.10). The negative and positive branches of the phase and group velocities are separated, implying that there should be a separation of the upwind and downwind parts of the dispersive wave-train [34]. Therefore, the structure of dispersive shock waves of the Serre equations should be two separate dispersive wave trains.

Numerical Solutions for the Smoothed Dam-break Problem

To resolve the differences present in the literature a variety of numerical methods were used to solve the most common class of smoothed versions of the dam-break problem initial conditions (2.14) which are given by

$$\begin{aligned} h(x,0) &= h_r + \frac{h_l - h_r}{2}\left(1 + \tanh\left(\frac{x_0 - x}{\alpha}\right)\right), \\ u(x,0) &= 0, \\ G(x,0) &= 0, \\ b(x) &= 0 \end{aligned}$$

where α controls the width of the transition from h_l to h_r and thus the steepness of the initial gradient in the water surface. This was termed the smoothed dam-break problem and most of the numerical simulations were focused on solutions for $h_l = 1.8m$, $h_r = 1m$ and $x_0 = 500m$ with a final time of $t = 30s$. The smoothing parameter α and the resolution of the methods were varied to investigate their influence on the observed behaviour of the numerical solution. Four structures were observed in the numerical solutions; the non-oscillatory structure, the flat

structure, the node structure and the growth structure. Numerical solutions at $t = 30s$ for the mentioned h_l, h_r and x_0 values demonstrating examples of the observed structures are shown in Figure 2.2.

The growth structure was consistently observed in numerical solutions of the smoothed dam-break problem as $\alpha \to \infty$ for high-order accurate methods on high resolution grids. Therefore, the growth structure represents the true structure of the solution of the Serre equations for the dam-break problem with the corresponding h_l and h_r values at $t = 30s$. The observation of other behaviours at $t = 30s$ is caused by; small α values which overly smooth the initial conditions, low-order numerical methods introducing large diffusive errors and low numerical resolutions which cannot resolve the high frequency waves observed in the growth structure. These structures exist on a spectrum where the severity of these effects determine the observed behaviour. So that, the most severe damping effects produced the non-oscillatory structure and the least severe effects produced the growth structure. These effects explained the observations of different structures previously present in the literature [24, 29, 31, 32].

The differences in the observed structures are primarily driven by the different internal structures of the dispersive shock wave, so that for the flat, node and growth structure in Figure 2.2 the front of the dispersive wave trains are indistinguishable. Therefore, the results of numerical solutions that have not resolved all the internal structure present in the growth structure still agree well with the Whitham modulation results (2.15) of El et al. [29].

The amplitude of waves at the centre of the growth structure decays over time, resulting in the observation of the flat structure when t is large. These results agree with the linear argument put forth by Dougalis et al. [34]. This indicates that for smaller times the non-linear terms of the Serre equations play a significant role in the evolution of steep gradients, while for long times the linear terms are dominant and thus a separation of the dispersive wave trains is observed.

In this chapter the Serre equations and their relevant properties were given. The forced Serre equations were introduced and a summary of the main results for the evolution of steep gradients in the free surface was provided.

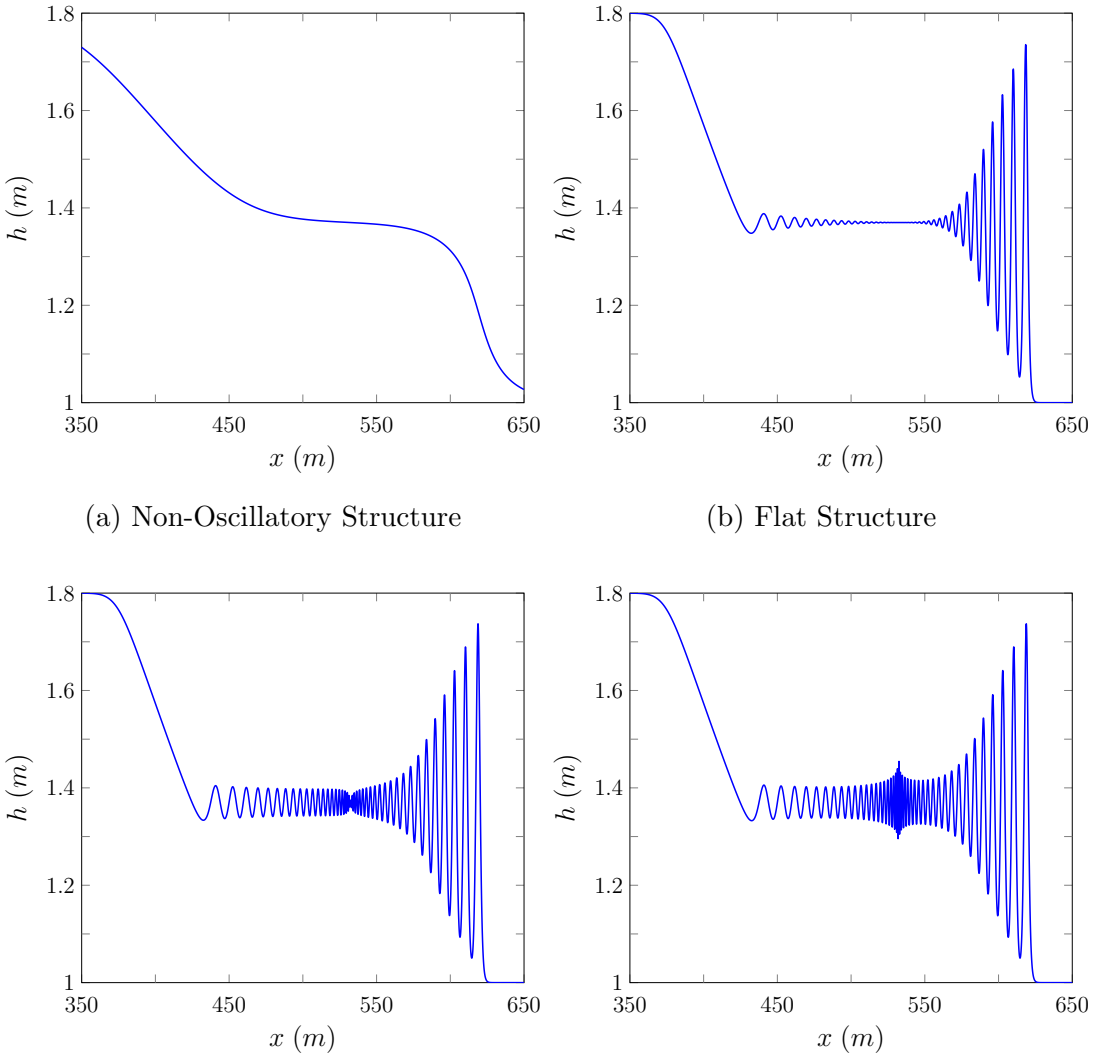

(a) Non-Oscillatory Structure

(b) Flat Structure

(c) Node Structure

(d) Growth Structure

Figure 2.2: Examples of the different structures observed in numerical solutions to the smoothed dam-break problem displayed by Pitt et al. [14].

Chapter 3

Finite Element Volume Method

In this chapter we introduce the notation for the numerical grids and then describe the second-order Finite Element Volume Method (FEVM) in detail.

A variety of numerical methods have been used to solve the Serre equations; from complete finite difference methods [29, 35] and finite element methods [25, 31, 32] to combinations of finite difference and finite volume methods [15, 24]. Splitting techniques have also been employed, most commonly to split the Serre equations into their non-linear and dispersive parts; resulting in an elliptic operator for the dispersive part and the SWWE for the non-linear part [30, 36, 37].

Numerical methods that make use of the conservation law form of the Serre equations (2.6) [15, 24, 25] are the most promising for the two dimensional Serre equations with variable bathymetry. The primary reason for this is that these methods are robust and extend well to unstructured meshes with complex geometries which are the meshes most commonly used for modelling physical scenarios. Secondly, to properly handle the elliptic operator produced by the non-linear and dispersive splitting requires overly restrictive assumptions about the smoothness of the physical quantities, particularly the water depth.

I have developed an extension of the Finite Difference Volume Methods (FDVM) [15, 24] that uses a finite element method in place of the finite difference method. This second-order FEVM which will be referred to as FEVM_2 was a main objective of the thesis; it consists of two main parts a Finite Element Method (FEM) to solve (2.7) and a Finite Volume Method (FVM) to solve (2.6) hence its name. Making use of these two methods results in a numerical method with a number of desirable properties. It is robust in the presence of steep gradients in the free surface [14], robust during the wetting and drying of beds and all the terms of the finite volume method can be calculated knowing only the quantities inside the

cell. This last point indicates that this method is the ideal variant of the finite volume based methods [15] to be extended to solve the two-dimensional Serre equations on unstructured meshes with parallelised code.

In addition to the FEVM_2, the first- and second-order FDVM of Le Métayer et al. [24] and Zoppou et al. [15] were reproduced. These methods will be referred to as FDVM_1 and FDVM_2 respectively. Furthermore the third-order extension FDVM_3 was implemented during my research. I have also reproduced the second-order naive finite difference method [38] and the finite difference method of El et al. [29]; which I refer to as $\mathcal{D}$ and $\mathcal{W}$ respectively. Descriptions of these methods have already been published [14, 15] and therefore, are omitted from the thesis.

3.1 Notation for Numerical Grids

In the FEVM_2, time and space will be discretised in different ways. Time is broken up into time levels separated by a constant duration Δt and space is broken up into cells of constant width Δx. The FEVM can be extended to allow for varying Δt and Δx values, with this description restricted to the constant case for simplicity. The notation for time is quite simple; from an initial time t^0 we define the n^{th} time level where $n \in \mathbb{N}$ to be

$$t^n = t^0 + n\Delta t.$$

The goal of FEVM_2 is to update the quantities at the current time level t^n to the next time level t^{n+1} by solving the equations.

The notation for space is a bit more complicated; as we require definitions of multiple locations inside the cells. The cells are defined by their midpoints; which are given from a starting location x_0, so that the midpoint of the j^{th} cell where $j \in \mathbb{N}$ is

$$x_j = x_0 + j\Delta x.$$

Other points inside the j^{th} cell can be defined in relation to the midpoint so that

$$x_{j+s} = x_j + s\Delta x$$

where $s \in \left[-\frac{1}{2}, \frac{1}{2}\right] \subset \mathbb{R}$, although for our purposes we restrict ourselves to rational values of s. Using this notation the j^{th} cell spans $\left[x_{j-1/2}, x_{j+1/2}\right]$. These discretisations in space and time result in the grids displayed in Figure 3.1.

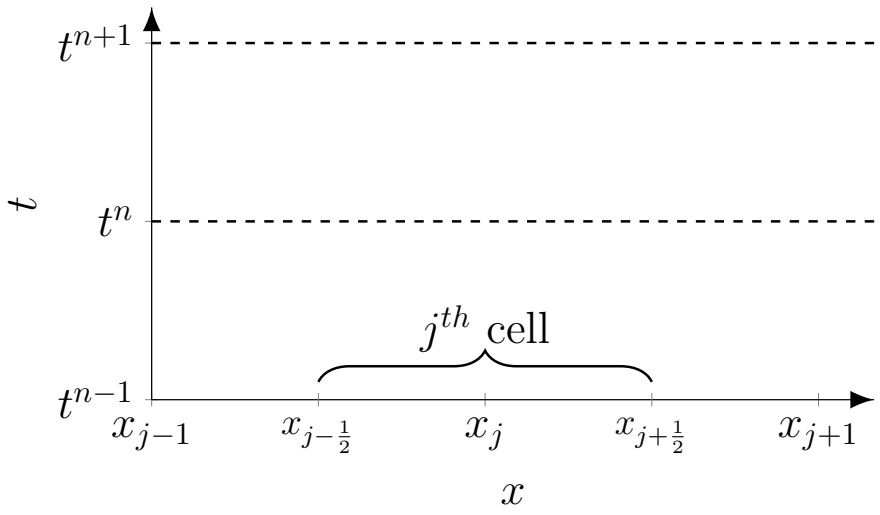

Figure 3.1: Diagram of the time levels t^{n-1}, t^n and t^{n+1} at which the numerical solution of the Serre equations will be calculated. The j^{th} cell with midpoint x_j spanning $x_{j-1/2}$ to $x_{j+1/2}$ which is a volume of the FVM and an element of the FEM is also shown.

The temporal and spatial grid notation naturally extends to our quantities of interest, for example, for a general quantity q

$$q_j^n = q(x_j, t^n).$$

These are the nodal values of q. Since the FEVM uses a FVM the cell averages of the quantities are also required. For each cell we define the average of a quantity at time level t^n as

$$\overline{q}_j^n = \frac{1}{\Delta x} \int_{x_{j-1/2}}^{x_{j+1/2}} q(x, t^n)\, dx$$

over the j^{th} cell.

In the FEVM we reconstruct quantities at various points inside the cell from the cell average values. At the cell edges $x_{j\pm1/2}$, two reconstructions are possible from each of the neighbouring cells, we distinguish between the two possible reconstructions using superscripts. For example, for the cell edge $x_{j+1/2}$ and a general quantity q, there is the reconstructed value $q^-_{j+1/2}$ from the upwind j^{th} cell and the reconstructed value $q^+_{j+1/2}$ from the downwind $(j+1)^{th}$ cell.

3.2 Structure Overview

To describe the FEVM we first present an overview of the evolution step and then provide the details for each component. We begin our evolution step with

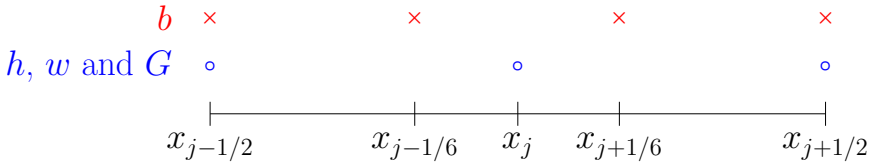

Figure 3.2: The locations of the reconstructions for h, w, G (○) and b (×) inside the j^{th} cell.

all the cell averages for h, w and G at time t^n and all the nodal values of b being known. We write these as vectors from the starting 0^{th} to the final m^{th} cell in the following way

$$\overline{\boldsymbol{q}}^n = \begin{bmatrix} \overline{q}_0^n \\ \overline{q}_1^n \\ \vdots \\ \overline{q}_m^n \end{bmatrix}, \qquad \boldsymbol{b} = \begin{bmatrix} b_0 \\ b_1 \\ \vdots \\ b_m \end{bmatrix}$$

where q is a generic quantity representing the vectors for h, G and w. The evolution step proceeds by (i) reconstructing the quantities over the cell, (ii) calculating the fluid velocity, (iii) approximating the flux, (iv) approximating the source term, (v) updating the cell averages and then (vi) applying second-order time stepping.

(i) Reconstruction: The locations for the reconstruction of all the quantities in the j^{th} cell are displayed in Figure 3.2. The quantities h, w and G are reconstructed at $x_{j-1/2}$, x_j and $x_{j+1/2}$ from their cell average values using the second-order reconstruction operators $\mathcal{R}^+_{j-1/2}$, $\mathcal{R}_j$ and $\mathcal{R}^-_{j+1/2}$ respectively. While the bed profile b in the j^{th} cell is reconstructed at $x_{j-1/2}$, $x_{j-1/6}$, $x_{j+1/6}$ and $x_{j+1/2}$ from its nodal values using the fourth-order reconstruction operators $\mathcal{B}_{j-1/2}$, $\mathcal{B}_{j-1/6}$, $\mathcal{B}_{j+1/6}$ and $\mathcal{B}_{j+1/2}$ respectively.

So that for a generic quantity q representing h, w and G and the bed b we have

$$q^{\pm}_{j\pm1/2} = \mathcal{R}^{\pm}_{j\pm1/2}\left(\overline{\boldsymbol{q}}^n\right), \qquad b_{j\pm1/2} = \mathcal{B}_{j\pm1/2}\left(\boldsymbol{b}\right),$$
$$q_j = \mathcal{R}_j\left(\overline{\boldsymbol{q}}^n\right), \qquad b_{j\pm1/6} = \mathcal{B}_{j\pm1/6}\left(\boldsymbol{b}\right).$$

To keep the notation simple the time superscript is omitted from the reconstructed quantities. This generates the vectors of these quantities reconstructed for every cell; $\hat{\boldsymbol{h}}$, $\hat{\boldsymbol{w}}$, $\hat{\boldsymbol{G}}$ and $\hat{\boldsymbol{b}}$ at time t^n which are

$$\hat{\boldsymbol{q}} = \begin{bmatrix} q^+_{-1/2} \\ q_0 \\ q^-_{1/2} \\ \vdots \\ q^-_{m+1/2} \end{bmatrix}, \qquad \hat{\boldsymbol{b}} = \begin{bmatrix} b_{-1/2} \\ b_{-1/6} \\ b_{1/6} \\ b_{1/2} \\ \vdots \\ b_{m+1/2} \end{bmatrix}$$

where q is a generic quantity demonstrating these vectors for h, w and G.

(ii) Fluid Velocity: The remaining unknown quantity, the horizontal velocity of the fluid column, u is calculated at $x_{j-1/2}$, x_j and $x_{j+1/2}$ in each cell by solving (2.7) with a second-order FEM. We denote the solution map of the FEM by $\mathcal{G}$, which takes $\hat{\boldsymbol{h}}$, $\hat{\boldsymbol{G}}$ and $\hat{\boldsymbol{b}}$ as inputs. So that

$$\hat{\boldsymbol{u}} = \begin{bmatrix} u_{-1/2} \\ u_0 \\ u_{1/2} \\ \vdots \\ u_{m+1/2} \end{bmatrix} = \mathcal{G}\left(\hat{\boldsymbol{h}}, \hat{\boldsymbol{G}}, \hat{\boldsymbol{b}}\right).$$

(iii) Flux Across Cell Interfaces: We calculate the temporally averaged fluxes $F^n_{j-1/2}$ and $F^n_{j+1/2}$ across the cell boundaries $x_{j-1/2}$ and $x_{j+1/2}$ using $\mathcal{F}_{j-1/2}$ and $\mathcal{F}_{j+1/2}$, so that

$$F^n_{j\pm1/2} = \mathcal{F}_{j\pm1/2}\left(\hat{\boldsymbol{h}}, \hat{\boldsymbol{G}}, \hat{\boldsymbol{b}}, \hat{\boldsymbol{u}}\right).$$

(iv) Source Terms: We calculate the source term contribution to the cell average of a quantity over a time step; S^n_j with the operator $\mathcal{S}$

$$S^n_j = \mathcal{S}_j\left(\hat{\boldsymbol{h}}, \hat{\boldsymbol{w}}, \hat{\boldsymbol{b}}, \hat{\boldsymbol{u}}\right).$$

(v) Update Cell Averages: We update the cell average values from time t^n to t^{n+1} with a forward Euler approximation, resulting in a method that is second-order accurate in space and first-order in time.

(vi) Second-Order SSP Runge-Kutta Method: We repeat steps (i)-(v) and use SSP Runge-Kutta time stepping to obtain $\overline{\boldsymbol{h}}$ and $\overline{\boldsymbol{G}}$ at t^{n+1} with second-order accuracy in space and time.

3.2.1 Reconstruction

We now provide details for the reconstruction of h, w, G and b in the j^{th} cell at the locations shown in Figure 3.2. For the purposes of the reconstruction we will assume that the mesh is structured. The reconstruction methods described here can be extended to unstructured meshes through generalisations of the interpolation techniques employed here [39, 40]. For h, w and G the reconstructions are performed from the cell averages. While b is reconstructed from the nodal values.

Reconstruction of the h, w and G

We reconstruct h, w and G with piecewise linear functions over a cell from neighbouring cell averages. Since h, w and G use the same reconstruction operators we demonstrate them for a general quantity q. For the j^{th} cell we reconstruct the values of q at $x_{j-1/2}$, x_j and $x_{j+1/2}$ in the following way

$$q^+_{j-1/2} = \mathcal{R}^+_{j-1/2}\left(\overline{\boldsymbol{q}}\right) = \overline{q}_j - \frac{\Delta x}{2} d_j, \tag{3.1a}$$

$$q_j = \mathcal{R}_j\left(\overline{\boldsymbol{q}}\right) = \overline{q}_j, \tag{3.1b}$$

$$q^-_{j+1/2} = \mathcal{R}^-_{j+1/2}\left(\overline{\boldsymbol{q}}\right) = \overline{q}_j + \frac{\Delta x}{2} d_j \tag{3.1c}$$

where

$$d_j = \text{minmod}\left(\theta \frac{\overline{q}_j - \overline{q}_{j-1}}{\Delta x}, \frac{\overline{q}_{j+1} - \overline{q}_{j-1}}{2\Delta x}, \theta \frac{\overline{q}_{j+1} - \overline{q}_j}{\Delta x}\right) \tag{3.2}$$

with $\theta \in [1, 2]$. The choice of the θ parameter changes the diffusion introduced by the reconstruction. When $\theta = 1$ the reconstruction introduces the most diffusion and is equivalent to the minmod reconstruction [41]. When $\theta = 2$ the reconstruction introduces the least diffusion and is equivalent to the monotized central reconstruction [42].

Definition 3.1. The minmod function

$$\text{minmod}\left(a_0, a_1, \dots\right) := \begin{cases} \min\left\{a_i\right\} & a_i > 0 \text{ for all } i \\ \max\left\{a_i\right\} & a_i < 0 \text{ for all } i \\ 0 & \text{otherwise} \end{cases}$$

takes a list of $a_i \in \mathbb{R}$. If all elements have the same sign then minmod returns the element with smallest absolute value, otherwise it returns zero.

The non-linear limiting used to calculate d_j ensures that the reconstruction of h, w and G inside the cell is Total Variation Diminishing (TVD) [43], hence it does

not introduce non-physical oscillations. The TVD property of this reconstruction is achieved by constraining the slope d_j to zero near local extrema, resulting in a piecewise constant reconstruction which is TVD. Away from local extrema d_j will be the gradient with the smallest absolute value, making our reconstruction second-order accurate.

The reconstruction operator $\mathcal{R}_j$ is second-order accurate regardless of the presence of local extrema. This can be seen through the error analysis of the midpoint quadrature rule [44] for which we have that

$$\overline{q}_j = \frac{1}{\Delta x} \int_{x_{j-1/2}}^{x_{j+1/2}} q \, dx = q_j + \mathcal{O}\left(\Delta x^2\right). \tag{3.3}$$

Reconstruction of the Bed Profile

For the bed profile we require a reconstruction that is at least second-order accurate for b, $\partial b/\partial x$ and $\partial^2 b/\partial x^2$. To accomplish this b is reconstructed with a cubic polynomial $C_j(x)$ centred around x_j

$$C_j(x) = c_0 \left(x - x_j\right)^3 + c_1 \left(x - x_j\right)^2 + c_2 \left(x - x_j\right) + c_3.$$

By forcing $C_j(x)$ to pass through the nodal values b_{j-2}, b_{j-1}, b_{j+1} and b_{j+2} we get

$$\begin{bmatrix} -8\Delta x^3 & 4\Delta x^2 & -2\Delta x & 1 \\ -\Delta x^3 & \Delta x^2 & -\Delta x & 1 \\ \Delta x^3 & \Delta x^2 & \Delta x & 1 \\ 8\Delta x^3 & 4\Delta x^2 & 2\Delta x & 1 \end{bmatrix} \begin{bmatrix} c_0 \\ c_1 \\ c_2 \\ c_3 \end{bmatrix} = \begin{bmatrix} b_{j-2} \\ b_{j-1} \\ b_{j+1} \\ b_{j+2} \end{bmatrix}.$$

Solving this we get the polynomial coefficients for $C_j(x)$

$$c_0 = \frac{-b_{j-2} + 2b_{j-1} - 2b_{j+1} + b_{j+2}}{12\Delta x^3},$$

$$c_1 = \frac{b_{j-2} - b_{j-1} - b_{j+1} + b_{j+2}}{6\Delta x^2},$$

$$c_2 = \frac{b_{j-2} - 8b_{j-1} + 8b_{j+1} - b_{j+2}}{12\Delta x},$$

$$c_3 = \frac{-b_{j-2} + 4b_{j-1} + 4b_{j+1} - b_{j+2}}{6}.$$

We require a continuous bed profile and so we average the two reconstructions at the cell edge from the adjacent cells. Therefore, our reconstruction of the bed profile in the j^{th} cell is the cubic which takes these values

$$\begin{aligned}
b_{j-1/2} &= \mathcal{B}_{j-1/2}(\boldsymbol{b}) = \frac{1}{2}\left(C_j(x_{j-1/2}) + C_{j-1}(x_{j-1/2})\right), \\
b_{j-1/6} &= \mathcal{B}_{j-1/6}(\boldsymbol{b}) = C_j(x_{j-1/6}), \\
b_{j+1/6} &= \mathcal{B}_{j+1/6}(\boldsymbol{b}) = C_j(x_{j+1/6}), \\
b_{j+1/2} &= \mathcal{B}_{j+1/2}(\boldsymbol{b}) = \frac{1}{2}\left(C_j(x_{j+1/2}) + C_{j+1}(x_{j+1/2})\right).
\end{aligned}$$

3.2.2 Fluid Velocity

In the FEVM we solve for the primitive variable u given h, G and b using a finite element approximation to (2.7). For the FEM we begin with the weak form of (2.7) with a test function v over the spatial domain Ω which is

$$\int_\Omega Gv\,dx = \int_\Omega uh\left(1 + \frac{\partial h}{\partial x}\frac{\partial b}{\partial x} + \frac{1}{2}h\frac{\partial^2 b}{\partial x^2} + \left[\frac{\partial b}{\partial x}\right]^2\right)v - \frac{\partial}{\partial x}\left(\frac{1}{3}h^3\frac{\partial u}{\partial x}\right)v\,dx.$$

Integrating by parts with zero Dirichlet boundary conditions we get

$$\begin{aligned}
\int_\Omega Gv\,dx = \int_\Omega uh\left(1 + \left[\frac{\partial b}{\partial x}\right]^2\right)v\,dx + \int_\Omega \frac{1}{3}h^3\frac{\partial u}{\partial x}\frac{\partial v}{\partial x}\,dx \\
- \int_\Omega \frac{1}{2}uh^2\frac{\partial b}{\partial x}\frac{\partial v}{\partial x}\,dx - \int_\Omega \frac{1}{2}h^2\frac{\partial b}{\partial x}\frac{\partial u}{\partial x}v\,dx. \quad (3.4)
\end{aligned}$$

By assuming that time is fixed so that all the functions only vary in space, this formulation implies that by ensuring that G, h, b and $\partial b/\partial x$ have finite integrals over Ω, then u and $\partial u/\partial x$ must have finite integrals as well. Since we require $\partial u/\partial x$ to be well defined to approximate the fluxes and the source term (2.6) and thus have finite integrals we will assume that for each time t that $h, G \in \mathbb{L}^2(\Omega)$ and $b \in \mathbb{W}^{1,2}(\Omega)$ so that $u \in \mathbb{W}^{1,2}(\Omega)$. See Appendix B for a precise definition of $\mathbb{L}^2(\Omega)$ and $\mathbb{W}^{1,2}(\Omega)$.

We simplify (3.4) by performing the integration over the cells and then summing the integrals together to get the equation for the entire domain

$$\begin{aligned}
\sum_j \left(\int_{x_{j-1/2}}^{x_{j+1/2}} \left[\left(uh\left(1 + \left[\frac{\partial b}{\partial x}\right]^2\right) - \frac{1}{2}h^2\frac{\partial b}{\partial x}\frac{\partial u}{\partial x} - G\right)v \right.\right. \\
\left.\left. + \left(\frac{1}{3}h^3\frac{\partial u}{\partial x} - \frac{1}{2}uh^2\frac{\partial b}{\partial x}\right)\frac{\partial v}{\partial x}\right]dx\right) = 0 \quad (3.5)
\end{aligned}$$

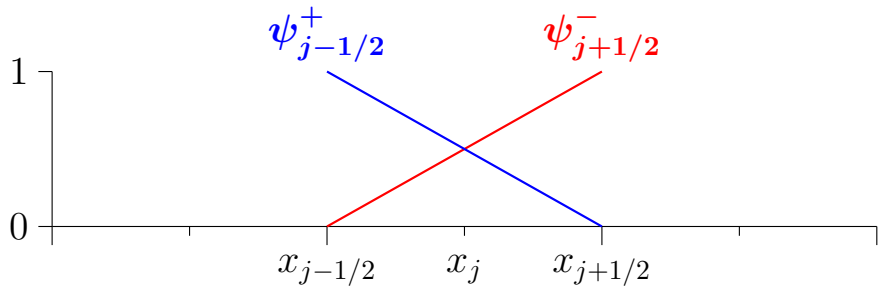

Figure 3.3: Support of the discontinuous linear basis functions ψ over a cell.

which holds for all test functions v. The next step is to replace the functions for the quantities h, G, b and u with their corresponding basis function approximations.

Basis Function Approximations

For h and G we use the basis functions ψ (B.1) which are linear inside a cell and zero elsewhere and so are not continuous as shown in Figure 3.3. This is consistent with our reconstruction which is second-order accurate inside the cell and possesses discontinuities at the cell edges. Since these basis functions are in $\mathbb{L}^2(\Omega)$ our basis function approximations to h and G are in the appropriate function space.

From the basis functions ψ we have the following representation for h and G in our FEM written for the generic quantity q

$$q = \sum_j \left(q^+_{j-1/2}\psi^+_{j-1/2} + q^-_{j+1/2}\psi^-_{j+1/2}, \right). \tag{3.6}$$

To calculate the flux and source terms in (2.6b) we require a locally calculated second-order accurate approximation to the first derivative of u. To do this we require a quadratic representation of u in each cell and since we desire $u \in \mathbb{W}^{1,2}(\Omega)$, this representation will be continuous across the cell edges $x_{j\pm1/2}$. Therefore, we use the continuous quadratic basis functions $\phi_{j\pm1/2}$ and ϕ_j (B.2) depicted in Figure 3.4.

From the basis functions ϕ our basis function approximation to u is

$$u = u_{-1/2}\phi_{-1/2} + \sum_j \left(u_j\phi_j + u_{j+1/2}\phi_{j+1/2} \right). \tag{3.7}$$

For the source term of the evolution of G equation (2.6b) we require a local approximation to the second derivative of the bed that is also second-order accurate. To allow for an appropriate second derivative of the bed profile, b must be

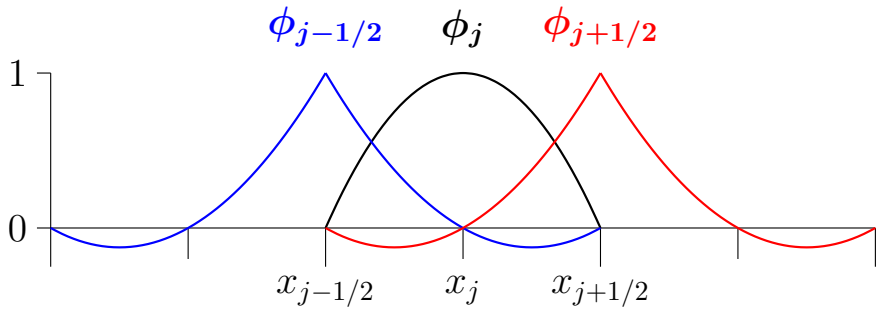

Figure 3.4: Support of the continuous piecewise quadratic basis functions ϕ over a cell.

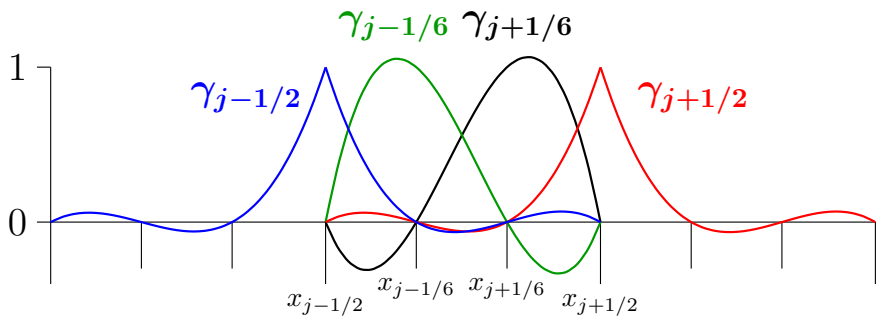

Figure 3.5: Support of the continuous piecewise cubic basis functions γ over a cell.

a member of $\mathbb{W}^{2,2}(\Omega)$ which is smoother than required by (3.4). We choose the cubic basis functions γ (B.3) which are continuous across the cell edges, as the bed profile will be continuous. These basis functions are shown in Figure 3.5 and from them we get our basis function approximation to b

$$b = b_{-1/2}\gamma_{-1/2} + \sum_j \left(b_{j-1/6}\gamma_{j-1/6} + b_{j+1/6}\gamma_{j+1/6} + b_{j+1/2}\gamma_{j+1/2} \right). \tag{3.8}$$

Calculation of Element-wise Matrices

The integral equation (3.5) holds for all v. However, since our solution space has the basis functions ϕ it is sufficient to satisfy (3.5) for all ϕ to generate the solution. Since only the basis functions $\phi_{j-1/2}$, ϕ_j and $\phi_{j+1/2}$ are non-zero over

the j^{th} cell we can calculate the j^{th} term in the sum (3.5) like so

$$\int_{x_{j-1/2}}^{x_{j+1/2}} \left(\left[uh \left(1 + \left[\frac{\partial b}{\partial x} \right]^2 \right) - \frac{1}{2} h^2 \frac{\partial b}{\partial x} \frac{\partial u}{\partial x} - G \right] \begin{bmatrix} \phi_{j-1/2} \\ \phi_j \\ \phi_{j+1/2} \end{bmatrix} + \left[\frac{1}{3} h^3 \frac{\partial u}{\partial x} - \frac{1}{2} h^2 \frac{\partial b}{\partial x} u \right] \frac{\partial}{\partial x} \left(\begin{bmatrix} \phi_{j-1/2} \\ \phi_j \\ \phi_{j+1/2} \end{bmatrix} \right) \right) dx \quad (3.9)$$

where we use our finite element approximations for h (3.6), G (3.6), u (3.7) and b (3.8). This integral can be generalised by moving to the natural reference ξ-space, as the basis functions which are non-zero in one element are just translations of the non-zero basis functions in another element. The mapping from the x-space to the ξ-space is

$$x = x_j + \xi \frac{\Delta x}{2}.$$

Therefore, the j^{th} cell $\left[x_{j-1/2}, x_{j+1/2}\right]$ gets mapped to $[-1, 1]$ in the ξ-space. Making the change of variables from x to ξ in (3.9) we get

$$\frac{\Delta x}{2} \int_{-1}^{1} \left(\left[uh \left(1 + \frac{4}{\Delta x^2} \left[\frac{\partial b}{\partial \xi} \right]^2 \right) - \frac{2}{\Delta x^2} h^2 \frac{\partial b}{\partial \xi} \frac{\partial u}{\partial \xi} - G \right] \begin{bmatrix} \phi_{j-1/2} \\ \phi_j \\ \phi_{j+1/2} \end{bmatrix} + \frac{4}{\Delta x^2} \left[\frac{1}{3} h^3 \frac{\partial u}{\partial \xi} - \frac{1}{2} h^2 \frac{\partial b}{\partial \xi} u \right] \frac{\partial}{\partial \xi} \left(\begin{bmatrix} \phi_{j-1/2} \\ \phi_j \\ \phi_{j+1/2} \end{bmatrix} \right) \right) d\xi.$$

We will demonstrate the rest of the process for the uh term as an example with the remaining integrals provided online (https://sites.google.com/view/jordanpitt/phd-thesis-resources/finite-element-integrals). The uh term is

$$\frac{\Delta x}{2} \int_{-1}^{1} uh \begin{bmatrix} \phi_{j-1/2} \\ \phi_j \\ \phi_{j+1/2} \end{bmatrix} d\xi.$$

Since the integral is computed over $[-1, 1]$, there are only a few non-zero contri-

butions from the finite element approximations to h and u, so we have

$$\frac{\Delta x}{2}\int_{-1}^{1}\Bigg(\left(u_{j-1/2}\phi_{j-1/2}+u_j\phi_j+u_{j+1/2}\phi_{j+1/2}\right)\times\left(h^+_{j-1/2}\psi^+_{j-1/2}+h^-_{j+1/2}\psi^-_{j+1/2}\right)\begin{bmatrix}\phi_{j-1/2}\\ \phi_j\\ \phi_{j+1/2}\end{bmatrix}\Bigg)d\xi$$

$$=\frac{\Delta x}{2}\Bigg(h^+_{j-1/2}\int_{-1}^{1}\psi^+_{j-1/2}\begin{bmatrix}\phi_{j-1/2}\phi_{j-1/2} & \phi_j\phi_{j-1/2} & \phi_{j+1/2}\phi_{j-1/2}\\ \phi_{j-1/2}\phi_j & \phi_j\phi_j & \phi_{j+1/2}\phi_j\\ \phi_{j+1/2}\phi_{j-1/2} & \phi_{j+1/2}\phi_j & \phi_{j+1/2}\phi_{j+1/2}\end{bmatrix}d\xi$$

$$+h^-_{j+1/2}\int_{-1}^{1}\psi^-_{j+1/2}\begin{bmatrix}\phi_{j-1/2}\phi_{j-1/2} & \phi_j\phi_{j-1/2} & \phi_{j+1/2}\phi_{j-1/2}\\ \phi_{j-1/2}\phi_j & \phi_j\phi_j & \phi_{j+1/2}\phi_j\\ \phi_{j+1/2}\phi_{j-1/2} & \phi_{j+1/2}\phi_j & \phi_{j+1/2}\phi_{j+1/2}\end{bmatrix}d\xi\Bigg)\begin{bmatrix}u_{j-1/2}\\ u_j\\ u_{j+1/2}\end{bmatrix}.$$

Calculating the integrals of all the basis function combinations we get

$$\frac{\Delta x}{2}\int_{-1}^{1}uh\begin{bmatrix}\phi_{j-1/2}\\ \phi_j\\ \phi_{j+1/2}\end{bmatrix}d\xi=$$

$$\frac{\Delta x}{60}\begin{bmatrix}7h^+_{j-1/2}+h^-_{j+1/2} & 4h^+_{j-1/2} & -h^+_{j-1/2}-h^-_{j+1/2}\\ 4h^+_{j-1/2} & 16h^+_{j-1/2}+16h^-_{j+1/2} & 4h^-_{j+1/2}\\ -h^+_{j-1/2}-h^-_{j+1/2} & 4h^-_{j+1/2} & h^+_{j-1/2}+7h^-_{j+1/2}\end{bmatrix}\begin{bmatrix}u_{j-1/2}\\ u_j\\ u_{j+1/2}\end{bmatrix}.$$

Assembly of the Global Matrix

By combining all the matrices generated by the integral of each of the u terms we get the contribution of the j^{th} cell to the stiffness matrix $\mathbf{A}_j$. Likewise all the integrals of the remaining term Gv in (3.5) generate the element wise vector $\boldsymbol{g}_j$. These element wise matrices and vectors are then assembled into the global stiffness matrix $\mathbf{A}$ and the global right hand-side term $\boldsymbol{g}$ thus (3.5) is rewritten as

$$\mathbf{A}\hat{\boldsymbol{u}}=\boldsymbol{g}. \tag{3.10}$$

This is a penta-diagonal matrix equation which can be solved by direct banded matrix solution techniques such as those of Press et al. [45] to obtain

$$\hat{\boldsymbol{u}}=\mathcal{G}\left(\hat{\boldsymbol{h}},\hat{\boldsymbol{G}},\hat{\boldsymbol{b}}\right)=\mathbf{A}^{-1}\boldsymbol{g} \tag{3.11}$$

as desired.

3.2.3 Flux Across the Cell Interfaces

We use the method of Kurganov et al. [46] to calculate the flux across a cell interface. This method was employed because it can handle discontinuities across the cell boundary and only requires an estimate of the maximum and minimum wave speeds. This is precisely the situation for the Serre equations which do not have a known expression for the characteristics but do possess estimates on the maximum and minimum wave speeds (2.10).

Only the calculation of the flux term $F_{j+1/2}$ is demonstrated as the process to calculate the flux term $F_{j-1/2}$ is identical but with different cells. For a general quantity q the approximation of the flux term given by Kurganov et al. [46] is

$$F_{j+\frac{1}{2}} = \frac{a^+_{j+\frac{1}{2}} f\left(q^-_{j+\frac{1}{2}}\right) - a^-_{j+\frac{1}{2}} f\left(q^+_{j+\frac{1}{2}}\right)}{a^+_{j+\frac{1}{2}} - a^-_{j+\frac{1}{2}}} + \frac{a^+_{j+\frac{1}{2}}\, a^-_{j+\frac{1}{2}}}{a^+_{j+\frac{1}{2}} - a^-_{j+\frac{1}{2}}} \left(q^+_{j+\frac{1}{2}} - q^-_{j+\frac{1}{2}}\right) \tag{3.12}$$

where $a^+_{j+\frac{1}{2}}$ and $a^-_{j+\frac{1}{2}}$ are given by bounds on the wave speed. Applying the wave speed bounds (2.10) we obtain

$$a^-_{j+\frac{1}{2}} = \min\left\{0\ ,\ u^-_{j+1/2} - \sqrt{gh^-_{j+1/2}}\ ,\ u^+_{j+1/2} - \sqrt{gh^+_{j+1/2}}\right\}, \tag{3.13}$$

$$a^+_{j+\frac{1}{2}} = \max\left\{0\ ,\ u^-_{j+1/2} + \sqrt{gh^-_{j+1/2}}\ ,\ u^+_{j+1/2} + \sqrt{gh^+_{j+1/2}}\right\}. \tag{3.14}$$

The flux functions $f(q^-_{j+\frac{1}{2}})$ and $f(q^+_{j+\frac{1}{2}})$ across the cell edge $x_{j+1/2}$ are evaluated using the reconstructed values $q^-_{j+\frac{1}{2}}$ from the j^{th} cell and $q^+_{j+\frac{1}{2}}$ from the $(j+1)^{th}$ cell. From the continuity equation (2.6a) we have

$$f\left(h^\pm_{j+\frac{1}{2}}\right) = u^\pm_{j+1/2} h^\pm_{j+1/2}.$$

For the evolution of G equation (2.6b) we have

$$\begin{aligned} f\left(G^\pm_{j+\frac{1}{2}}\right) = u^\pm_{j+1/2} G^\pm_{j+1/2} + \frac{g}{2}\left(h^\pm_{j+1/2}\right)^2 - \frac{2}{3}\left(h^\pm_{j+1/2}\right)^3 \left[\left(\frac{\partial u}{\partial x}\right)^\pm_{j+1/2}\right]^2 \\ + \left(h^\pm_{j+1/2}\right)^2 u^\pm_{j+1/2} \left(\frac{\partial u}{\partial x}\right)^\pm_{j+1/2} \left(\frac{\partial b}{\partial x}\right)^\pm_{j+1/2}. \end{aligned} \tag{3.15}$$

The quantities $h^+_{j-1/2}$, $h^-_{j+1/2}$, $G^+_{j-1/2}$ and $G^-_{j+1/2}$ were calculated during the reconstruction and the FEM provided $u^\pm_{j+1/2} = u_{j+1/2}$ as u is continuous across the cell boundaries.

Calculation of Derivatives

Approximations to $\left(\frac{\partial b}{\partial x}\right)^{\pm}_{j+1/2}$ and $\left(\frac{\partial u}{\partial x}\right)^{\pm}_{j+1/2}$ are now required to calculate the flux (3.15). To calculate these derivatives in u and b we use the basis function approximation to these quantities in the FEM to define the reconstruction polynomial of these quantities over a cell. For u we have the quadratic

$$P_j^u(x) = p_0^u (x - x_j)^2 + p_1^u (x - x_j) + p_2^u \tag{3.16}$$

that passes through $u_{j-1/2}$, u_j and $u_{j+1/2}$. While for b we have the cubic

$$P_j^b(x) = p_0^b (x - x_j)^3 + p_1^b (x - x_j)^2 + p_2^b (x - x_j) + p_3^b \tag{3.17}$$

that passes through $b_{j-1/2}$, $b_{j-1/6}$, $b_{j+1/6}$ and $b_{j+1/2}$. Because the cell edge values were averaged during the reconstruction of the bed, $P_j^b(x)$ will be different from $C_j(x)$.

For $P_j^u(x)$ we obtain the coefficients

$$\begin{aligned} p_0^u &= \frac{u_{j-1/2} - 2u_j + u_{j+1/2}}{2\Delta x^2}, \\ p_1^u &= \frac{-u_{j-1/2} + u_{j+1/2}}{\Delta x}, \\ p_2^u &= u_j. \end{aligned}$$

While for $P_j^b(x)$ the coefficients are

$$p_0^b = \frac{-9b_{j-1/2} + 27b_{j-1/6} - 27b_{j+1/6} + 9b_{j+1/2}}{2\Delta x^3},$$

$$p_0^b = \frac{9b_{j-1/2} - 9b_{j-1/6} - 9b_{j+1/6} + 9b_{j+1/2}}{4\Delta x^2},$$

$$p_0^b = \frac{b_{j-1/2} - 27b_{j-1/6} + 27b_{j+1/6} - b_{j+1/2}}{8\Delta x},$$

$$p_0^b = \frac{-b_{j-1/2} + 9b_{j-1/6} + 9b_{j+1/6} - b_{j+1/2}}{16}.$$

Taking the derivative of the polynomials (3.16) and (3.17) we get

$$\begin{aligned} \frac{\partial}{\partial x} P_j^u(x) &= 2p_0^u (x - x_j) + p_1^u, \\ \frac{\partial}{\partial x} P_j^b(x) &= 3p_0^b (x - x_j)^2 + 2p_1^b (x - x_j) + p_2^b. \end{aligned}$$

This gives a second-order approximation to the derivative of u and b at $x_{j+1/2}$ for the j^{th} cell. The process for the $(j+1)^{th}$ cell is the same and we get

$$\begin{aligned}
\left(\frac{\partial u}{\partial x}\right)^{-}_{j+1/2} &= \frac{\partial}{\partial x} P^{u}_{j}(x_{j+1/2}),\\
\left(\frac{\partial u}{\partial x}\right)^{+}_{j+1/2} &= \frac{\partial}{\partial x} P^{u}_{j+1}(x_{j+1/2}),\\
\left(\frac{\partial b}{\partial x}\right)^{-}_{j+1/2} &= \frac{\partial}{\partial x} P^{b}_{j}(x_{j+1/2}),\\
\left(\frac{\partial b}{\partial x}\right)^{+}_{j+1/2} &= \frac{\partial}{\partial x} P^{b}_{j+1}(x_{j+1/2}).
\end{aligned}$$

Therefore, we possess all the terms needed to calculate the approximation to the flux (3.12) for h and G, as desired. However, to ensure that the FEVM is well balanced and recovers the lake at rest steady state solution, these fluxes must be modified.

Well Balancing Modification to Flux Approximation

To recover the lake at rest steady state solution we follow the work of Audusse et al. [47], who accomplished this for the SWWE. Previously, we demonstrated that this process can be extended to the Serre equations [38]. To enforce well balancing the reconstruction of h is modified at the cell edges in the following way.

First calculate

$$\dot{b}^{-}_{j+1/2} = w^{-}_{j+1/2} - h^{-}_{j+1/2}, \qquad \dot{b}^{+}_{j+1/2} = w^{+}_{j+1/2} - h^{+}_{j+1/2}. \tag{3.18}$$

Find the maximum

$$\ddot{b}_{j+1/2} = \max\left\{\dot{b}^{-}_{j+1/2}, \dot{b}^{+}_{j+1/2}\right\}$$

then define

$$\ddot{h}^{-}_{j+1/2} = \max\left\{0, w^{-}_{j+1/2} - \ddot{b}_{j+1/2}\right\}, \tag{3.19a}$$

$$\ddot{h}^{+}_{j+1/2} = \max\left\{0, w^{+}_{j+1/2} - \ddot{b}_{j+1/2}\right\}. \tag{3.19b}$$

This generates the vector $\ddot{\boldsymbol{h}}$

$$\ddot{\boldsymbol{h}} = \begin{bmatrix} \ddot{h}^{+}_{-1/2} \\ h_0 \\ \ddot{h}^{-}_{1/2} \\ \vdots \\ \ddot{h}^{-}_{m+1/2} \end{bmatrix}$$

which we use to calculate the flux term $F_{j+1/2}$ in (3.12) for h and G instead of $\hat{\boldsymbol{h}}$. Applying the same process but with different cells we obtain $F_{j-1/2}$ and we have

$$F^n_{j\pm1/2} = \mathcal{F}_{j\pm1/2}\left(\ddot{\boldsymbol{h}}, \hat{\boldsymbol{G}}, \hat{\boldsymbol{b}}, \hat{\boldsymbol{u}}\right).$$

for the evolution of h and G equations as desired.

3.2.4 Source Terms

To evolve the Serre equations (2.6), we require an approximation to the source term at the cell centre x_j which we denote as S_j. Equation (2.6a) has no source term, therefore we just present the calculation of the source term for equation (2.6b).

Following the work of Audusse et al. [47] to produce a well-balanced method, we split our approximation to S^n_j into the centred source term S_{ci} and the corrective interface source terms $S^-_{j+\frac{1}{2}}$ and $S^+_{j+\frac{1}{2}}$

$$S^n_j = S^-_{j+\frac{1}{2}} + \Delta x S_{ci} + S^+_{j-\frac{1}{2}}.$$

Where S_{ci} is the naive source term approximation and $S^-_{j+\frac{1}{2}}$ and $S^+_{j+\frac{1}{2}}$ are correction terms that ensure that the flux and source term cancel for the lake at rest solution.

We calculate the centred source term using

$$S_{ci} = -\frac{1}{2}\left(h_j\right)^2 u_j \left(\frac{\partial u}{\partial x}\right)_j \left(\frac{\partial^2 b}{\partial x^2}\right)_j + h_j \left(u_j\right)^2 \left(\frac{\partial b}{\partial x}\right)_j \left(\frac{\partial^2 b}{\partial x^2}\right)_j - g h_j \left(\frac{\partial b}{\partial x}\right)_j.$$

Where we use h_j from the reconstruction process (3.1) and u_j from the solution of (3.11). To calculate the derivatives we employ our polynomial representations of u (3.16) and b (3.17) inside a cell. However, to ensure that the terms cancel properly for a lake at rest we modify our approximation to $\dfrac{\partial b}{\partial x}$ to use $\dot{b}^-_{j+1/2}$ and

$\dot{b}^+_{j+1/2}$ from (3.18). Therefore, the following approximations are used to calculate S_{ci}

$$\left(\frac{\partial u}{\partial x}\right)_j = \frac{\partial}{\partial x} P^u_j(x_j),$$
$$\left(\frac{\partial b}{\partial x}\right)_j = \frac{\dot{b}^-_{j+1/2} - \dot{b}^+_{j-1/2}}{\Delta x},$$
$$\left(\frac{\partial^2 b}{\partial x^2}\right)_j = \frac{\partial^2}{\partial x^2} P^b_j(x_j).$$

To ensure well-balancing the corrective interface source terms

$$S^-_{j+\frac{1}{2}} = \frac{g}{2}\left(\ddot{h}^-_{j+\frac{1}{2}}\right)^2 - \frac{g}{2}\left(h^-_{j+\frac{1}{2}}\right)^2,$$

$$S^+_{j-\frac{1}{2}} = \frac{g}{2}\left(h^+_{j-\frac{1}{2}}\right)^2 - \frac{g}{2}\left(\ddot{h}^+_{j-\frac{1}{2}}\right)^2$$

are also added. These corrective terms make use of $h^-_{j+\frac{1}{2}}$ and $h^+_{j+\frac{1}{2}}$ obtained from the reconstruction (3.1) and the modified values $\ddot{h}^-_{j+\frac{1}{2}}$ and $\ddot{h}^+_{j+\frac{1}{2}}$ from (3.19). Combining the centred and interface source terms our approximation to the source term for G is

$$S^n_j = \mathcal{S}_j\left(\hat{\boldsymbol{h}}, \ddot{\boldsymbol{h}}, \hat{\boldsymbol{w}}, \hat{\boldsymbol{b}}, \hat{\boldsymbol{u}}\right) = S^-_{j+\frac{1}{2}} + \Delta x S_{ci} + S^+_{j-\frac{1}{2}}.$$

3.2.5 Update Cell Averages

Applying a forward Euler approximation with our approximation to the flux and source terms we get that

$$\overline{q}^{n+1}_j = \overline{q}^n_j + \frac{\Delta t}{\Delta x}\left(F^n_{j+\frac{1}{2}} - F^n_{j-\frac{1}{2}} + S^n_j\right) \tag{3.20}$$

where $F^n_{j+\frac{1}{2}}$, $F^n_{j-\frac{1}{2}}$ and S^n_j are all calculated using the quantities at time t^n. This update formula is first-order in time.

3.2.6 Second-Order SSP Runge-Kutta Method

To increase the order of accuracy in time we employ the strong stability preserving Runge-Kutta method [48] which is a convex combination of the first-order time

steps (3.20) in the following way

$$\overline{q}_j^{(1)} = \overline{q}_j^n + \frac{\Delta t}{\Delta x}\left(F^n_{j+\frac{1}{2}} - F^n_{j-\frac{1}{2}} + S^n_j\right), \tag{3.21a}$$

$$\overline{q}_j^{(2)} = \overline{q}_j^{(1)} + \frac{\Delta t}{\Delta x}\left(F^{(1)}_{j+\frac{1}{2}} - F^{(1)}_{j-\frac{1}{2}} + S^{(1)}_j\right), \tag{3.21b}$$

$$\overline{q}_j^{n+1} = \frac{1}{2}\left(\overline{q}_j^n + \overline{q}_j^{(2)}\right). \tag{3.21c}$$

This results in a time stepping method that preserves the stability of the first-order method (3.20) and is second-order accurate in time. Since all the spatial approximations are second-order accurate, the steps (i-vi) should result in a second-order accurate FEVM for the Serre equations, as desired.

3.3 CFL condition

To ensure the stability of our FEVM we use the Courant-Friedrichs-Lewy (CFL) condition [49] which is necessary for stability. The CFL condition ensures that time steps are small enough so that information is only transferred between neighbouring cells. For the Serre equations the CFL condition is

$$\Delta t \leq \frac{Cr}{\max_j\left\{a^{\pm}_{j+1/2}\right\}}\Delta x \tag{3.22}$$

where $a^{\pm}_{j+1/2}$ are the wave-speed bounds used in the flux approximation (3.14) and $0 \leq Cr \leq 1$ is the Courant number. Typically, we use the conservative $Cr = 0.5$ for our numerical experiments.

3.4 Boundary Conditions

To numerically model the Serre equations over finite spatial domains we must enforce boundary conditions at the left and right edge of the domain; $x_{-1/2}$ and $x_{m+1/2}$ respectively. We have only developed Dirichlet boundary conditions for the FEVM, which we enforce using ghost cells located outside the domain boundaries. These ghost cells contain the complete representation of their respective quantities over the cell. For h, w, G and u only one ghost cell at each boundary is required, while for b we require two ghost cells at each boundary. The ghost

cells for h, w and G written for a generic quantity q are

$$\hat{\boldsymbol{q}}_{-1} = \begin{bmatrix} q^+_{-3/2} \\ q_{-1} \\ q^-_{-1/2} \end{bmatrix}, \qquad \hat{\boldsymbol{q}}_{m+1} = \begin{bmatrix} q^+_{m+1/2} \\ q_{m+1} \\ q^-_{m+3/2} \end{bmatrix}.$$

For u and b the ghost cells are

$$\hat{\boldsymbol{u}}_{-1} = \begin{bmatrix} u_{-3/2} \\ u_{-1} \\ u_{-1/2} \end{bmatrix}, \qquad \hat{\boldsymbol{u}}_{m+1} = \begin{bmatrix} u_{m+1/2} \\ u_{m+1} \\ u_{m+3/2} \end{bmatrix},$$

$$\hat{\boldsymbol{b}}_{-2} = \begin{bmatrix} b_{-5/2} \\ b_{-13/6} \\ b_{-11/6} \\ b_{-3/2} \end{bmatrix}, \quad \hat{\boldsymbol{b}}_{-1} = \begin{bmatrix} b_{-3/2} \\ b_{-7/6} \\ b_{-5/6} \\ b_{-1/2} \end{bmatrix}, \quad \hat{\boldsymbol{b}}_{m+1} = \begin{bmatrix} b_{m+1/2} \\ b_{m+5/6} \\ b_{m+7/6} \\ b_{m+3/2} \end{bmatrix}, \quad \hat{\boldsymbol{b}}_{m+2} = \begin{bmatrix} b_{m+3/2} \\ b_{m+11/6} \\ b_{m+13/6} \\ b_{m+5/2} \end{bmatrix}.$$

To ensure that the solution of u by (3.11) agrees with the boundary conditions $\hat{\boldsymbol{u}}_{-1}$ and $\hat{\boldsymbol{u}}_m$ the element-wise stiffness matrices $\mathbf{A}_0$ and $\mathbf{A}_m$ and vectors $\boldsymbol{g}_0$ and $\boldsymbol{g}_m$ must be modified in the following way

$$\mathbf{A}_0 = \begin{bmatrix} 1 & 0 & 0 \\ a_{21} & a_{22} & a_{23} \\ a_{31} & a_{32} & a_{33} \end{bmatrix}, \qquad \boldsymbol{g}_0 = \begin{bmatrix} u_{-1/2} \\ g_1 \\ g_2 \end{bmatrix},$$

$$\mathbf{A}_m = \begin{bmatrix} a_{11} & a_{12} & a_{13} \\ a_{21} & a_{22} & a_{23} \\ 0 & 0 & 1 \end{bmatrix}, \qquad \boldsymbol{g}_m = \begin{bmatrix} g_0 \\ g_1 \\ u_{m+1/2} \end{bmatrix}.$$

These are then assembled with the other element contributions in the global stiffness matrix $\mathbf{A}$ and right hand side vector $\boldsymbol{g}$ in (3.10).

3.5 Dry Beds

Dry beds are handled adequately by all steps of the FEVM in their current form, except the FEM for u. The dry bed presents two issues; when h and G are small then small errors in h and G can produce large errors in u leading to instabilities and when $h = 0$ the stiffness matrix $\mathbf{A}$ (3.11) becomes singular.

The issue of large errors in u when h is small also arises when solving the SWWE; due to $u = (uh)/h$ being undefined as uh and h go to zero. For the Serre equations with horizontal beds when $h \ll 1$ from (2.8c) we have

$$G = uh + \mathcal{O}\left(h^3\right). \tag{3.23}$$

Since $h \ll 1$ we neglect the $\mathcal{O}\left(h^3\right)$ terms, and thus when h is small G is equal to the momentum uh, and the challenges posed by $h \to 0$ for the SWWE and the Serre equations are equivalent. Therefore, we can apply the dry bed handling techniques from the SWWE to the Serre equations; in particular a desingularisation transformation [50].

These desingularisation transforms act by modifying the calculation of u given h and uh to avoid the singularity as the numerator and denominator go to zero, hence their name. The simplest such transformation is

$$u = \frac{(uh)h}{h\left(h + h_{base}\right)} \tag{3.24}$$

where h_{base} is some small chosen parameter. The error introduced by this transformation is smallest when h_{base} is smallest. However, as noted by Kurganov and Petrova [50] small values of h_{base} lead to large numerical errors in the calculation of u. To avoid such errors h_{base} can be made larger or following Kurganov and Petrova [50] different desingularisation transforms can be employed. For the main purpose of this thesis; the validation tests reported in Chapter 5 we found the simpler transformation with small values of h_{base} more useful, keeping in mind that large numerical errors in u were possible for small values of h.

To adapt the calculation of u in (3.24) to (2.7) we view it as a transformation of the quantity h which is equivalent to

$$h \to h\left(\frac{h + h_{base}}{h}\right). \tag{3.25}$$

This transformation is ill-defined when $h = 0$ so we also add in a small term h_{tol} to the denominator; this h_{tol} also serves as our cut-off value with any cells with $h < h_{tol}$ being considered dry. Therefore, our transformation for the reconstructed values of h in the finite element method is

$$h^+_{j-1/2} = h^+_{j-1/2}\left(\frac{h^+_{j-1/2} + h_{base}}{h^+_{j-1/2} + h_{tol}}\right), \tag{3.26a}$$

$$h^-_{j+1/2} = h^-_{j+1/2}\left(\frac{h^-_{j+1/2} + h_{base}}{h^-_{j+1/2} + h_{tol}}\right) \tag{3.26b}$$

where on the right hand side are the reconstructed values of h from (3.1) and the left hand side are the values of h used to defined the basis functions of the finite element method (3.6). This transformation is applied to all terms in the FEM avoiding the singularity as $h \to 0$; and in the case where $G = uh$ the transformation is equivalent to (3.24) for the SWWE.

Even with the transform (3.26), the matrix $\mathbf{A}$ can become singular. The methods of Zoppou et al. [15] made use of direct banded matrix solvers such as the Thomas algorithm [51] to solve (3.11) which rely on non-singular matrices making them unsuitable when $h = 0$. This was resolved by employing an LU decomposition algorithm described by Press et al. [45]. This algorithm solves banded matrix problems using an LU decomposition with partial pivoting, which inserts small non-zero pivots when the pivots value is below some tolerance value p_{tol}. It does this while also keeping the banded matrix structure, and so is not as memory intensive as a standard LU decomposition. Typically we set $p_{tol} = 10^{-20}$ allowing the matrix solver to accurately invert $\mathbf{A}$ and thus solve (3.11) when $h = 0$.

Finally, after solving (3.11) using the LU decomposition algorithm of Press et al. [45] where the transformation (3.26) has been applied to the reconstructed values of h we possess an approximation to u in the presence of dry beds. Additionally to avoid numerical errors becoming dominant when h is very small we place a cut-off on h past which $h = G = u = 0$ and the cells are properly dry; this is given by h_{tol}. This drying of the cells is performed for the whole cell based on the cell average value of h so that if $\overline{h}_j \leq h_{tol}$ then

$$\begin{aligned} h^+_{j-1/2} &= 0 & G^+_{j-1/2} &= 0 & w^+_{j-1/2} &= b_{j-1/2} \\ h_j &= 0 & G_j &= 0 & w_j &= b_j, \\ h^-_{j+1/2} &= 0 & G^-_{j+1/2} &= 0 & w^-_{j+1/2} &= b_{j+1/2} \end{aligned}$$

and

$$\begin{aligned} u_{j-1/2} &= 0 && \text{if} && h_{j-1} \leq h_{tol} \\ u_j &= 0 \\ u_{j+1/2} &= 0 && \text{if} && h_{j+1} \leq h_{tol} \end{aligned}$$

this drying procedure occurs after the solution of (3.11). In the numerical experiments the typical values used were $h_{tol} = 10^{-12}$ and $h_{base} = 10^{-8}$.

In this chapter FEVM$_2$ was described, including the details for the well balancing and dry bed handling procedures.

Chapter 4

Linear Analysis

In this chapter a linear analysis is used to study the convergence and dispersion properties of the numerical methods.

An important property of a numerical method is convergence. Convergence guarantees that as the spatial and temporal resolution of a numerical method is increased, then the numerical solution approaches the solution of the partial differential equations it approximates.

For linear partial differential equations the Lax-equivalence theorem states that a numerical method is convergent if and only if it is stable and consistent [52]. A numerical scheme is consistent if the error introduced by the numerical method over a time step approaches zero as the spatial and temporal resolution increases. A numerical method is stable if the errors from previous time steps are not amplified over subsequent time steps.

Another important attribute of a numerical method modelling dispersive wave equations, such as the Serre equations is its dispersion properties. The dispersion relation of a system determines the phase and group velocity of travelling waves in that system. The Serre equations possess a dispersion relation that well approximates the dispersion relation given by linear theory for water waves [21]. Therefore, how well the dispersion relation of a numerical method approximates the dispersion relation of the Serre equations is of particular interest.

We analysed the convergence and dispersion properties of the whole numerical method applied to the solution of the linearised Serre equations with a horizontal bed. The whole scheme is considered with the spatial and temporal approximations analysed simultaneously. The effect of variations in the bed and non-linear terms are important when studying the convergence properties of our methods for solving the full Serre equations. However, these effects greatly increase the

complexity of the convergence analysis. We therefore, estimate the convergence properties of the non-linear Serre equations with varying bathymetry by investigating the linearised Serre equations with a horizontal bed.

In general, we would expect that a numerical method that has poor convergence properties for the linearised Serre equations with a horizontal bed will also have poor convergence properties when the bed and non-linear terms are included.

The dispersion properties of the Serre equations are derived from the linearised Serre equations with a horizontal bed [15]. Because the dispersion analysis includes the spatial and temporal approximations simultaneously the presented analysis of dispersion properties of the numerical method is a complete analysis extending the work of Filippini et al. [37].

The linear analyses of convergence and dispersion properties for the finite volume based methods rely on establishing a relationship of the form

$$\begin{bmatrix} \overline{h} \\ \overline{G} \end{bmatrix}_j^{n+1} = \mathbf{E} \begin{bmatrix} \overline{h} \\ \overline{G} \end{bmatrix}_j^{n} \tag{4.1}$$

where $\mathbf{E}$ is the 2×2 evolution matrix relating the cell average conserved quantities h and G at time level t^n with the cell average conserved quantities at time level t^{n+1}, which is independent of n and j. The evolution matrix $\mathbf{E}$ is obtained in the analyses by propagating Fourier modes through the numerical scheme. By analysing the properties of $\mathbf{E}$ and comparing it with the exact evolution matrix we can determine the convergence and dispersion properties of its associated numerical method.

We derive $\mathbf{E}$ in (4.1) for FEVM_2 and perform the convergence and dispersion analysis. We then present the results of the analyses for the finite difference volume methods FDVM_1, FDVM_2 and FDVM_3 described by Zoppou et al. [15] and the finite difference methods $\mathcal{D}$ and $\mathcal{W}$ described by Pitt et al. [14]. These results extend those published by Zoppou et al. [15] by including more methods, analysing the convergence properties and allowing non-zero background mean velocities.

4.1 Linearised Serre Equations

The Serre equations with a horizontal bed (2.5) are linearised by considering waves as small perturbations $\delta \times \eta(x,t)$ and $\delta \times \mu(x,t)$ on a flow with a mean

height H and a mean velocity U respectively, where $\delta \ll 1$. So we have

$$h(x,t) = H + \delta\eta(x,t) + \mathcal{O}\left(\delta^2\right), \tag{4.2a}$$
$$u(x,t) = U + \delta\mu(x,t) + \mathcal{O}\left(\delta^2\right). \tag{4.2b}$$

These waves are relatively small so terms of order δ^2 are negligible. We substitute (4.2) into the Serre equations and neglect terms of order δ^2 to obtain

$$\frac{\partial(\delta\eta)}{\partial t} + H\frac{\partial(\delta\mu)}{\partial x} + U\frac{\partial(\delta\eta)}{\partial x} = 0, \tag{4.3a}$$
$$H\frac{\partial(\delta\mu)}{\partial t} + gH\frac{\partial(\delta\eta)}{\partial x} + UH\frac{\partial(\delta\mu)}{\partial x} - \frac{H^3}{3}\left(U\frac{\partial^3(\delta\mu)}{\partial x^3} + \frac{\partial^3(\delta\mu)}{\partial x^2\partial t}\right) = 0 \tag{4.3b}$$

and for G

$$G = UH + U\delta\eta + H\delta\mu - \frac{H^3}{3}\frac{\partial^2(\delta\mu)}{\partial x^2}. \tag{4.3c}$$

Absorbing the δ factor into corresponding η and μ terms and rewritting these equations in conservation law form for η and G we obtain

$$\frac{\partial\eta}{\partial t} + \frac{\partial}{\partial x}(H\mu + U\eta) = 0, \tag{4.4a}$$
$$\frac{\partial G}{\partial t} + \frac{\partial}{\partial x}(UG + UH\mu + gH\eta) = 0 \tag{4.4b}$$

where

$$G = UH + U\eta + H\mu - \frac{H^3}{3}\frac{\partial^2\mu}{\partial x^2}. \tag{4.4c}$$

4.2 Evolution Matrix

To derive the evolution matrix, $\mathbf{E}$ we study the behaviour of (4.4) when η and μ are Fourier modes. A Fourier mode $q(x,t)$ is

$$q(x,t) = q(0,0)e^{i\left(\omega^{\pm}t + kx\right)} \tag{4.5}$$

where k is the wavenumber, $\omega^{\pm}$ is the frequency (2.9) and i is the imaginary number. The Fourier modes are the eigenfunctions of these linearised Serre equations (4.4). Since the eigenfunctions form a basis of the solution space, their dispersion and convergence properties are inherited by all solutions of (4.4). Therefore, it is sufficient to study only the convergence and dispersion properties for Fourier mode solutions captured by the evolution matrix $\mathbf{E}$.

A consequence of a quantity q being a Fourier mode represented on a uniform temporal and spatial grid is that for any real numbers m and l we have

$$q_{j+l}^{n+m} = q_j^n e^{i\left(m\omega^{\pm}\Delta t + lk\Delta x\right)}. \tag{4.6}$$

Because η and μ are Fourier modes then so is G. Furthermore, the cell averages of these quantities $\overline{\eta}$, $\overline{\mu}$ and $\overline{G}$ are Fourier modes as well.

For Fourier modes the operators $\mathcal{R}^+_{j-1/2}$, $\mathcal{R}_j$, $\mathcal{R}^-_{j+1/2}$, $\mathcal{G}$, $\mathcal{F}_{j-1/2}$ and $\mathcal{F}_{j+1/2}$ from Chapter 3 will only vary with H, U, k, $\omega^{\pm}$, Δx and Δt and hence are independent of j and n. By combining these operators the evolution matrix $\mathbf{E}$ can be derived for FEVM_2 for the linearised Serre equations with a horizontal bed. Since all the constituent operators of $\mathbf{E}$ are independent of j and n then $\mathbf{E}$ will also be independent of j and n, as desired. We will now derive expressions for all these operators, following the structure of the method laid out in Section 3.2. Since the linearised Serre equations with a horizontal bed have no source terms step (iv), which approximates the source terms is not necessary.

4.2.1 Reconstruction

Given the cell averages $\overline{\boldsymbol{\eta}}$ and $\overline{\boldsymbol{G}}$ at t^n, the first step of our numerical method is to reconstruct η and G inside the j^{th} cell at $x_{j-1/2}$, x_j and $x_{j+1/2}$ using $\mathcal{R}^+_{j-1/2}$, $\mathcal{R}_j$ and $\mathcal{R}^-_{j+1/2}$ from (3.1). Since η and G are Fourier modes and therefore smooth we do not require non-linear limiters to ensure our scheme is TVD and so we use the slope $d_j = \left(-\bar{q}_{j-1} + \bar{q}_{j+1}\right)/\left(2\Delta x\right)$ in the reconstruction. Applying (4.6) to the reconstructions (3.1) with the centred slope approximation we obtain

$$q^+_{j-\frac{1}{2}} = \overline{q}_j - \frac{-\overline{q}_j e^{-ik\Delta x} + \overline{q}_j e^{ik\Delta x}}{4} = \left(1 - \frac{i\sin\left(k\Delta x\right)}{2}\right)\overline{q}_j = \mathcal{R}^+_{j-1/2}\overline{q}_j, \tag{4.7a}$$

$$q_j = \bar{q}_j = \mathcal{R}_j \bar{q}_j, \tag{4.7b}$$

$$q^-_{j+\frac{1}{2}} = \overline{q}_j + \frac{-\overline{q}_j e^{-ik\Delta x} + \overline{q}_j e^{ik\Delta x}}{4} = \left(1 + \frac{i\sin\left(k\Delta x\right)}{2}\right)\overline{q}_j = \mathcal{R}^-_{j+1/2}\overline{q}_j. \tag{4.7c}$$

Note that these reconstructions operators $\mathcal{R}^+_{j-1/2}$, $\mathcal{R}_j$ and $\mathcal{R}^-_{j+1/2}$ are independent of j. Furthermore, from (4.6) we have that reconstructions of η and G at other locations are translations of $\mathcal{R}^+_{j-1/2}$, $\mathcal{R}_j$ and $\mathcal{R}^-_{j+1/2}$. In particular, we have that the reconstruction operator $\mathcal{R}^+_{j+1/2}$ for $q^+_{j+\frac{1}{2}}$ is given by

$$q^+_{j+\frac{1}{2}} = e^{ik\Delta x} q^+_{j-\frac{1}{2}} = e^{ik\Delta x}\mathcal{R}^+_{j-1/2}\overline{q}_j = \mathcal{R}^+_{j+1/2}\overline{q}_j. \tag{4.7d}$$

4.2.2 Fluid Velocity

To calculate the velocity perturbation $\mu_{j+1/2}$ we use a second-order FEM. We begin with the weak formulation of (4.4c), obtained by multiplying (4.4c) by a test function v and integrating over the spatial domain Ω

$$\int_\Omega Gv\,dx = UH\int_\Omega v\,dx + U\int_\Omega \eta v\,dx + H\int_\Omega \mu v\,dx + \frac{H^3}{3}\int_\Omega \frac{\partial \mu}{\partial x}\frac{\partial v}{\partial x}\,dx.$$

The FEM then proceeds for (4.4) as in Chapter 3 for the non-linear Serre equation. So that G has the basis functions $\psi^+_{j-1/2}$ and $\psi^-_{j+1/2}$ (B.1), which means our approximation to G is linear inside a cell with discontinuous jumps at the cell edges. For v and μ the basis functions $\phi_{j-1/2}$, ϕ_j and $\phi_{j+1/2}$ (B.2) are used so that v and our approximation to μ are quadratic polynomials inside a cell and are continuous across the cell edges.

Given the detailed description of the method in Chapter 3, we will just present the element wise matrix $\mathbf{A}_j$ and vector $\boldsymbol{g}_j$ for the finite element approximation to (4.4)

$$\mathbf{A}_j = H\frac{\Delta x}{30}\begin{bmatrix} 4 & 2 & -1 \\ 2 & 16 & 2 \\ -1 & 2 & 4 \end{bmatrix} + \frac{H^3}{3}\frac{1}{3\Delta x}\begin{bmatrix} 7 & -8 & 1 \\ -8 & 16 & -8 \\ 1 & -8 & 7 \end{bmatrix},$$

$$\boldsymbol{g}_j = \frac{\Delta x}{6}\left(\begin{bmatrix} G^+_{j-1/2} \\ 2G^+_{j-1/2} + 2G^-_{j+1/2} \\ G^-_{j+1/2} \end{bmatrix} - UH\begin{bmatrix} 1 \\ 4 \\ 1 \end{bmatrix} - U\begin{bmatrix} \eta^+_{j-1/2} \\ 2\eta^+_{j-1/2} + 2\eta^-_{j+1/2} \\ \eta^-_{j+1/2} \end{bmatrix}\right).$$

To calculate the intercell flux we require μ at $x_{j+1/2}$. From the element wise matrices and vectors for the j and $(j+1)^{th}$ cells the equation that relates all the quantities at $x_{j+1/2}$ is

$$\begin{aligned}\frac{\Delta x}{6}\left(G^-_{j+1/2} + G^+_{j+1/2}\right) = & \\ & 2UH\frac{\Delta x}{6} + U\frac{\Delta x}{6}\left(\eta^-_{j+1/2} + \eta^+_{j+1/2}\right) \\ & + \left(H\frac{\Delta x}{30}\left[-\mu_{j-1/2} + 2\mu_j + 8\mu_{j+1/2} + 2\mu_{j+1} - \mu_{j+3/2}\right]\right. \\ & \left. + \frac{H^3}{3}\frac{1}{3\Delta x}\left[\mu_{j-1/2} - 8\mu_j + 14\mu_{j+1/2} - 8\mu_{j+1} + \mu_{j+3/2}\right]\right).\end{aligned}$$

Using (4.7) and (4.6), we obtain

$$\frac{\Delta x}{6}\left(\mathcal{R}^-_{j+1/2}+\mathcal{R}^+_{j+1/2}\right)\overline{G}_j = 2UH\frac{\Delta x}{6}+U\frac{\Delta x}{6}\left(\mathcal{R}^-_{j+1/2}+\mathcal{R}^+_{j+1/2}\right)\overline{\eta}_j + \left(H\frac{\Delta x}{30}\left[-e^{-ik\Delta x}+2e^{-ik\frac{\Delta x}{2}}+8+2e^{ik\frac{\Delta x}{2}}-e^{ik\Delta x}\right] + \frac{H^3}{3}\frac{1}{3\Delta x}\left[e^{-ik\Delta x}-8e^{-ik\frac{\Delta x}{2}}+14-8e^{ik\frac{\Delta x}{2}}+e^{ik\Delta x}\right]\right)\mu_{j+1/2}.$$

Rearranging the equation we have that

$$\mu_{j+1/2} = \mathcal{G}^\eta\overline{\eta}_j + \mathcal{G}^G\overline{G}_j + \mathcal{G}^c \tag{4.8}$$

where

$$\mathcal{G}^\eta = -U\mathcal{G}^G,$$

$$\mathcal{G}^G = \frac{\Delta x}{6\mathcal{G}_D}\left(\mathcal{R}^-_{j+1/2}+\mathcal{R}^+_{j+1/2}\right),$$

$$\mathcal{G}^c = -2UH\frac{\Delta x}{6\mathcal{G}_D}$$

and the common divisor $\mathcal{G}_D$ is

$$\mathcal{G}_D = H\frac{\Delta x}{30}\left(4\cos\left(\frac{k\Delta x}{2}\right)-2\cos\left(k\Delta x\right)+8\right) + \frac{H^3}{3}\frac{1}{3\Delta x}\left(-16\cos\left(\frac{k\Delta x}{2}\right)+2\cos\left(k\Delta x\right)+14\right).$$

So that the factors $\mathcal{G}^\eta$, $\mathcal{G}^G$ $\mathcal{G}^c$ do not depend on n or j as desired.

4.2.3 Flux Across the Cell Interfaces

The average intercell flux $F_{j+1/2}$ is approximated using (3.12). For the linearised Serre equations we have the wave speed bounds (2.10), so that

$$a^-_{j+1/2} = \min\left\{0, U-\sqrt{gH}\right\}, \qquad a^+_{j+1/2} = \max\left\{0, U+\sqrt{gH}\right\}. \tag{4.9}$$

This method has three different approximations to $F_{j+1/2}$ depending on the Froude number $Fr = \dfrac{U}{\sqrt{gH}}$; (i) supercritical flow to the left where $Fr < -1$,

(ii) critical and subcritical flow in both directions where $-1 \leq Fr \leq 1$ and (iii) supercritical flow to the right where $Fr > 1$. We will derive the flux operators for each of these cases separately.

Left Supercritical Flow $Fr < -1$:

For left supercritical flow; $Fr < -1$ and therefore $U + \sqrt{gH} < 0$ so we have from (4.9) that $a^-_{j+1/2} = U - \sqrt{gH}$ and $a^+_{j+1/2} = 0$. For these values the flux approximation reduces to the upwind approximation

$$F_{j+\frac{1}{2}} = f\left(q^+_{j+\frac{1}{2}}\right) \tag{4.10}$$

for a generic quantity q.

Substituting the flux function from the continuity equation (4.4a) into the flux approximation we obtain

$$F^\eta_{j+\frac{1}{2}} = H\mu_{j+1/2} + U\eta^+_{j+1/2}$$

since μ is continuous $\mu_{j+1/2} = \mu^+_{j+1/2} = \mu^-_{j+1/2}$.

Using the FEM for $\mu_{j+1/2}$ (4.8) and the reconstruction (4.7) we have

$$\begin{aligned} F^\eta_{j+\frac{1}{2}} &= H\left(\mathcal{G}^\eta\overline{\eta}_j + \mathcal{G}^G\overline{G}_j + \mathcal{G}^c\right) + U\eta^+_{j+1/2} \\ &= \left(H\mathcal{G}^\eta + U\mathcal{R}^+_{j+1/2}\right)\overline{\eta}_j + H\mathcal{G}^G\overline{G}_j + H\mathcal{G}^c. \end{aligned}$$

This can be written as coefficients for $\overline{\eta}_j$ and $\overline{G}_j$ like so

$$F^\eta_{j+\frac{1}{2}} = \mathcal{F}^{\eta,\eta}_{j+\frac{1}{2}}\overline{\eta}_j + \mathcal{F}^{\eta,G}_{j+\frac{1}{2}}\overline{G}_j + \mathcal{F}^{\eta,c}_{j+\frac{1}{2}}$$

where

$$\begin{aligned} \mathcal{F}^{\eta,\eta}_{j+\frac{1}{2}} &= H\mathcal{G}^\eta + U\mathcal{R}^+_{j+1/2}, \\ \mathcal{F}^{\eta,G}_{j+\frac{1}{2}} &= H\mathcal{G}^G, \\ \mathcal{F}^{\eta,c}_{j+\frac{1}{2}} &= H\mathcal{G}^c. \end{aligned}$$

Substituting the flux function for the G equation (4.4b) into the flux approximation (4.10) we obtain

$$F^G_{j+\frac{1}{2}} = UG^+_{j+1/2} + UH\mu_{j+1/2} + gH\eta^+_{j+1/2}.$$

Using the FEM (4.8) to calculate $\mu_{j+1/2}$ and our interface reconstruction (4.7) we have

$$F^G_{j+\frac{1}{2}} = UG^+_{j+1/2} + UH\left(\mathcal{G}^\eta\overline{\eta}_j + \mathcal{G}^G\overline{G}_j + \mathcal{G}^c\right) + gH\eta^+_{j+1/2}$$

which can be rewritten as

$$F^G_{j+\frac{1}{2}} = \mathcal{F}^{G,\eta}_{j+\frac{1}{2}}\overline{\eta}_j + \mathcal{F}^{G,G}_{j+\frac{1}{2}}\overline{G}_j + \mathcal{F}^{G,c}_{j+\frac{1}{2}}$$

where

$$\begin{aligned}
\mathcal{F}^{G,\eta}_{j+\frac{1}{2}} &= UH\mathcal{G}^\eta + gH\mathcal{R}^+_{j+1/2},\\
\mathcal{F}^{G,G}_{j+\frac{1}{2}} &= U\mathcal{R}^+_{j+1/2} + UH\mathcal{G}^G,\\
\mathcal{F}^{G,c}_{j+\frac{1}{2}} &= UH\mathcal{G}^c.
\end{aligned}$$

Subcritical Flow $-1 \leq Fr \leq 1$:

When the flow is subcritical we have $-1 \leq Fr \leq 1$, which means that $a^-_{j+1/2} = U - \sqrt{gH}$ and $a^+_{j+1/2} = U + \sqrt{gH}$. Therefore, the flux approximation (3.12) becomes

$$\begin{aligned}
F_{j+\frac{1}{2}} = \frac{U}{2\sqrt{gH}}\left[f\left(q^-_{j+\frac{1}{2}}\right) - f\left(q^+_{j+\frac{1}{2}}\right)\right] + \frac{1}{2}\left[f\left(q^-_{j+\frac{1}{2}}\right) + f\left(q^+_{j+\frac{1}{2}}\right)\right]\\
+ \frac{U^2 - gH}{2\sqrt{gH}}\left[q^+_{j+\frac{1}{2}} - q^-_{j+\frac{1}{2}}\right].
\end{aligned} \tag{4.11}$$

Substituting in the flux function for η given by (4.4a) we get

$$\begin{aligned}
F^\eta_{j+\frac{1}{2}} = \frac{U}{2\sqrt{gH}}\left(H\mu_{j+1/2} + U\eta^-_{j+\frac{1}{2}} - H\mu_{j+1/2} - U\eta^+_{j+\frac{1}{2}}\right)\\
+ \frac{1}{2}\left(H\mu_{j+1/2} + U\eta^-_{j+\frac{1}{2}} + H\mu_{j+1/2} + U\eta^+_{j+\frac{1}{2}}\right)\\
+ \frac{U^2 - gH}{2\sqrt{gH}}\left(\eta^+_{j+\frac{1}{2}} - \eta^-_{j+\frac{1}{2}}\right).
\end{aligned}$$

Using the reconstruction factors (4.7) and (4.8) and rearranging we get

$$F^\eta_{j+\frac{1}{2}} = \mathcal{F}^{\eta,\eta}_{j+\frac{1}{2}}\overline{\eta}_j + \mathcal{F}^{\eta,G}_{j+\frac{1}{2}}\overline{G}_j + \mathcal{F}^{\eta,c}_{j+\frac{1}{2}}$$

where

$$\begin{aligned}
\mathcal{F}^{\eta,\eta}_{j+\frac{1}{2}} &= H\mathcal{G}^\eta + \frac{U}{2}\left[\mathcal{R}^-_{j+1/2} + \mathcal{R}^+_{j+1/2}\right] - \frac{\sqrt{gH}}{2}\left[\mathcal{R}^+_{j+1/2} - \mathcal{R}^-_{j+1/2}\right]\\
\mathcal{F}^{\eta,G}_{j+\frac{1}{2}} &= H\mathcal{G}^G\\
\mathcal{F}^{\eta,c}_{j+\frac{1}{2}} &= H\mathcal{G}^c
\end{aligned}$$

For the flux function of G (4.4b) the flux approximation (4.11) becomes

$$\begin{aligned}F^G_{j+\frac{1}{2}} = &\frac{U}{2\sqrt{gH}}\left(UG^-_{j+\frac{1}{2}} + UH\mu_{j+1/2} + gH\eta^-_{j+\frac{1}{2}} - UG^+_{j+\frac{1}{2}} - UH\mu_{j+1/2} - gH\eta^+_{j+\frac{1}{2}}\right)\\ &+\frac{1}{2}\left(UG^-_{j+\frac{1}{2}} + UH\mu_{j+1/2} + gH\eta^-_{j+\frac{1}{2}} + UG^+_{j+\frac{1}{2}} + UH\mu_{j+1/2} + gH\eta^+_{j+\frac{1}{2}}\right)\\ &+\frac{U^2-gH}{2\sqrt{gH}}\left(G^+_{j+\frac{1}{2}} - G^-_{j+\frac{1}{2}}\right).\end{aligned}$$

By using the reconstruction factors (4.7) and (4.8) we get

$$F^G_{j+\frac{1}{2}} = \mathcal{F}^{G,\eta}_{j+\frac{1}{2}}\overline{\eta}_j + \mathcal{F}^{G,G}_{j+\frac{1}{2}}\overline{G}_j + \mathcal{F}^{G,c}_{j+\frac{1}{2}}$$

where

$$\begin{aligned}\mathcal{F}^{G,\eta}_{j+\frac{1}{2}} &= \frac{U\sqrt{gH}}{2}\left[\mathcal{R}^-_{j+1/2} - \mathcal{R}^+_{j+1/2}\right] + UH\mathcal{G}^\eta + \frac{gH}{2}\left[\mathcal{R}^-_{j+1/2} + \mathcal{R}^+_{j+1/2}\right],\\ \mathcal{F}^{G,G}_{j+\frac{1}{2}} &= UH\mathcal{G}^G + +\frac{U}{2}\left[\mathcal{R}^-_{j+1/2} + \mathcal{R}^+_{j+1/2}\right] - \frac{\sqrt{gH}}{2}\left[\mathcal{R}^+_{j+1/2} - \mathcal{R}^-_{j+1/2}\right],\\ \mathcal{F}^{G,c}_{j+\frac{1}{2}} &= UH\mathcal{G}^c.\end{aligned}$$

Right Supercritical Flow $Fr > 1$**:**

When the flow is flowing to the right and supercritical we have $Fr > 1$, which means that $a^-_{j+1/2} = 0$ and $a^+_{j+1/2} = U + \sqrt{gH}$. This is very similar to the left supercritical case, except instead of $\mathcal{R}^+_{j+1/2}$ we have $\mathcal{R}^-_{j+1/2}$ in our flux approximation for a general quantity (3.12) which reduces to

$$F_{j+\frac{1}{2}} = f\left(q^-_{j+\frac{1}{2}}\right).$$

Substituting in the flux function into (4.4a) and (4.4b) we obtain

$$F^\eta_{j+\frac{1}{2}} = \mathcal{F}^{\eta,\eta}_{j+\frac{1}{2}}\overline{\eta}_j + \mathcal{F}^{\eta,G}_{j+\frac{1}{2}}\overline{G}_j + \mathcal{F}^{\eta,c}_{j+\frac{1}{2}}$$

where

$$\begin{aligned}\mathcal{F}^{\eta,\eta}_{j+\frac{1}{2}} &= H\mathcal{G}^\eta + U\mathcal{R}^-_{j+1/2},\\ \mathcal{F}^{\eta,G}_{j+\frac{1}{2}} &= H\mathcal{G}^G,\\ \mathcal{F}^{\eta,c}_{j+\frac{1}{2}} &= H\mathcal{G}^c\end{aligned}$$

and

$$F^G_{j+\frac{1}{2}} = \mathcal{F}^{G,\eta}_{j+\frac{1}{2}}\overline{\eta}_j + \mathcal{F}^{G,G}_{j+\frac{1}{2}}\overline{G}_j + \mathcal{F}^{G,c}_{j+\frac{1}{2}}$$

where

$$\begin{aligned}\mathcal{F}^{G,\eta}_{j+\frac{1}{2}} &= UH\mathcal{G}^{\eta} + gH\mathcal{R}^{-}_{j+1/2},\\ \mathcal{F}^{G,G}_{j+\frac{1}{2}} &= U\mathcal{R}^{+}_{j+1/2} + UH\mathcal{G}^{G},\\ \mathcal{F}^{G,c}_{j+\frac{1}{2}} &= UH\mathcal{G}^{c}\end{aligned}$$

respectively.

4.2.4 Update Cell Averages

We have obtained the operators for the flux functions for supercrticial, critical and subcritical flow. Substituting the appropriate flux approximation into the forward Euler step, (3.20) we get

$$\begin{aligned}\overline{\eta}_j^{n+1} &= \overline{\eta}_j^{n} - \frac{\Delta t}{\Delta x}\left(\left[\mathcal{F}^{\eta,\eta}_{j+\frac{1}{2}}\overline{\eta}_j + \mathcal{F}^{\eta,G}_{j+\frac{1}{2}}\overline{G}_j + \mathcal{F}^{\eta,c}_{j+\frac{1}{2}}\right] - \left[\mathcal{F}^{\eta,\eta}_{j-\frac{1}{2}}\overline{\eta}_j + \mathcal{F}^{\eta,G}_{j-\frac{1}{2}}\overline{G}_j + \mathcal{F}^{\eta,c}_{j-\frac{1}{2}}\right]\right),\\ \overline{G}_j^{n+1} &= \overline{G}_j^{n} - \frac{\Delta t}{\Delta x}\left(\left[\mathcal{F}^{G,\eta}_{j+\frac{1}{2}}\overline{\eta}_j + \mathcal{F}^{G,G}_{j+\frac{1}{2}}\overline{G}_j + \mathcal{F}^{G,c}_{j+\frac{1}{2}}\right] - \left[\mathcal{F}^{G,\eta}_{j-\frac{1}{2}}\overline{\eta}_j + \mathcal{F}^{G,G}_{j-\frac{1}{2}}\overline{G}_j + \mathcal{F}^{G,c}_{j-\frac{1}{2}}\right]\right).\end{aligned}$$

Since $\mathcal{F}^{\eta,\eta}_{j-\frac{1}{2}} = e^{-ik\Delta x}\mathcal{F}^{\eta,\eta}_{j+\frac{1}{2}}$, $\mathcal{F}^{\eta,G}_{j-\frac{1}{2}} = e^{-ik\Delta x}\mathcal{F}^{\eta,G}_{j+\frac{1}{2}}$, $\mathcal{F}^{G,\eta}_{j-\frac{1}{2}} = e^{-ik\Delta x}\mathcal{F}^{G,\eta}_{j+\frac{1}{2}}$ and $\mathcal{F}^{G,G}_{j-\frac{1}{2}} = e^{-ik\Delta x}\mathcal{F}^{G,G}_{j+\frac{1}{2}}$ we have

$$\begin{aligned}\overline{\eta}_j^{n+1} &= \overline{\eta}_j^{n} - \frac{\Delta t}{\Delta x}\left(\left[1-e^{-ik\Delta x}\right]\left[\mathcal{F}^{\eta,\eta}_{j+\frac{1}{2}}\overline{\eta}_j + \mathcal{F}^{\eta,G}_{j+\frac{1}{2}}\overline{G}_j\right]\right),\\ \overline{G}_j^{n+1} &= \overline{G}_j^{n} - \frac{\Delta t}{\Delta x}\left(\left[1-e^{-ik\Delta x}\right]\left[\mathcal{F}^{G,\eta}_{j+\frac{1}{2}}\overline{\eta}_j + \mathcal{F}^{G,G}_{j+\frac{1}{2}}\overline{G}_j\right]\right).\end{aligned}$$

This can be written in matrix form using the identity matrix $\mathbf{I}$ as

$$\begin{aligned}\begin{bmatrix}\overline{\eta}\\ \overline{G}\end{bmatrix}_j^{n+1} &= \begin{bmatrix}\overline{\eta}\\ \overline{G}\end{bmatrix}_j^{n} - \left(1-e^{-ik\Delta x}\right)\frac{\Delta t}{\Delta x}\begin{bmatrix}\mathcal{F}^{\eta,\eta} & \mathcal{F}^{\eta,G}\\ \mathcal{F}^{G,\eta} & \mathcal{F}^{G,G}\end{bmatrix}\begin{bmatrix}\overline{\eta}\\ \overline{G}\end{bmatrix}_j^{n}\\ &= \left(\mathbf{I} - \Delta t\mathbf{F}\right)\begin{bmatrix}\overline{\eta}\\ \overline{G}\end{bmatrix}_j^{n}\end{aligned} \tag{4.12}$$

for a single Euler step which is first-order in time.

4.2.5 Second-Order SSP Runge-Kutta Method

To achieve second-order accurate time stepping, the second-order SSP Runge-Kutta scheme (3.21) is used. This scheme uses the following convex combination

of the Euler steps (4.12)

$$\begin{bmatrix}\overline{\eta}\\ \overline{G}\end{bmatrix}_j^{(1)} = (\mathbf{I} - \Delta t\mathbf{F}) \begin{bmatrix}\overline{\eta}\\ \overline{G}\end{bmatrix}_j^{n}, \tag{4.13a}$$

$$\begin{bmatrix}\overline{\eta}\\ \overline{G}\end{bmatrix}_j^{(2)} = (\mathbf{I} - \Delta t\mathbf{F}) \begin{bmatrix}\overline{\eta}\\ \overline{G}\end{bmatrix}_j^{(1)}, \tag{4.13b}$$

$$\begin{bmatrix}\overline{\eta}\\ \overline{G}\end{bmatrix}_j^{n+1} = \frac{1}{2}\left(\begin{bmatrix}\overline{\eta}\\ \overline{G}\end{bmatrix}_j^{n} + \begin{bmatrix}\overline{\eta}\\ \overline{G}\end{bmatrix}_j^{(2)} \right). \tag{4.13c}$$

Substituting (4.13a) and (4.13b) into (4.13c) we can write this in terms of the flux matrix $\mathbf{F}$ and our cell averages at t^n as

$$\begin{bmatrix}\overline{\eta}\\ \overline{G}\end{bmatrix}_j^{n+1} = \frac{1}{2}\left(\begin{bmatrix}\overline{\eta}\\ \overline{G}\end{bmatrix}_j^{n} + (\mathbf{I} - \Delta t\mathbf{F})^2 \begin{bmatrix}\overline{\eta}\\ \overline{G}\end{bmatrix}_j^{n} \right).$$

Expanding $(\mathbf{I} - \Delta t\mathbf{F})^2$ we get

$$\begin{aligned}\begin{bmatrix}\overline{\eta}\\ \overline{G}\end{bmatrix}_j^{n+1} &= \left(\mathbf{I} - \Delta t\mathbf{F} + \frac{1}{2}\Delta t^2\mathbf{F}^2\right) \begin{bmatrix}\overline{\eta}\\ \overline{G}\end{bmatrix}_j^{n} \\ &= \mathbf{E} \begin{bmatrix}\overline{\eta}\\ \overline{G}\end{bmatrix}_j^{n}\end{aligned} \tag{4.14}$$

which is in the desired form (4.1).

This is the evolution matrix $\mathbf{E}$ for FEVM_2. The matrix $\mathbf{E}$ is dependent on the flux matrix $\mathbf{F}$ and therefore will depend on the Froude number. The Froude number is constant over time in this analysis and so we can investigate supercritical, subcritical and critical flow individually.

The convergence and dispersion analysis then proceed by studying the properties of the evolution matrix $\mathbf{E}$ for FEVM_2. As a comparison we also provide the results for the finite difference volume methods FDVM_1, FDVM_2 and FDVM_3 described by Zoppou et al. [15] and the finite difference methods $\mathcal{D}$ and $\mathcal{W}$ described by Pitt et al. [14].

The evolution matrices for FDVM_1, FDVM_2, FDVM_3 can be derived following the derivation of the evolution matrix of FEVM_2 using the expressions for its constituent operators provided in Appendix C. For $\mathcal{D}$ and $\mathcal{W}$ the evolution matrices are (C.6) and (C.7) respectively. We now present the results of the convergence analysis.

4.3 Convergence Analysis

We apply the Lax-equivalence theorem to demonstrate the convergence of our numerical methods by establishing their consistency and stability. We use a Von Neumann stability analysis to demonstrate stability. Consistency is demonstrated for the Fourier modes (4.5) solutions which form a basis of the solution space of the linearised Serre equations. Together these stability and consistency conditions imply convergence of the numerical method under the L_2 norm.

4.3.1 Stability

For a numerical method to be stable we must ensure that errors from previous time steps are not amplified over the current time step. To accomplish this we must ensure

$$\rho\left(\mathbf{E}\right) \leq 1 \tag{4.15}$$

where $\rho\left(\mathbf{E}\right)$ is the spectral radius of $\mathbf{E}$. Since $\mathbf{E}$ was derived for our methods by using Fourier modes, this condition implies Von Neumann stability.

We calculated $\rho\left(\mathbf{E}\right)$ numerically for various values of Δx, Δt, k, H and U to check if (4.15) holds. We summarised our results in Figure 4.1 which is a plot of $\rho\left(\mathbf{E}\right)$ against $\Delta x/\lambda$ for representative values of k, H and U; where $\lambda = 2\pi/k$ is the wavelength. We used g $= 9.81 m/s^2$ and chose $\Delta t = 0.5/\left(U + \sqrt{gH}\right)\Delta x$ to satisfy the CFL condition (3.22). This is the common choice of Δt in our numerical experiments.

The behaviour of $\rho\left(\mathbf{E}\right)$ for $H = 1m$, $k = \frac{\pi}{10} m^{-1}$ and $U = 0m/s$ and $1m/s$ is shown in Figure 4.1 and is representative of the behaviour for all other values of H, k and U. For these k and H values the shallowness parameter $\sigma = \frac{1}{20}$ and so the Serre equations are applicable [21].

In Figure 4.1 it can be seen that all methods have $\rho\left(\mathbf{E}\right) \leq 1$ for $U = 0m/s$ and are therefore stable. The two finite difference methods overlap and have $\rho\left(\mathbf{E}\right) = 1$ for all Δx values, while the FDVM_2 and the FEVM_2 also overlap with $\rho\left(\mathbf{E}\right) < 1$. However, when $U \neq 0m/s$ the method $\mathcal{W}$ has $\rho\left(\mathbf{E}\right) > 1$ for all Δx values and is therefore unstable. All other methods have $\rho\left(\mathbf{E}\right) \leq 1$, retaining their stability when $U \neq 0m/s$.

We observed the same results for a wide range of k, H and U values and Froude numbers. All methods except $\mathcal{W}$ were found to be stable for any combination of these variables. While $\mathcal{W}$ was only stable when $U = 0m/s$. This is different from the stability result for $\mathcal{D}$ and $\mathcal{W}$ reported by [14] as that analysis assumed

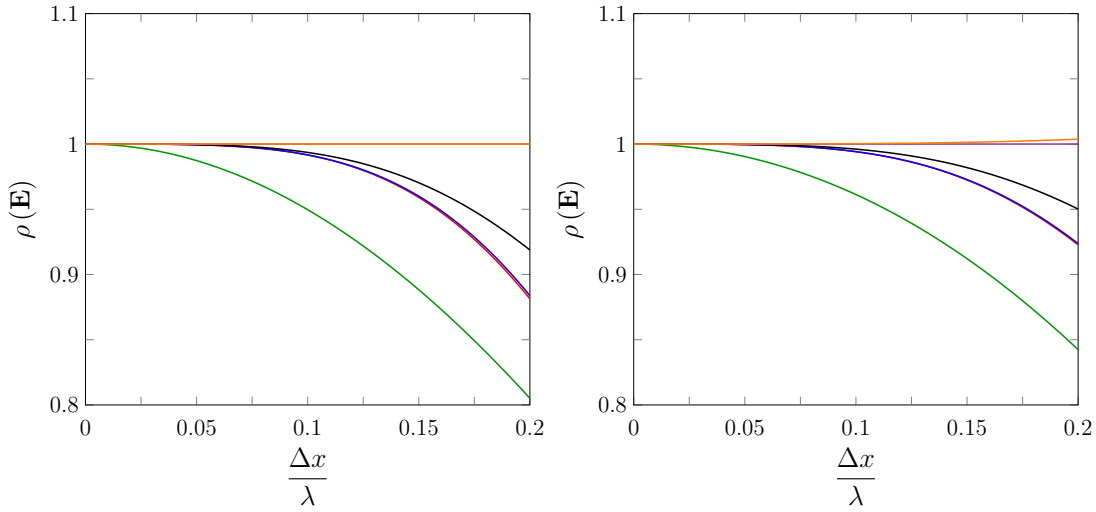

(a) $U = 0$ (b) $U = 1$

Figure 4.1: Spectral radius of $\mathbf{E}$ against $\Delta x/\lambda$ for FDVM_1 (–), FDVM_2 (–), FEVM_2 (–), FDVM_3 (–), $\mathcal{D}$ (–) and $\mathcal{W}$ (–). With $H = 1m$ and $k = \frac{\pi}{10}$.

$U = 0n/s$.

4.3.2 Consistency

For a numerical method to be consistent the error introduced by the method for a single time step must approach zero as the spatial and temporal resolution is increased. To demonstrate convergence, it is enough to demonstrate consistency for the eigenfunctions of the linearised Serre equations, which are the Fourier modes. Therefore, we can demonstrate consistency by investigating the evolution matrix $\mathbf{E}$. The error introduced for a single time step from t^n to t^{n+1}, $\mathcal{T}^n$ is

$$\mathcal{T}^n = \mathbf{E}\left[\frac{\overline{\eta}}{\overline{G}}\right]_j^n - \left[\frac{\overline{\eta}}{\overline{G}}\right]_j^{n+1}. \tag{4.16}$$

To ensure consistency we must have that $\lim_{\Delta x,\Delta t\to 0}\|\mathcal{T}^n\|_2 = 0$ for all n, where $\|\cdot\|_2$ is the L_2 vector norm. Taking the L_2 norm of both sides of (4.16) and using (4.6) we obtain

$$\|\mathcal{T}^n\|_2 = \left\|\mathbf{E}\left[\frac{\overline{\eta}}{\overline{G}}\right]_j^n - e^{i\omega^{\pm}\Delta t}\left[\frac{\overline{\eta}}{\overline{G}}\right]_j^n\right\|_2.$$

Using the matrix norm induced by L_2, the Frobenius norm $\|\cdot\|_F$ we have that

$$\|\mathcal{T}^n\|_2 \leq \left\|\mathbf{E} - e^{i\omega^{\pm}\Delta t}\mathbf{I}\right\|_F \left\| \left[\frac{\overline{\eta}}{\overline{G}}\right]_j^n \right\|_2 .$$

Since $\overline{\eta}_j^n$ and $\overline{G}_j^n$ are finite and independent of Δx and Δt, if $\lim_{\Delta x,\Delta t\to 0}\left\|\mathbf{E} - e^{i\omega^{\pm}\Delta t}\mathbf{I}\right\|_F = 0$ then $\lim_{\Delta x,\Delta t\to 0}\|\mathcal{T}^n\|_2 = 0$ as desired.

We calculated the Taylor series of $\mathbf{E} - e^{i\omega^{\pm}\Delta t}\mathbf{I}$ for all the numerical methods for all flow scenarios; subcritical, critical and supercritical flows. Since the results are the same for ω^+ and ω^- we only report the results for ω^+. For FEVM$_2$ the lowest order Δx and Δt terms of the Taylor series of $\mathbf{E} - e^{i\omega^{+}\Delta t}\mathbf{I}$ can be found in Table 4.1. From this table it can be seen that the Taylor series of all the elements of $\mathbf{E} - e^{i\omega^{+}\Delta t}\mathbf{I}$ have a factor of Δt. So that

$$\begin{aligned}\left\|\mathbf{E} - e^{i\omega^{+}\Delta t}\mathbf{I}\right\|_F &= \|\Delta t\left(\mathbf{M}_0 + \mathcal{O}\left(\Delta t\right)\right)\|_F \\ &= |\Delta t|\,\|\mathbf{M}_0 + \mathcal{O}\left(\Delta t\right)\|_F \\ &\leq |\Delta t|\left(\|\mathbf{M}_0\|_F + \|\mathcal{O}\left(\Delta t\right)\|_F\right)\end{aligned}$$

where $\mathbf{M}_0$ is some matrix.

From Tables 4.1 we have that $\mathbf{M}_0$ is independent of Δt and finite so that as $\Delta t \to 0$ then $|\Delta t|\left(\|\mathbf{M}_0\|_F + \|\mathcal{O}\left(\Delta t\right)\|_F\right) \to 0$ and therefore $\left\|\mathbf{E} - e^{i\omega^{+}\Delta t}\mathbf{I}\right\|_F \to 0$. Therefore, for FEVM$_2$ we have $\lim_{\Delta x,\Delta t\to 0}\|\mathcal{T}^n\|_2 = 0$ and so FEVM$_2$ is consistent for Fourier mode solutions implying consistency for all solutions as desired.

All methods were found to be consistent using the same reasoning. Their Tables can be found in Appendix C. In particular we have Tables C.9 and C.10 for FDVM$_1$, Table C.11 for FDVM$_2$, Tables C.12 and C.13 for FDVM$_3$, Table C.14 for $\mathcal{D}$ and Table C.15 for $\mathcal{W}$.

4.4 Dispersion Analysis

To study the dispersion properties of the numerical method, we must calculate the dispersion relation of the numerical method that relates the frequency $\widetilde{\omega}^{\pm}$ to the wavenumber k. Making use of (4.6) in (4.14) we get

$$\mathbf{E}\left[\frac{\overline{\eta}}{\overline{G}}\right]_j^n = e^{i\omega^{\pm}\Delta t}\left[\frac{\overline{\eta}}{\overline{G}}\right]_j^n . \tag{4.17}$$

Element	Lowest Order Terms of Error for FEVM_2	
	Δx	Δt
$E_{0,0} - e^{i\omega^+\Delta t}$	$-\dfrac{i\left(54+45H^2k^2+10H^4k^4\right)}{120\beta^2}Uk^3\Delta t\Delta x^2$	$\dfrac{\sqrt{3gH\beta}+3U}{\beta}ik\Delta t$
$E_{0,1}$	$\dfrac{\beta-3}{\beta^2}\dfrac{ik^3}{40}\Delta t\Delta x^2$	$-\dfrac{3}{\beta}ik\Delta t$
$E_{1,0}$	$-\left(gH-\dfrac{15U^2}{\beta}+\dfrac{9U^2}{\beta}\right)\dfrac{k^3}{120}\Delta t\Delta x^2$	$\left(-gH+\dfrac{3U^2}{\beta}\right)ik\Delta t$
$E_{1,1} - e^{i\omega^+\Delta t}$	$\dfrac{126+75H^2k^2+10H^4k^4}{\beta^2}\dfrac{k^3}{120}iU\Delta t\Delta x^2$	$\dfrac{\sqrt{3gH\beta}-3U}{\beta}ik\Delta t$

Table 4.1: Lowest order terms of the Taylor series for the elements of $\mathbf{E}-e^{i\omega^+\Delta t}\mathbf{I}$ for FEVM_2 for all values of Fr. Here $\beta = 3+k^2H^2$.

Therefore, the evolution matrix $\mathbf{E}$ of an exact method has the eigenvalues $e^{i\omega^+\Delta t}$ and $e^{i\omega^-\Delta t}$ where $\omega^\pm$ are the positive and negative branches of the dispersion relation of the linearised Serre equations (2.9). For approximate numerical methods the dispersion relation for $\widetilde{\omega}^\pm$ can be calculated by taking the eigenvalues of its evolution matrix $\lambda^\pm$ like so

$$\widetilde{\omega}^\pm = \frac{1}{i\Delta t}\log\left[\lambda^\pm\right].$$

By comparing $\widetilde{\omega}^\pm$ with the analytic $\omega^\pm$ given by the linearised Serre equations (2.9) we can determine the error in the dispersion relation for the numerical method. The real part of the frequency determines the speed of a wave, while the imaginary part determines the change in amplitude. For the linearised Serre equations the imaginary part of $\omega^\pm$ is zero and so the amplitude of waves are constant in time. We only present the results for the positive branch of the dispersion relation comparing $\widetilde{\omega}^+$ and ω^+ as the behaviour of the negative branch is very similar.

The relative error in the dispersion relation was plotted against $\Delta x/\lambda$ for representative values of H, U and k. Where $\lambda = 2\pi/k$ is the wavelength of the wave with wave number k. We used $g = 9.81m/s^2$ and chose $\Delta t = 0.5/\left(U + \sqrt{gH}\right)\Delta x$ to satisfy the CFL condition (3.22).

In Figures 4.2 and 4.3 we present the plots for $kH = \pi/10$ where $\sigma = kH/2\pi = 1/20$ and so the water is shallow and thus the Serre equations are appropriate. We present the real and imaginary errors separately to isolate the errors in the speed and amplitude of the wave for the numerical method. The total error is also reported as a measure of the overall error in the dispersion relation of the numerical method.

From Figures 4.2 and 4.3 we can see that all methods approximate the dispersion relation of the Serre equations well with the approximation improving as $\Delta x \to 0$, as expected.

For the real part of the dispersion error all the FEVM and the FDVM outperform the two finite difference methods and therefore will better approximate the speed of waves of the linearised Serre equations. However, for the amplitude of waves the roles are reversed with the two finite difference methods either scaling the waves very little or not at all. When taking both effects into account with the total error we see that the FDVM_1 has the largest dispersion error followed by $\mathcal{W}$, $\mathcal{D}$, FEVM_2, FDVM_2 and finally FDVM_3 has the lowest dispersion error. So that the size of the total dispersion error is mainly determined by the order

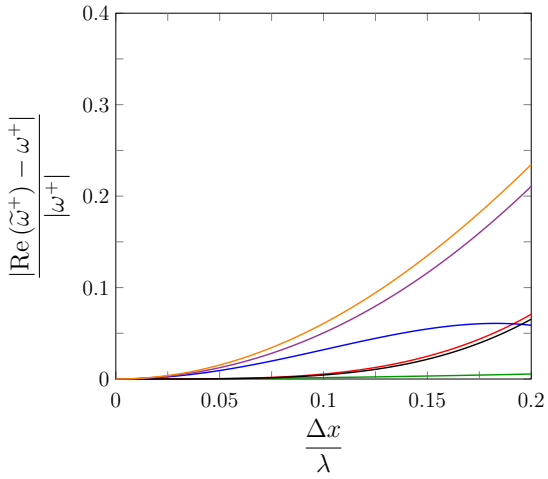

(a) Real Part

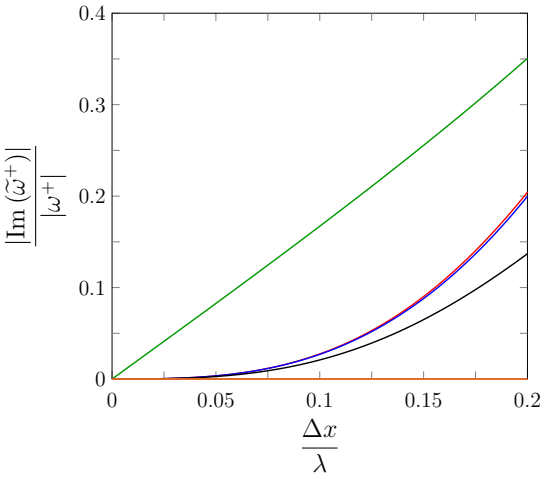

(b) Imaginary Part

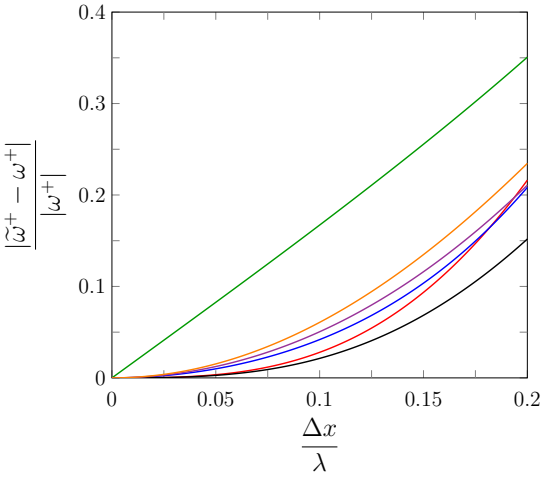

(c) Real and Imaginary Parts

Figure 4.2: Relative dispersion error against $\Delta x/\lambda$ when $H = 1m$, $k = \frac{\pi}{10}$ and $U = 0m/s$ for FDVM$_1$ (–), FDVM$_2$ (–), FEVM$_2$ (–), FDVM$_3$ (–), $\mathcal{D}$ (–) and $\mathcal{W}$ (–).

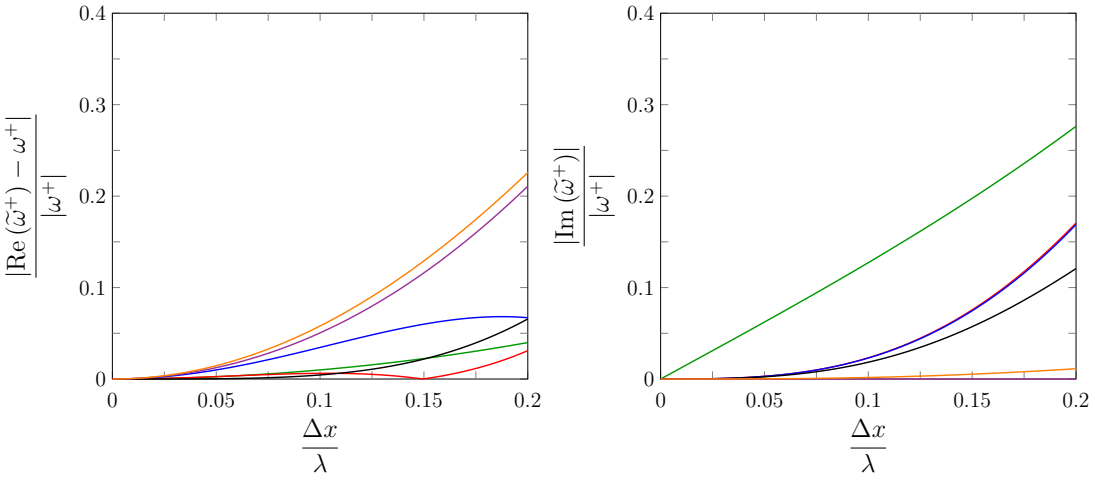

(a) Real part

(b) Imaginary part

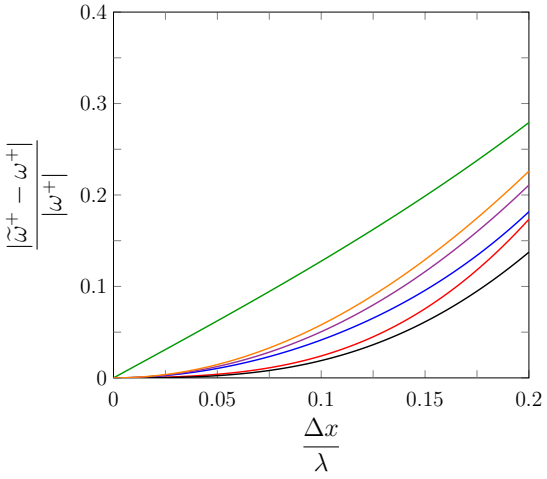

(c) Real and Imaginary Parts

Figure 4.3: Relative dispersion error against $\Delta x/\lambda$ when $H = 1m$, $k = \frac{\pi}{10}$ and $U = 1m/s$ for FDVM_1 (–), FDVM_2 (–), FEVM_2 (–), FDVM_3 (–), $\mathcal{D}$ (–) and $\mathcal{W}$ (–).

of accuracy of the numerical scheme. Overall the methods built around a FVM perform better than the finite difference methods of the same order.

Figures 4.2 and 4.3 furthermore demonstrate that FDVM_2 is superior to FEVM_2 not just for the complete dispersion error, but its real and imaginary parts individually as well. Therefore, FDVM_2 should more accurately model the speed and amplitude of waves.

We observed similar results across a wide array of k, H and U values. However, as kH is increased the distinction between FDVM_2 and FEVM_2 becomes less pronounced. This can be seen in Figure 4.4 where $kH = 2.5$ and $\sigma = 5/4\pi > 1/20$ where the water is no longer shallow.

These kH values are the same as those reported by Filippini et al. [37], and our results are similar for the real part of the dispersion error. Our FDVM and the FEVM compare favourably with the methods described and analysed by Filippini et al. [37]. Furthermore, we extended their work by allowing for non-zero values of U, combining the spatial and temporal approximations and examining the imaginary and total error in the dispersion relation. This work also extended the dispersion analysis presented by Zoppou et al. [15] for FDVM_1, FDVM_2 and FDVM_3 by including non-zero values of U.

Figure 4.5 demonstrates that the results of the real part of the dispersion error is slightly different if we allow for non-zero values of U. For example the non-zero value of U significantly changes the real part of the dispersion error for FDVM_1 when $kH = 2.5$. Therefore, for some methods allowing for non-zero values of U can have a significant impact on the conclusions drawn from the dispersion analysis. Furthermore, taking the imaginary part of the dispersion error into account is important as $\omega^{\pm}$ determines not only the speed of waves but also their amplitude. For instance the FDVM_1 performs very well for the real part of the dispersion error and poorly for the imaginary part, and so false conclusions about the accuracy of the method could be drawn from only considering the real part of the dispersion error.

The Taylor series expansion of $\widetilde{\omega}^{\pm}$ was also derived for all the numerical methods. We have compiled the lowest order terms of the Taylor series for $\widetilde{\omega}^{+} - \omega^{+}$ in Table 4.2 when $-1 \leq Fr \leq 1$ for the FDVM and FEVM. In Table 4.2 it is clear that these schemes estimated ω^{+} with the expected order of accuracy in both space and time. This was also the case for ω^{-}.

We also present the lowest order terms of the Taylor series for $\widetilde{\omega}^{+} - \omega^{+}$ for both $Fr < -1$ and $Fr > 1$ in Table 4.3. We only present the errors that are different from those reported in Table 4.2, this was only the case for the

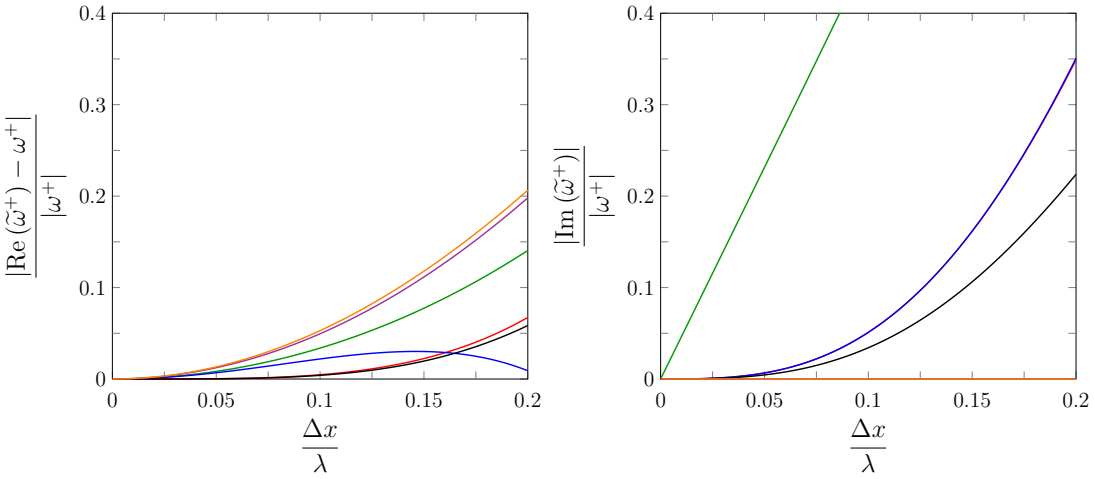

(a) Real part

(b) Imaginary part

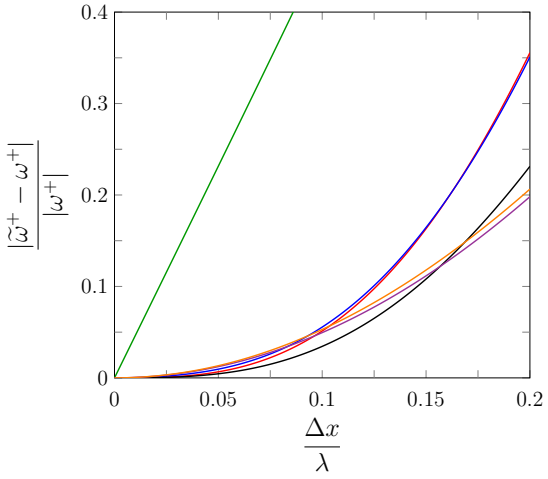

(c) Real and Imaginary Parts

Figure 4.4: Relative dispersion error against $\Delta x/\lambda$ when $H = 1m$, $k = 2.5$ and $U = 0m/s$ for FDVM_1 (–), FDVM_2 (–), FEVM_2 (–), FDVM_3 (–), $\mathcal{D}$ (–) and $\mathcal{W}$ (–).

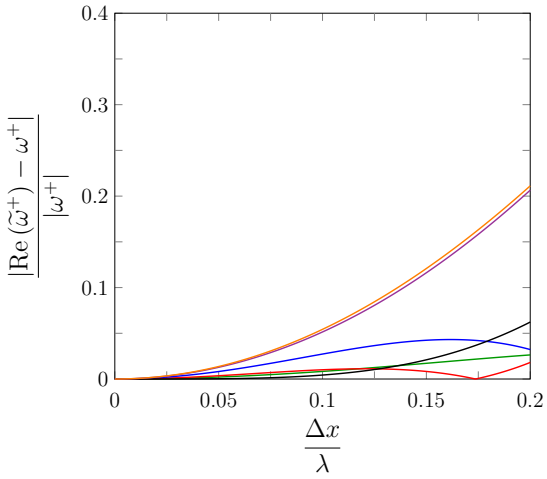

(a) Real part

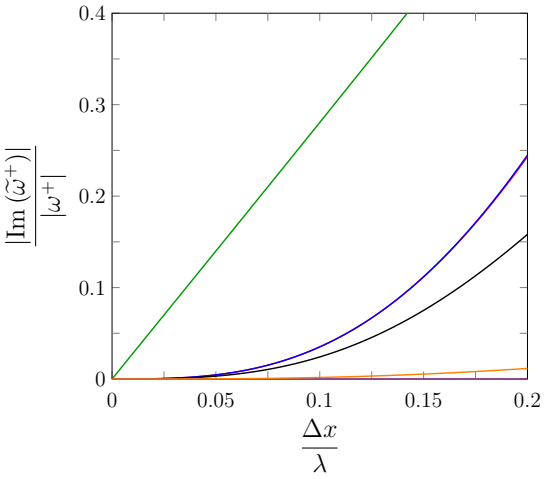

(b) Imaginary part

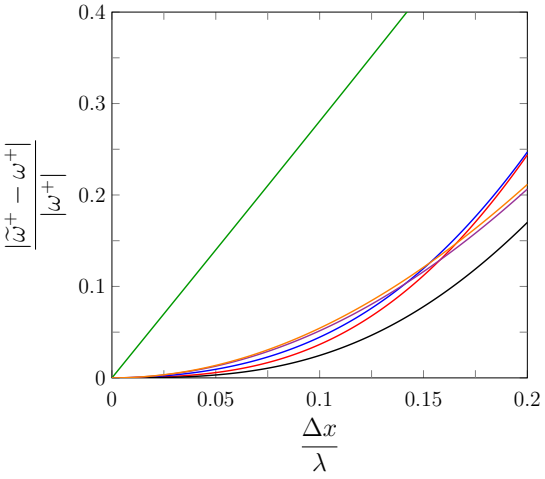

(c) Real and Imaginary Parts

Figure 4.5: Relative dispersion error against $\Delta x/\lambda$ when $H = 1m$, $k = 2.5$ and $U = 1m/s$ for FDVM_1 (–), FDVM_2 (–), FEVM_2 (–), FEVM_3 (–), $\mathcal{D}$ (–) and $\mathcal{W}$ (–).

Scheme	Lowest Order Terms of $\widetilde{\omega}^+ - \omega^+$	
	Δx	Δt
FDVM_1	$-\left(2\sqrt{gH} - \sqrt{\frac{3U}{\beta}}\right)\frac{ik^2}{4}\Delta x$	$\frac{i\left(\omega^+\right)^2}{2}\Delta t$
FDVM_2	$\frac{2\beta U - 3\sqrt{3gH\beta}}{\beta^2}\frac{k^3}{24}\Delta x^2$	$-\frac{\left(\omega^+\right)^3}{6}\Delta t^2$
FEVM_2	$\left(U + \frac{(42 + 15k^2H^2)\sqrt{3gH\beta}}{20\beta^2}\right)\frac{k^3}{12}\Delta x^2$	$-\frac{\left(\omega^+\right)^3}{6}\Delta t^2$
FDVM_3	$-\left(2\sqrt{gH} - \sqrt{3\beta}U\right)\frac{ik^4}{24}\Delta x^3$	$-\frac{i\left(\omega^+\right)^4}{24}\Delta t^3$

Table 4.2: Lowest order terms for Taylor series of $\widetilde{\omega}^+ - \omega^+$ for all FDVM and the FEVM. With $-1 \leq Fr \leq 1$ and $\beta = 3 + H^2k^2$.

spatial error of the first- and third–order numerical methods. From these tables it is clear that the FDVM and the FEVM retain their order of accuracy when approximating ω^+ for when the flow is supercritical, this was also the case for ω^-.

Finally we present the lowest order terms of the Taylor series for $\widetilde{\omega}^+ - \omega^+$ for the finite difference methods in Table 4.4. These methods do not change depending on the value of the physical quantities. The two finite difference methods retain their order of accuracy in space and time when approximating ω^+.

Because all methods were demonstrated to have the expected order of accuracy in approximating $\omega^\pm$ for the linearised Serre equations this implies that for small Δx values the order of accuracy will be the primary driver of the dispersion error, as was observed.

In this chapter the convergence and dispersion properties of the numerical methods were studied using a linear analysis. The results of this analysis demonstrated the superiority of the higher-order accurate FDVM and FEVM over the finite difference methods.

Scheme	Lowest Order Δx Term of $\widetilde{\omega}^+ - \omega^+$	
	$Fr < -1$	$Fr > 1$
FDVM$_1$	$-\left(2U + \sqrt{\frac{3gH}{\beta}}\right)\frac{ik^2}{4}\Delta x$	$\left(2U + \sqrt{\frac{3gH}{\beta}}\right)\frac{ik^2}{4}\Delta x$
FDVM$_3$	$-\left(2U + \sqrt{\frac{3gH}{\beta}}\right)\frac{ik^4}{24}\Delta x^3$	$\left(2U + \sqrt{\frac{3gH}{\beta}}\right)\frac{ik^4}{24}\Delta x^3$

Table 4.3: Lowest order Δx term for Taylor series of $\widetilde{\omega}^+ - \omega^+$ for all FDVM for supercritical Froude numbers where different from Table 4.2. With $\beta = 3 + H^2k^2$.

Scheme	Lowest Order Terms of $\widetilde{\omega}^+ - \omega^+$	
	Δx	Δt
$\mathcal{D}$	$-\chi\Delta x^2$	$-\frac{(\omega^+)^3}{3}\Delta t^2$
$\mathcal{W}$	$\chi\Delta x^2$	$\frac{1}{\beta^2}\Big(\beta U^2\left[9\sqrt{3gH\beta} + 4\beta U\right]$ $+3gH^2\left[\sqrt{3gH\beta} + 6\beta U\right]\Big)\frac{k^3}{18}\Delta t^2$

Table 4.4: Lowest order terms of the Taylor series of $\widetilde{\omega}^+ - \omega^+$ for $\mathcal{D}$ and $\mathcal{W}$. With $\beta = 3 + H^2k^2$ and $\chi = \left(U + \frac{(4 + H^2k^2)\sqrt{3gH\beta}}{4\beta^2}\right)$.

Chapter 5

Numerical Validation

In this chapter analytic and forced solutions are used to validate the numerical methods.

To verify that the numerical methods have the expected convergence and conservation properties we make use of the analytic and forced solutions described in Chapter 2. To assess these properties we first introduce the measures of convergence and conservation for a numerical solution. These measures are then used to compare all the numerical methods using the solitary travelling wave solution. The convergence and conservation properties of FDVM_2 and FEVM_2 are compared using the lake at rest solution. Currently, the FDVM_2 and FEVM_2 are the only methods in this thesis that incorporate varying bathymetry.

Finally we validate FDVM_2 and FEVM_2 using forced solutions which test the accuracy of their approximations to all terms in the Serre equations. The forced solutions are obtained by adding terms to the Serre equations (2.13) to force any desired solution. This allows the method to be validated against more flow scenarios than possible given the limited number of currently known analytic solutions. These forced solutions can be any functions and so the forced Serre equations are no longer strictly conservative. Therefore, the forced solutions are only used to assess the convergence properties of these numerical methods.

5.1 Measuring Convergence and Conservation

The convergence of the numerical methods is studied by comparing their numerical solutions to the analytic solutions or the forced solutions of the Serre equations. While conservation is investigated by comparing the total amount of a conserved quantity in a numerical solution at some time with the total amount

of that quantity present in the initial conditions. We introduce notation for these measures and describe their calculation here, beginning with convergence.

5.1.1 Measure of Convergence

By measuring the relative difference between the numerical and analytic solutions as Δx varies, the convergence of the numerical methods can be investigated. To measure the relative difference we use the L_2 vector norm; to compare the numerical and analytic solutions at the cell midpoints x_j at the end of the simulations. For a quantity q, the vector of its values $\boldsymbol{q}$ at the cell midpoints x_j and the corresponding numerical solution at those locations $\boldsymbol{q^*}$; the L_2 norm is

$$L_2(\boldsymbol{q}, \boldsymbol{q^*}) = \begin{cases} \dfrac{||\boldsymbol{q^*} - \boldsymbol{q}||_2}{||\boldsymbol{q}||_2} & ||\boldsymbol{q}||_2 > 0 \\ \\ ||\boldsymbol{q^*}||_2 & ||\boldsymbol{q}||_2 = 0. \end{cases}$$

5.1.2 Measures of Conservation

The conservation properties of the methods are established by calculating the total amount of a conserved quantity in the numerical solution $\mathcal{C}^* (\boldsymbol{q^*})$ at the end of the simulation and comparing it to the total amount of that quantity present in the initial conditions $\mathcal{C} (q(x,0))$, derived analytically. Again a relative measure is used;

$$C(q, \boldsymbol{q^*}) = \begin{cases} \dfrac{|\mathcal{C}^* (\boldsymbol{q^*}) - \mathcal{C} (q(x,0)) |}{|\mathcal{C} (q(x,0)) |} & |\mathcal{C} (q(x,0)) | > 0 \\ \\ |\mathcal{C}^* (\boldsymbol{q^*}) | & |\mathcal{C} (q(x,0)) | = 0 \end{cases} \tag{5.1}$$

where $\mathcal{C}^* (\boldsymbol{q^*})$ was calculated using 3 point Gaussian quadrature over the j^{th} cell and summing these cell integrals for all j. The value of q at the three points needed to perform the Gaussian quadrature were calculated by interpolating the j^{th} cell using a quartic polynomial that fits the nodal values q_{j-2}, q_{j-1}, q_j, q_{j+1} and q_{j+2} at the surrounding cell midpoints. The Gaussian quadrature using three points is 5^{th} order accurate and interpolation by quartics is 5^{th} order accurate for the quantity q and 4^{th} order accurate for its spatial derivative $\partial q/\partial x$. Since all methods are third-order accurate or less, the error introduced by the calculation of $\mathcal{C}^* (\boldsymbol{q^*})$ for h, uh, G and $\mathcal{H}$ will be dominated by the error introduced by the numerical solvers.

In some cases $\mathcal{C}\left(q(x,0)\right)$ may be difficult to derive analytically. In this case we approximate $\mathcal{C}\left(q(x,0)\right)$ with $\mathcal{C}^*\left(\boldsymbol{q}^0\right)$ in (5.1); where $\boldsymbol{q}^0$ is the vector of the quantity at the cell midpoints used as the initial conditions of our numerical method. We denote the numerical approximation to the conservation error (5.1) by C^*.

5.2 Solitary Travelling Wave Solution

To assess the ability of our numerical methods to solve the Serre equations with a horizontal bed we use the solitary travelling wave solution (2.11) described in Chapter 2. This is a particular member of the family of periodic travelling wave solutions [29]. Every member of this family of solutions except the trivial stationary one have the same non-zero terms and thus provide similar tests for the numerical methods. Hence, it is sufficient to only study the solitary travelling wave solution.

For the solitary wave solution all the terms in (2.8) must be adequately approximated by the numerical method to properly reproduce the analytic solution. Therefore, this analytic solution serves as a benchmark for the ability of a numerical method to accurately solve the Serre equations with a horizontal bed for smooth solutions.

For our numerical tests we used the solitary travelling wave solution (2.11) with $a_0 = 1m$, $a_1 = 0.7m$ and $g = 9.81m/s^2$ at $t = 0s$ as the initial conditions. The spatial domain was $[-250m, 250m]$ and the problem was solved until $t = 50s$. This was done for a range of Δx values that had the following form; $\Delta x = 100/2^k m$ with $k \in [6, \ldots, 19]$. The CFL condition was satisfied with CFL number $Cr = 0.5$ by setting $\Delta t = Cr\Delta x/\sqrt{g\left(a_0 + a_1\right)}$. For FDVM_2 and FEVM_2 the limiting parameter $\theta = 1.2$ was used in the generalised minmod limiter (3.2) employed by both methods during the reconstruction step. While FDVM_3 used a Koren limiter in its reconstruction [15], which has no limiting parameter.

For the parameters $a_0 = 1m$ and $a_1 = 0.7m$ the non-linearity is $\epsilon = a_1/a_0 = 0.7$; this is large but beneath most of the well known breaking thresholds for water waves $\epsilon \leq 0.8$ [53]. Because ϵ is large the non-linear effects are large and therefore, so are the balancing dispersive effects making this particular analytic solution a rigorous test of the numerical methods. For this spatial domain and final time $t = 50s$ there is no interaction of the wave with the boundary, therefore the Dirichlet boundary conditions were appropriate.

The results of this analytic solution validation were published by Zoppou et al. [15] for FDVM_1, FDVM_2 and FDVM_3. I produced the results in that paper which have been expanded here to include an investigation of the convergence of G and the conservation of h, uh and G.

An example numerical solution with $\Delta x = 100/2^{11}m \approx 0.049m$ from all methods was plotted in Figure 5.1 against the analytic solution at $t = 50s$. We have only plotted an illustrative amount of the points in the numerical solution. From these plots it is clear that FDVM_1 performs significantly worse than the higher-order methods at reproducing the analytic solution, even for this relatively fine grid where the wave is captured by more than 200 cells. This is primarily due to the numerical diffusion introduced by the method, which has caused the wave in the numerical solution to decrease in amplitude and widen significantly. The higher-order numerical methods all accurately replicate the analytic solution, with insignificant visual differences in these plots due to the high resolution of the grid.

The L_2 error was calculated for h, u and G for all numerical solutions and was plotted against Δx for all numerical methods in Figure 5.2. From these plots it is clear that all numerical methods are convergent. The rate at which the numerical solutions converge to the analytic solution over Δx is determined by the order of accuracy of the numerical scheme. All methods demonstrate the expected order of accuracy given the order of accuracy of the approximations used in the method; which agrees with the results of the linear analysis in Chapter 4 and Appendix C.

All methods more accurately reproduced the analytic solution for h than either G or u across all Δx values. This is due to the simplicity of h's evolution equation (2.6a) compared to the evolution equation of G (2.6b); with the error in u being dominated by the error in G.

Increasing the order of accuracy of our numerical methods leads to smaller errors when comparing two numerical solutions for the same Δx value, as Figure 5.2 clearly demonstrates. This is consistent with the example numerical solution in Figure 5.1, where the lowest order accuracy scheme, FDVM_1 had the poorest reproduction of the analytic solution. However, there is only a slight benefit from moving from the second-order FEVM_2 and FDVM_2 to the third-order FDVM_3.

For the second-order methods we find that FDVM_2 consistently produces the smallest L_2 error followed by FEVM_2, $\mathcal{W}$ and $\mathcal{D}$. The difference between the FDVM_2 and FEVM_2 is significant with the errors of FEVM_2 being 2 to 4 times larger than those of FDVM_2. Therefore, FDVM_2 is reproducing the solitary wave

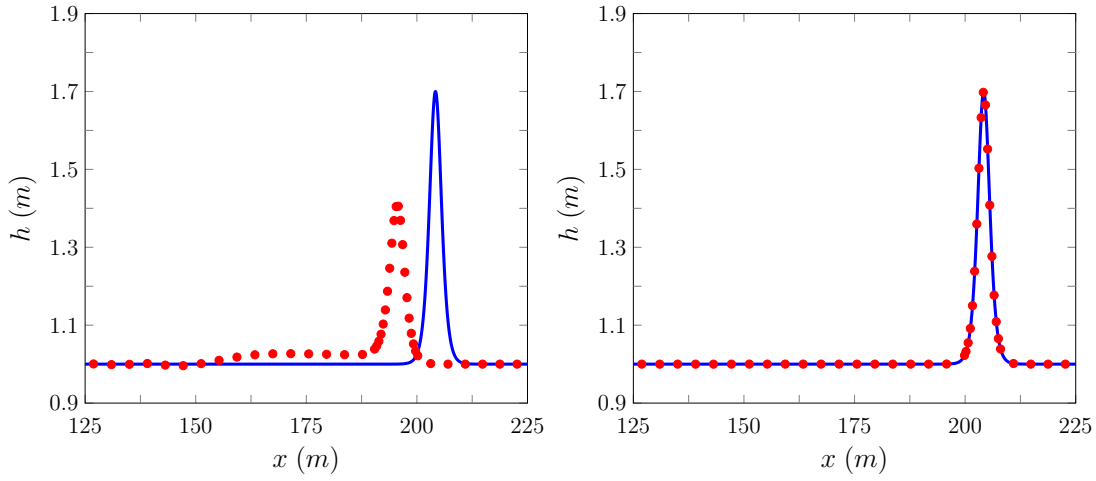

(a) FDVM_1 (b) FDVM_2

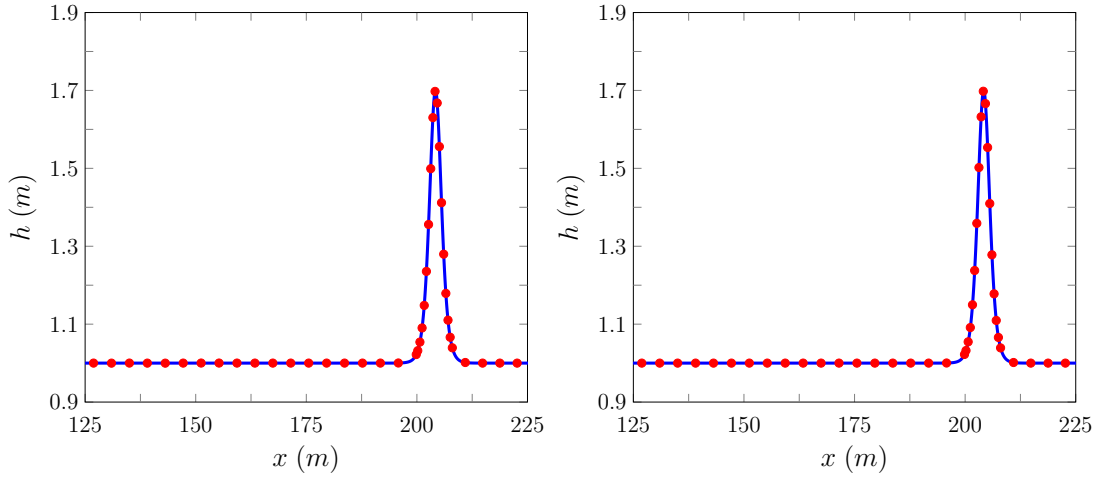

(c) FEVM_2 (d) FDVM_3

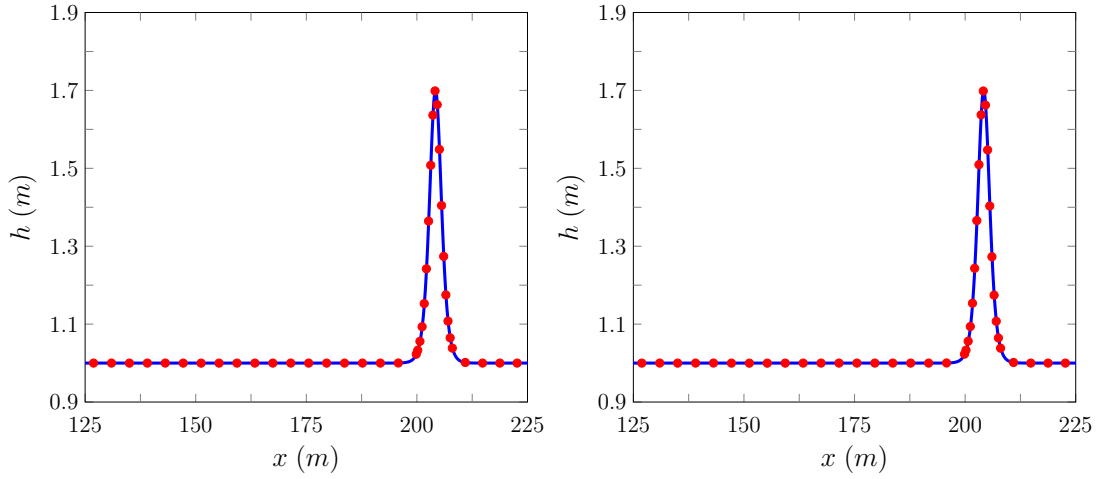

(e) $\mathcal{D}$ (f) $\mathcal{W}$

Figure 5.1: Comparison of the analytic solution (–) and numerical solution with $\Delta x = 100/2^{11}m$ (•) for the soliton problem at $t = 50s$ for all methods.

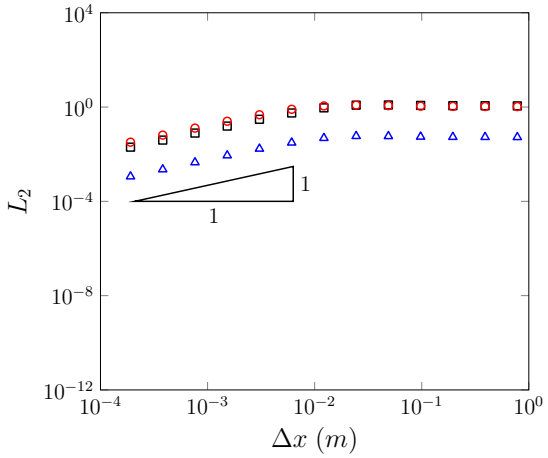

(a) FDVM_1

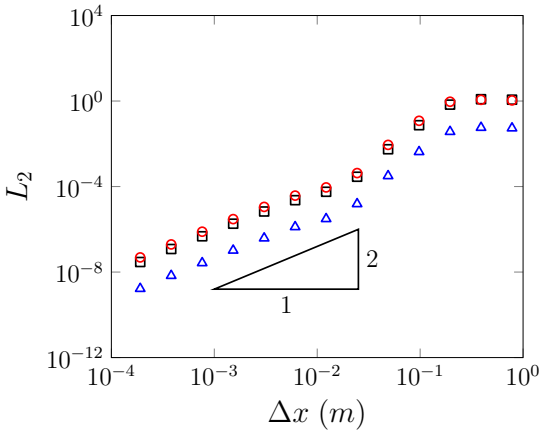

(b) FDVM_2

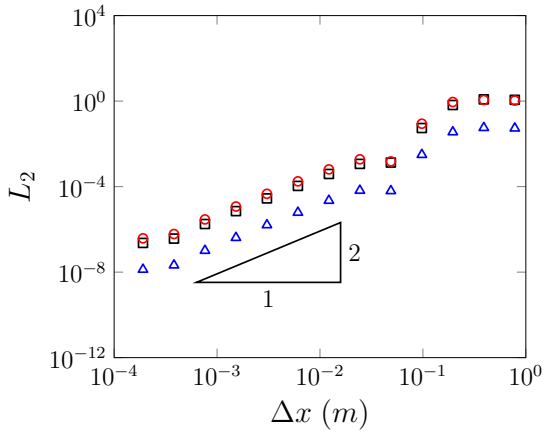

(c) FEVM_2

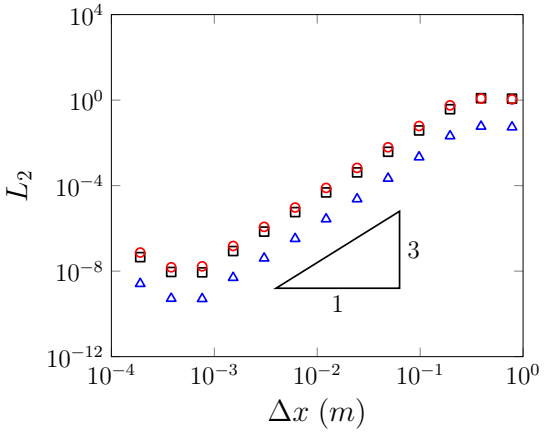

(d) FDVM_3

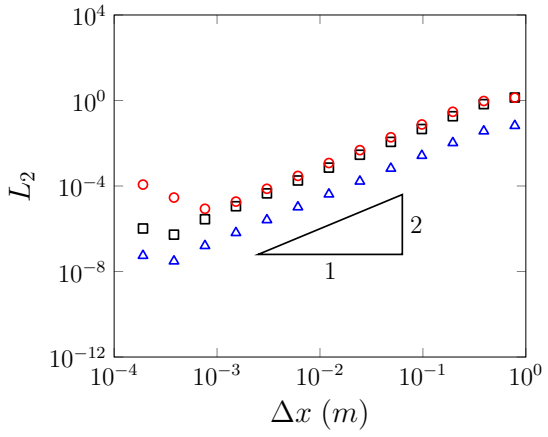

(e) $\mathcal{D}$

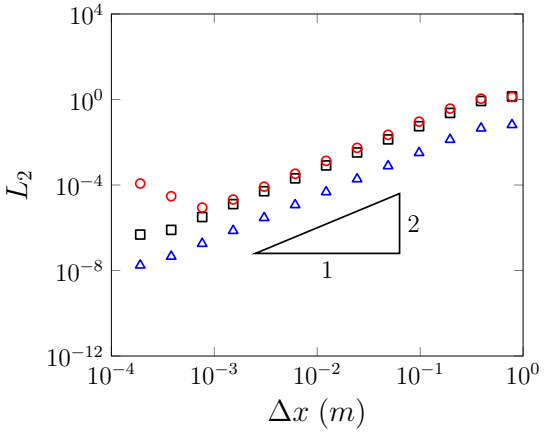

(f) $\mathcal{W}$

Figure 5.2: Convergence as measured by the L_2 norm against Δx for h (△), u (□) and G (○) for the soliton problem for all methods.

solution more accurately than FEVM_2.

The finite difference methods produce very similar errors which are twice as large as the errors from FEVM_2. Additionally, the round-off effects dominate the L_2 error of the finite difference methods at larger Δx values than for the finite volume based methods.

The error in conservation C was calculated for all methods using the analytic expressions for the total amounts of the conserved quantities in the initial conditions (A.1). The error in conservation was plotted against the spatial resolution in Figure 5.3. These results demonstrate that due to the use of the finite volume methods for h and G, both are conserved at round-off error for all the finite volume based methods as expected. While the finite difference methods only conserved h at round-off error because the employed finite difference method for the continuity equation (2.6a) is a conservative method.

No methods conserve $\mathcal{H}$ or the uh within machine precision. Since none of the methods were designed to conserve these quantities this is not surprising, although the error in conservation of all methods for these quantities does exhibit the order of accuracy of the convergence of the numerical method or better, as expected.

For small Δx values the round-off errors dominate the conservation error, particularly for the finite difference methods. Interestingly, FDVM_3 has an accumulation of round-off error increasing the conservation error for h and G as Δx decreases. This was found to be caused by the Runge-Kutta coefficients of the third-order time stepping method [15] not being exactly represented as floating point numbers. For the third-order SSP Runge-Kutta time stepping method the coefficients in the last step are $1/3$ and $2/3$. Since these numbers are not exactly represented in floating point they are approximated with a small error that when summed does not maintain the conservation properties of h and G. Thus, every time step accumulates a small conservation error of machine precision size leading to the observed increase as Δx becomes small and the number of time steps increases. Remedies for this were attempted such as using the coefficients $1/3$ and $(1 - 1/3)$ and bringing the common divisor out but this problem persisted. Some other numerical techniques are required to resolve this issue such as those of Higham [54]. Ultimately, since the convergence of FDVM_3 was only slightly better than FEVM_2 and FDVM_2 [15] it was not developed further and this issue was not resolved.

These results demonstrate the need for higher-order accurate schemes to accurately approximate the Serre equations. Furthermore, they suggest that second-

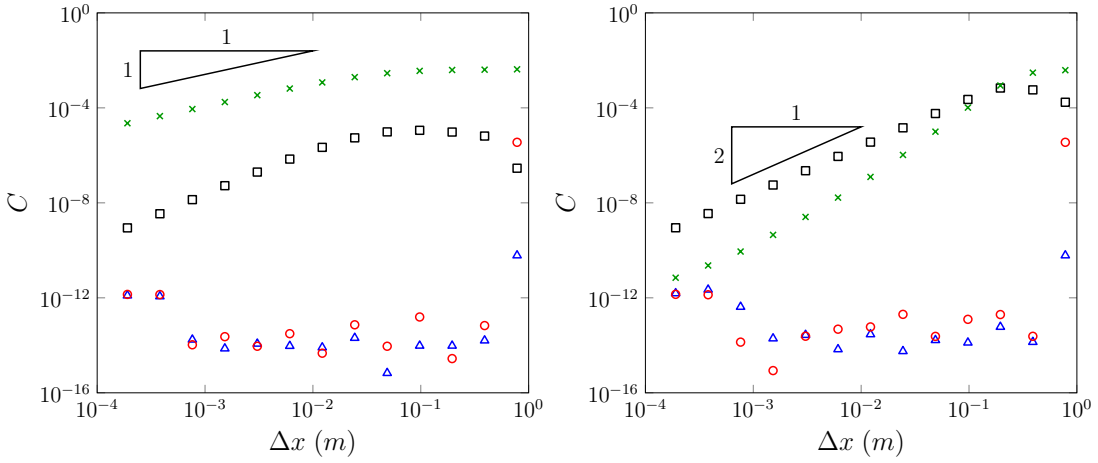

(a) FDVM$_1$

(b) FDVM$_2$

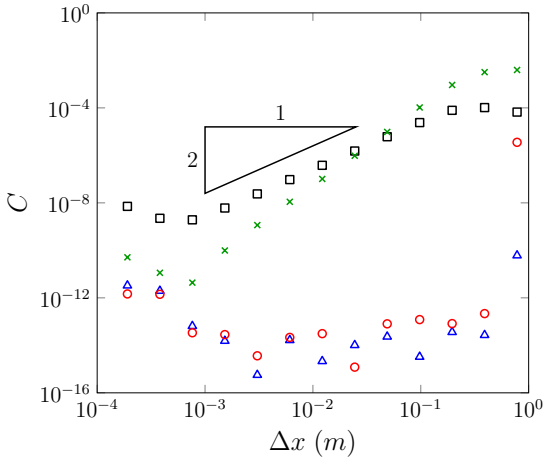

(c) FEVM$_2$

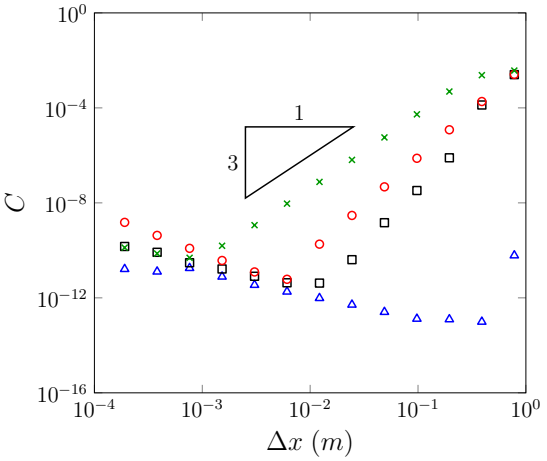

(d) FDVM$_3$

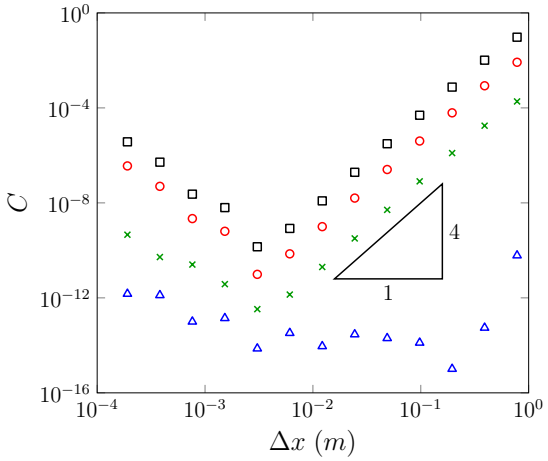

(e) $\mathcal{D}$

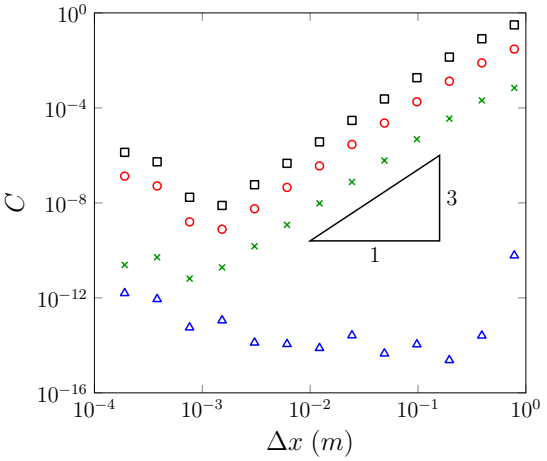

(f) $\mathcal{W}$

Figure 5.3: Conservation error C against Δx for h (△), uh (□), G (○) and $\mathcal{H}$ (×) for the soliton problem for all methods.

order accuracy is sufficient, with third-order accurate schemes showing only a slight improvement. This was also the conclusion of the analytic validation by Zoppou et al. [15]. Finally, they demonstrate the ability of FEVM and FDVM to conserve h and G up to machine precision, as desired. Given these results, only FEVM_2 and FDVM_2 have been extended to allow for variable bathymetry and dry beds. Consequently, the rest of the results in this chapter and Chapter 6 will only consider FEVM_2 and FDVM_2.

5.3 Lake at Rest Solution

To verify the validity of our numerical methods for the Serre equations with variable bathymetry and assess the well balancing method we compare various numerical solutions to the lake at rest solution (2.12).

The particular lake at rest solution (2.12) associated with the bed profile

$$b(x) = a_1 \sin(a_2 x) \tag{5.2}$$

was chosen for this validation to ensure that all terms with derivatives of the bed were tested. To demonstrate the capability of the methods in the presence of dry and wet beds the parameter values $a_0 = 0m$, $a_1 = 1m$ and $a_2 = 2\pi/50m^{-1}$ were chosen. These parameter values result in wet regions with a horizontal free surface where the stage $w(x,t) = h(x,t) + b(x) = a_0 = 0$ (2.12). Therefore, we have a periodic bed where water submerges the troughs of the bed while the peaks of the bed are dry.

For the numerical solutions the spatial domain was $x \in [-112.5m, 87.5m]$ and the final time was $t = 10s$, with the standard gravitational acceleration $g = 9.81m/s^2$. The spatial resolution of the method was varied so that $\Delta x = 100/2^k m$ with $k \in [8, \ldots, 17]$ and the CFL condition (3.22) was satisfied by having $\Delta t = Cr\Delta x/\sqrt{g}$ with condition number $Cr = 0.5$. The standard limiting parameter $\theta = 1.2$ was used in the generalised minmod limiter, (3.2) for both FEVM_2 and FDVM_2. Dirichlet boundary conditions were used at both ends as the analytic solution is stationary.

The numerical methods are assessed by using the specified lake at rest solution as initial conditions and comparing the numerical solutions of FEVM_2 and FDVM_2 at $t = 10s$ to the analytic solution, which are the initial conditions. To demonstrate the utility of the well balancing method the results from two versions of FEVM_2 and FDVM_2 are presented, where the well balancing method described in Chapter 3 is and is not employed.

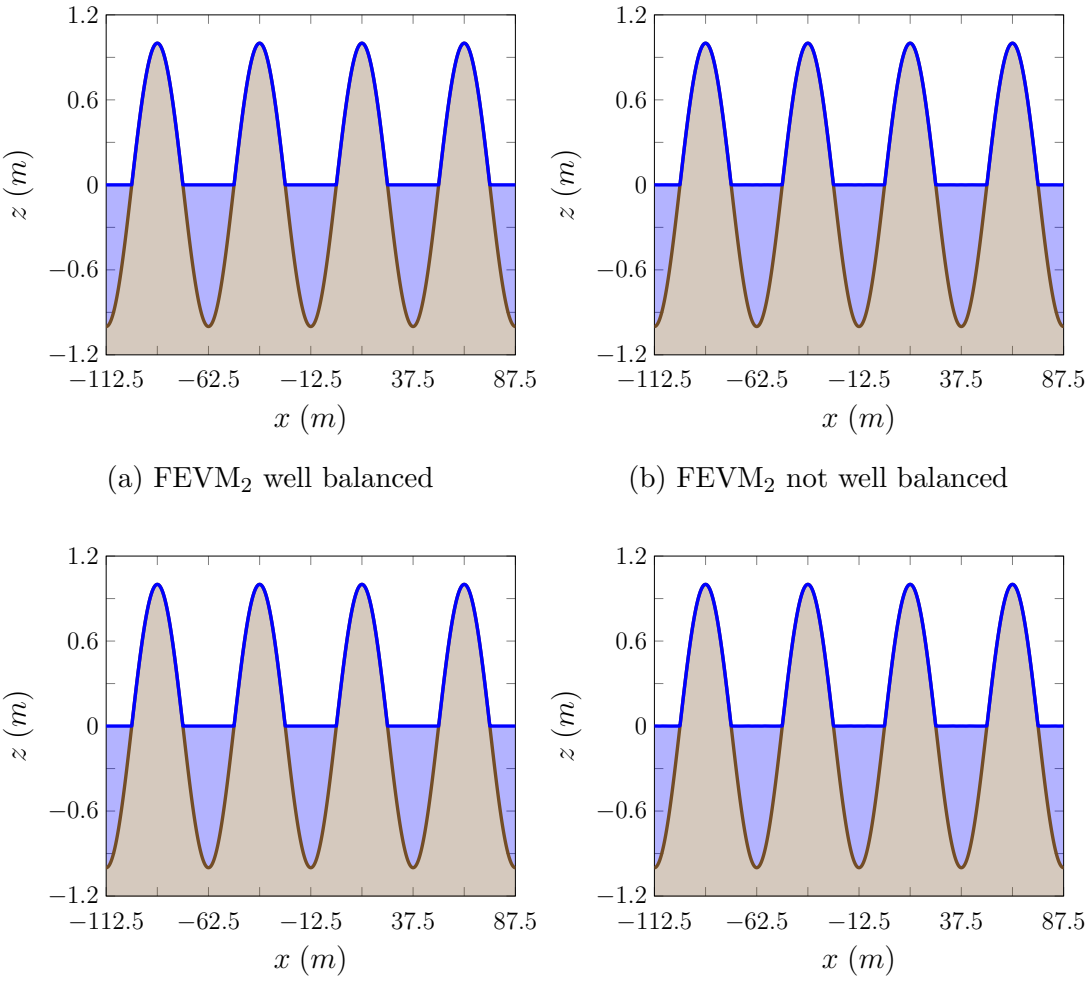

(a) FEVM$_2$ well balanced

(b) FEVM$_2$ not well balanced

(c) FDVM$_2$ well balanced

(d) FDVM$_2$ not well balanced

Figure 5.4: Numerical solutions for w (■) and b (■) with $\Delta x = 100/2^{10}m$ for the lake at rest problem at $t = 10s$ for FEVM$_2$ and FDVM$_2$.

Example numerical solutions with $\Delta x = 100/2^{10}m \approx 0.0977m$ at $t = 10s$ for all versions of FEVM$_2$ and FDVM$_2$ are given in Figure 5.4. The numerical solutions in these figures are indistinguishable from the analytic solutions at this scale and so the analytic solutions have been omitted from the plots.

Examination of the L_2 errors depicted in Figure 5.5 reveals that only the well balanced methods have accurately recovered the analytic solution. With both well balanced versions of the methods reproducing h, G and u precisely, accounting for round-off errors. For G and u their error is increasing due to an accumulation of the round-off errors for each cell and time step; hence their second-order increase as $\Delta x \to 0$. The errors in u produce errors in h through

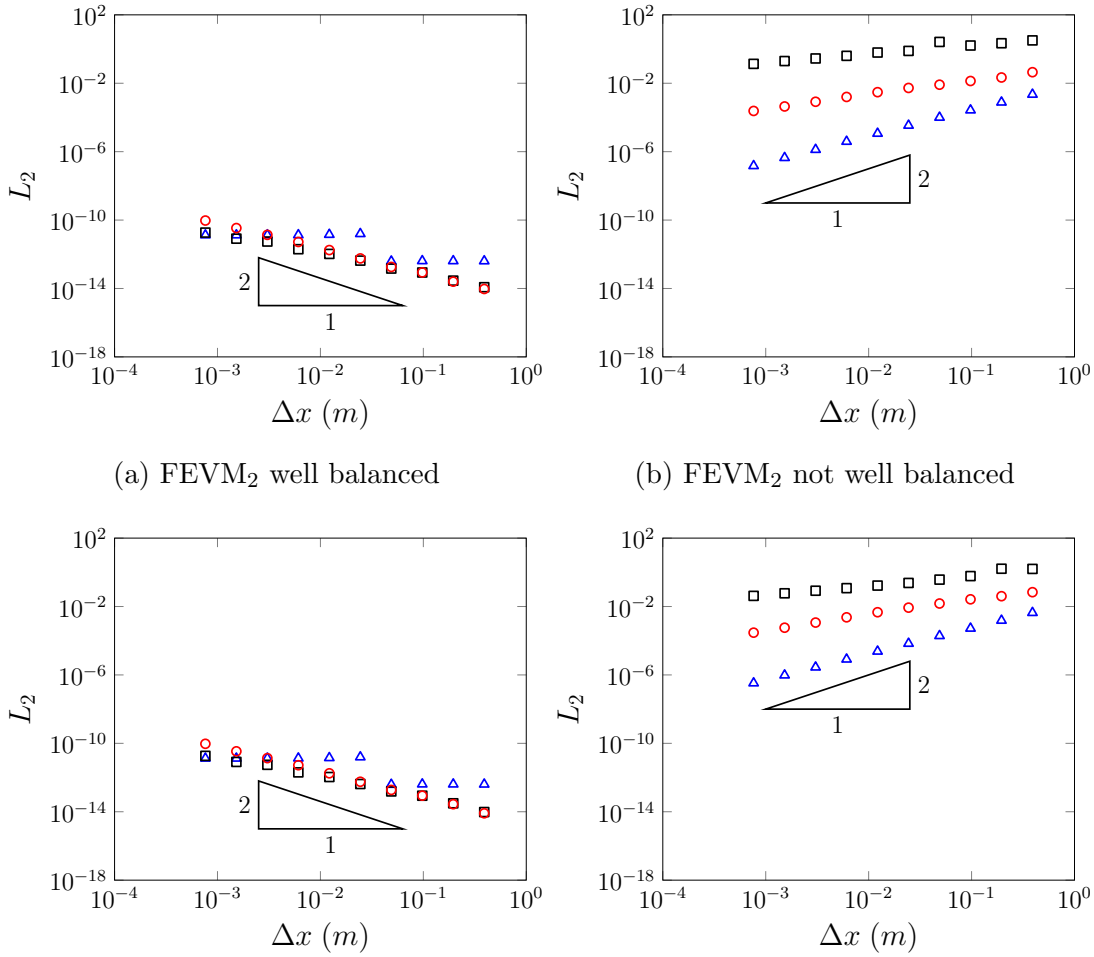

(a) FEVM$_2$ well balanced

(b) FEVM$_2$ not well balanced

(c) FDVM$_2$ well balanced

(d) FDVM$_2$ not well balanced

Figure 5.5: Convergence as measured by the L_2 norm against Δx for h (△), u (□) and G (○) for the lake at rest problem at $t = 10s$ FEVM$_2$ and FDVM$_2$.

its flux function increasing the error in h as Δx decreases. However, since h is far larger than u these effects have a more complicated relationship to the cell width.

For methods without well balancing; the errors are significantly larger, yet they are converging to the analytic solution. However, the order of accuracy of the convergence in u and G has degraded and is not the expected second-order accuracy observed for h. The poor convergence of u and G is a result of the errors in u and G not being damped by the method. Thus errors generated by the imbalance between the flux and source terms increase over time degrading the order of accuracy. The second-order accuracy in h is retained for the presented Δx values as these errors introduced in u and G are small for a single cell, although

for smaller Δx values these errors in u and G will begin to dominate the errors in h.

Using the expressions in Appendix A for the total amounts of the conserved quantities the conservation error C was calculated for FEVM_2 and FDVM_2 with the results plotted in Figure 5.6. The error in conservation of these methods affirms the superiority of the well-balanced version of the methods. In particular, we see that the total amounts of uh and G are only conserved within machine precision when well balancing is employed. Since uh and G are uniformly zero in the initial conditions the well balanced methods have only introduced round-off errors into these quantities, whilst without well balancing large errors in these quantities are introduced in the naive methods.

The errors in conservation of h and $\mathcal{H}$ for the well balanced methods are large, but do converge at the order of accuracy of the scheme or better. These errors are caused by the discretisation of the initial conditions, primarily the approximation of the boundaries of the wet regions by the numerical grids. This initial discretisation error can be removed by comparing the total amounts of the conserved quantities in the numerical solution to their numerically calculated total amounts in the initial conditions with C^* as in Figure 5.7. For the completely numerically calculated conservation error C^* we observe that all the conserved quantities are conserved at machine precision for the well balanced methods. With $\mathcal{H}$ being conserved exactly for most numerical solutions, hence its disappearance from the log-log plot. The conservation error of $\mathcal{H}$ is small for the lake at rest solution since u is very small. Hence, $\mathcal{H}$ is essentially the gravitational potential energy which since mass is well conserved is also well conserved.

These results demonstrate the need for well-balancing for both numerical methods, as it is only with its inclusion that the lake at rest steady state can be accurately reproduced.

5.4 Forced Solutions

The previous analytic solution validations do not provide a stringent test for all terms present in the Serre equations and there are currently no known analytic solutions that do. To remedy this the forced solutions introduced in Chapter 2 were used to validate the numerical methods. Since the source terms in the modified Serre equations, (2.13) can be determined and accounted for analytically, the only source of error in the numerical solutions reproduction of the forced

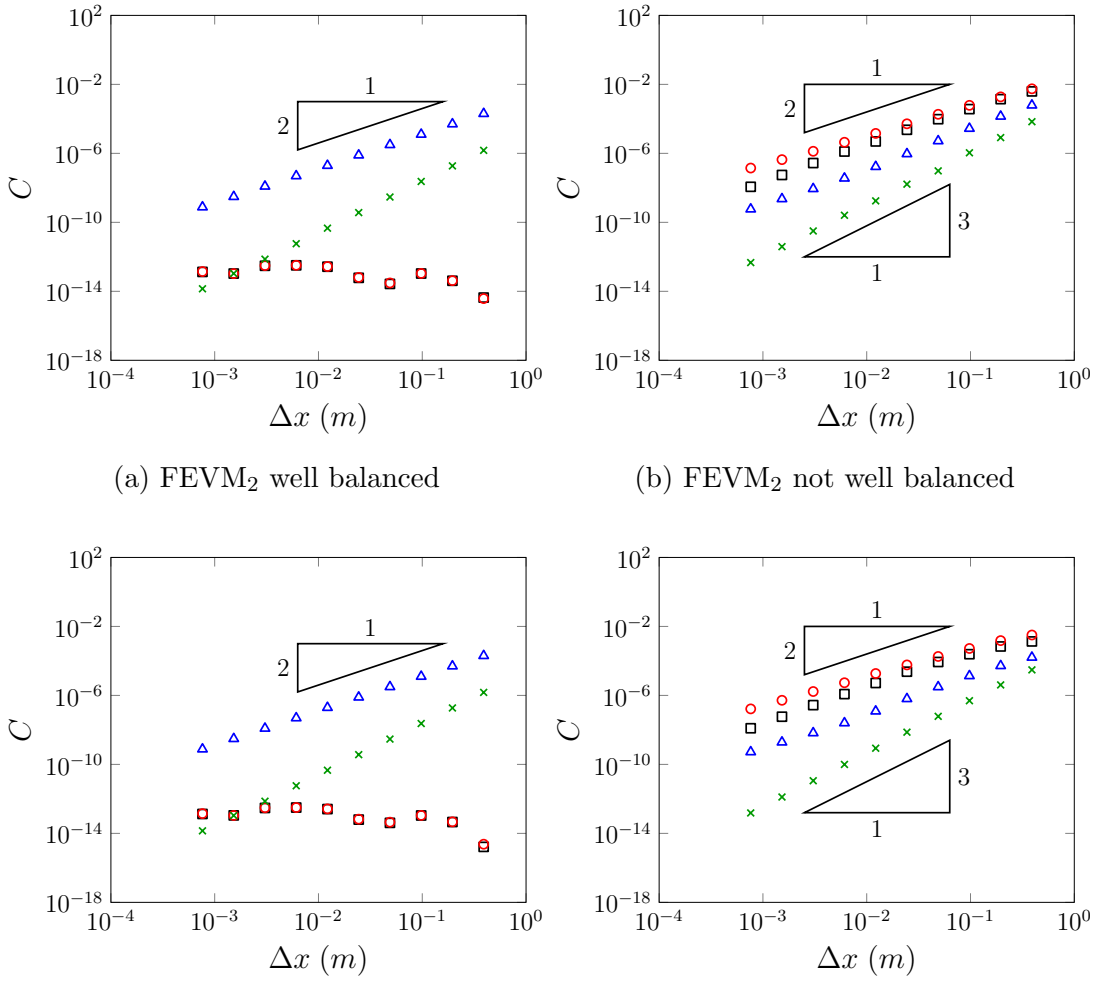

(a) FEVM$_2$ well balanced

(b) FEVM$_2$ not well balanced

(c) FDVM$_2$ well balanced

(d) FDVM$_2$ not well balanced

Figure 5.6: Conservation error C against Δx for h (△), uh (□), G (○) and $\mathcal{H}$ (×) for the lake at rest problem at $t = 10s$ for FEVM$_2$ and FDVM$_2$.

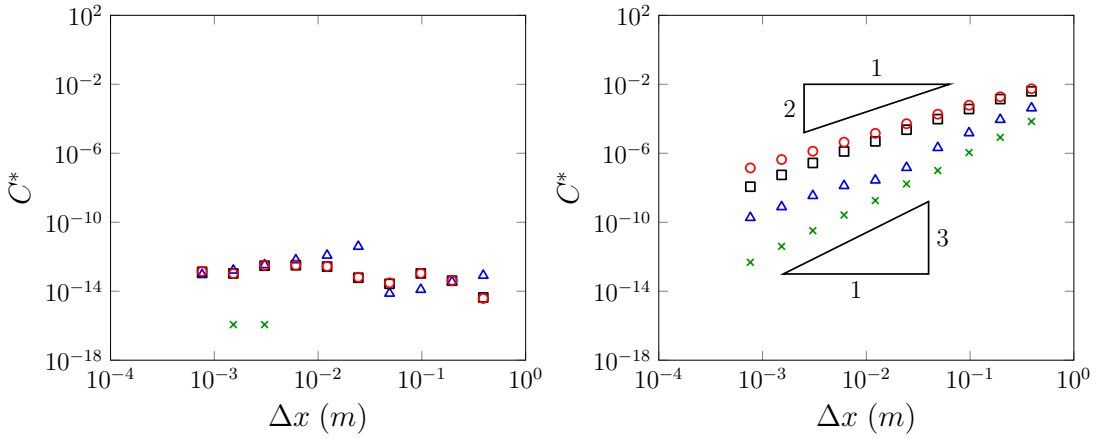

(a) FEVM$_2$ well balanced

(b) FEVM$_2$ not well balanced

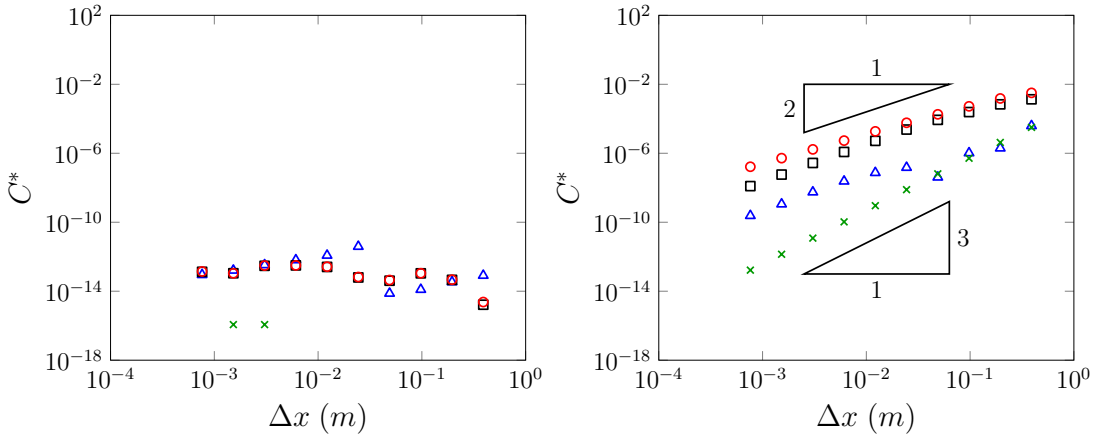

(c) FDVM$_2$ well balanced

(d) FDVM$_2$ not well balanced

Figure 5.7: Conservation error using only numerical calculations C^* against Δx for h (△), uh (□), G (○) and $\mathcal{H}$ (×) for the lake at rest problem at $t = 10s$ for FEVM$_2$ and FDVM$_2$.

solutions are the numerical methods themselves and thus the theoretical second-order accuracy of FEVM_2 and FDVM_2 should be recovered.

We performed validation tests for two forced solutions; one with a finite water depth everywhere and the other with a dry bed to validate and compare the numerical solutions in both situations. To ensure that all terms of the Serre equations were accurately approximated in the numerical method the functions

$$h^*(x,t) = a_0 + a_1 \exp\left(-\frac{\left[(x - a_2 t) - a_3\right]^2}{2a_4}\right), \tag{5.3a}$$

$$u^*(x,t) = a_5 \exp\left(-\frac{\left[(x - a_2 t) - a_3\right]^2}{2a_4}\right), \tag{5.3b}$$

$$b^*(x) = a_6 \sin\left(a_7 x\right) \tag{5.3c}$$

for the primitive variables were chosen. These functions produce an a_1 high Gaussian bump for h and u that travels at a fixed speed a_2 over a periodic bed. Thus the solutions h and u will have constant shape and be translated to the right over time. However, this is not the case for G as u and h have constant shape but the bed is periodic. Therefore, the bed terms in G (2.7) will change the shape of G as the Gaussian bump in h and u encounters different bed slopes.

For non-trivial choices of the parameters a_i all terms in the Serre equations vary in space and time and so all terms must be accurately approximated by the numerical method to adequately reproduce the forced solution.

Both validation studies used the values $a_1 = 0.5m$, $a_2 = 2\pi/\left(10a_7\right) m/s$, $a_3 = -3\pi/\left(2a_7\right) m$, $a_4 = \pi/(16a_7)m^2$, $a_5 = 0.5m/s$, $a_6 = 1.0m$ and $a_7 = \pi/25m^{-1}$ with $a_0 = 1m$ for the finite water depth forced solution and $a_0 = 0m$ for the dry bed forced solution. These parameter values result in a Gaussian bump in h and u that has a width much smaller than the wavelength of the bed profile and travels precisely one wavelength in $10s$.

The domain of the numerical solutions was $x \in [-112.5m, 87.5m]$ with $t \in [0s, 10s]$. The standard gravitational acceleration $g = 9.81m/s^2$ was used. The spatial resolution of numerical methods was varied like so $\Delta x = 100/2^k m$ with $k \in [8, \ldots, 17]$. To satisfy the CFL condition, (3.22) the temporal resolution $\Delta t = Cr\Delta x/\left(a_2 + a_5 + \sqrt{g\left(a_0 + a_1\right)}\right)$ was chosen with condition number $Cr = 0.5$. The value $\theta = 1.2$ was used in the generalised minmod limiter (3.2) for both FEVM_2 and FDVM_2 and Dirichlet boundary conditions were applied at the boundaries of the domain.

5.4.1 Results for a Wet Bed

For the non-zero water depth case where $a_0 = 1m$ an example of the numerical solutions of FEVM_2 and FDVM_2 are given in Figures 5.8 and 5.9 respectively for $\Delta x = 100/2^{10}m \approx 0.0977m$ at various times. The numerical solutions and the forced solutions are distinguishable at all times for these scales, accurately reproducing the forced solution as it travels over the bed. Thus h and u maintain their constant shape while G does not due to the influence of the periodic bed.

The L_2 error of h, u and G for the FEVM_2 and FDVM_2 are given in Figure 5.10. Both methods recover the expected second-order accuracy. Since the source term of the modified Serre equations is added analytically and all terms must be accurately approximated by the method for this forced solution, these results demonstrate that FEVM_2 and FDVM_2 are second-order accurate for all terms when the bed is wet everywhere, as desired.

5.4.2 Results with a Dry Bed

To demonstrate the capability of the methods to handle wetting and drying of a bed, a series of numerical simulations of the forced solutions (5.3a) where $a_0 = 0m$ were conducted using both FEVM_2 and FDVM_2.

Example numerical solutions demonstrating the evolution of the wave are given in Figure 5.11 for FEVM_2 and Figure 5.12 FDVM_2 with $\Delta x = 100/2^{10}m \approx 0.0977m$ at various times. The methods accurately reproduce the analytic solution for the stage w, h and G. However, both fail to accurately reproduce u when h is small, particularly behind the Gaussian bump. So that now h is the only quantity that maintains a constant shape in the numerical solutions, as G changes due to the periodic bed and u changes due to numerical errors.

These large errors in u when h is small are caused by the particular choices $h_{base} = 10^{-8}$ and $h_{tol} = 10^{-12}$ used in the desingularisation transformation applied to the FEM (3.11). By choosing larger values of these quantities the errors in u can be significantly damped. However, if h_{base} and h_{tol} are larger they begin to dominate the L_2 errors in h, G and uh making the convergence less obvious. This trade-off is present in all desingularisation transforms.

For our purposes the chosen desingularisation transform (3.26) with small h_{base} and h_{tol} values are sufficient, resulting in large observed errors in u when h is small.

The L_2 errors for h, u, uh and G for both methods are given in Figure 5.13. Both methods exhibit second-order convergence in all the quantities except u.

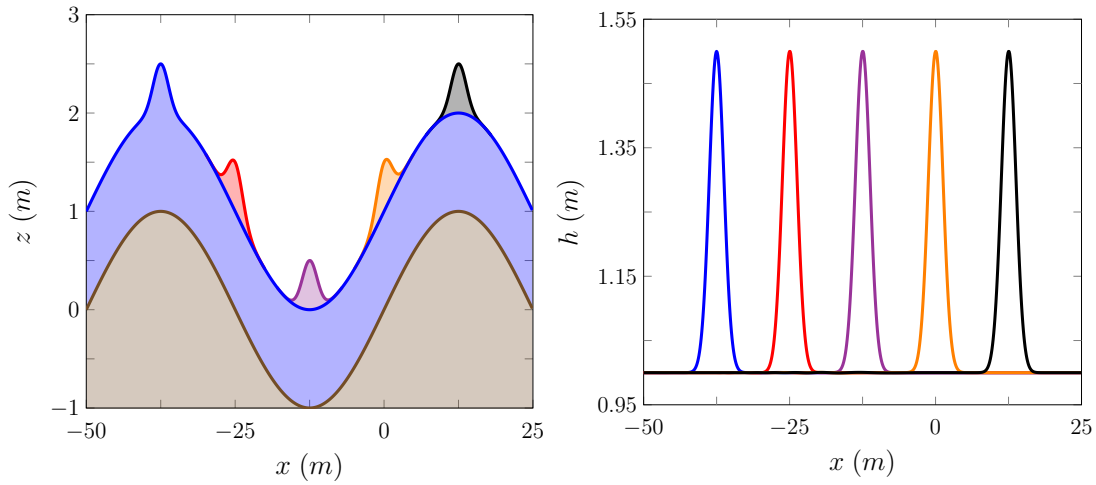

(a) w and b (■) (b) h

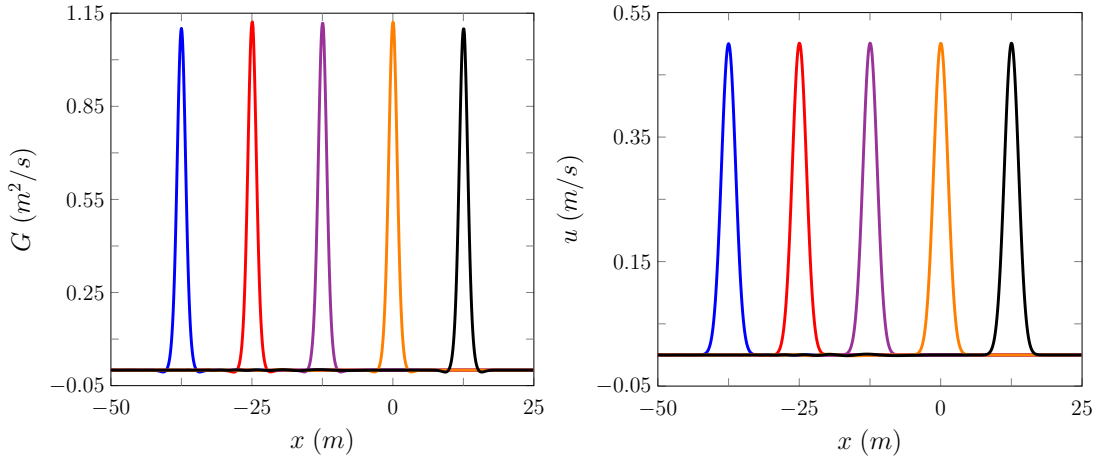

(c) G (d) u

Figure 5.8: Numerical solutions for w, b, h, G and u produced by FEVM$_2$ with $\Delta x = 100/2^{10}m$ at $t = 0s$ (– / ■), $2.5s$ (–/ ■), $5.0s$ (– / ■), $7.5s$ (–/ ■), $10.0s$ (– / ■) to the wet bed forced solution problem, where $a_0 = 1m$.

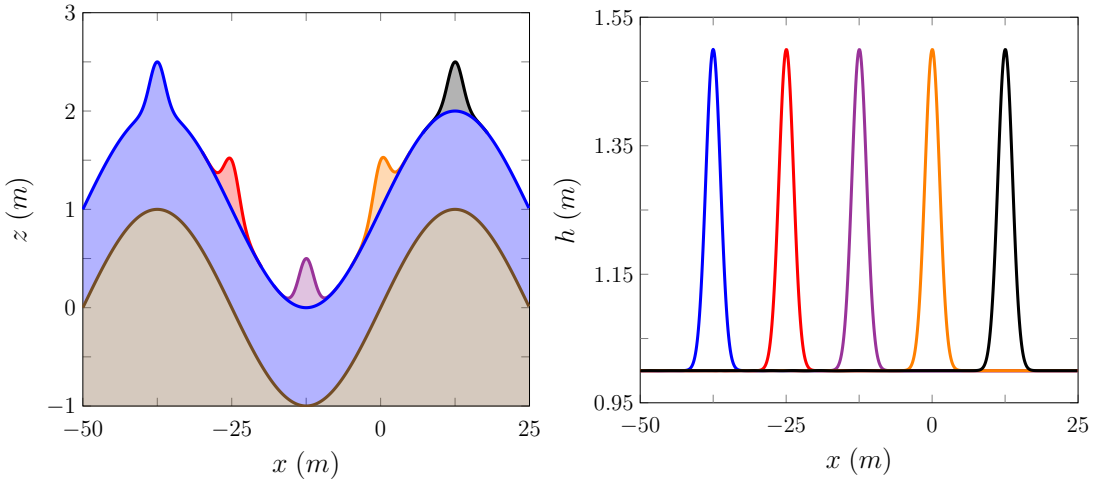

(a) w and b (□) (b) h

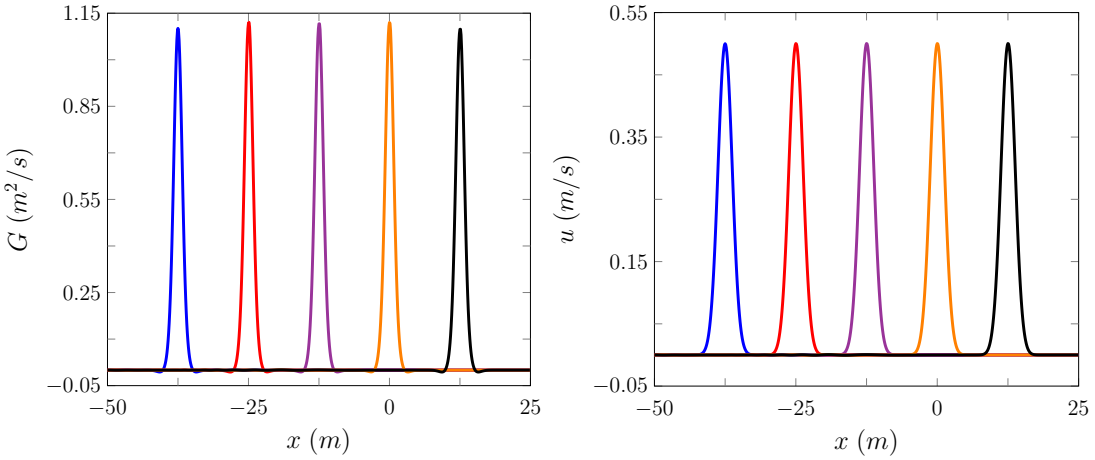

(c) G (d) u

Figure 5.9: Numerical solutions for w, b, h, G and u produced by FDVM$_2$ with $\Delta x = 100/2^{10}m$ at $t = 0s$ (– / □), $2.5s$ (–/ □), $5.0s$ (– / □), $7.5s$ (–/ □), $10.0s$ (– / □) to the wet bed forced solution problem, where $a_0 = 1m$.

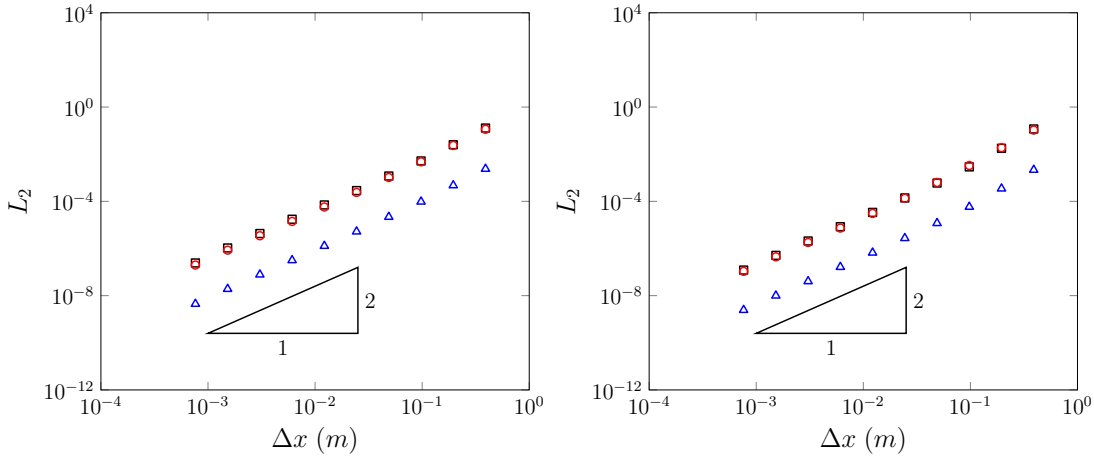

(a) FEVM_2 (b) FDVM_2

Figure 5.10: Convergence as measured by the L_2 norm against Δx for h (△), u (□) and G (○) for the wet bed forced solution problem for FEVM_2 and FDVM_2 at $t = 10s$.

The large errors in u only occur when h is small. This can be seen by restricting our convergence to only compare regions where $h > 10^{-3}m$ as in Figure 5.14. It can be seen that the expected second-order accuracy in u is recovered when h is not small. Since all the flux and source terms of the Serre equations (2.6) only depend on u multiplied by some power of h; the large errors in u when h is small do not translate to significant errors in G, h or uh.

Therefore, these methods can accurately handle the dry bed problem, even with small h_{base} and h_{tol} values, although in such cases the velocity may have large errors in regions where h is small. For physical applications where large errors in u when h is small are not acceptable we recommend altering the dry bed handling of the scheme by increasing the h_{base} and h_{tol} values or altering the desingularisation transformation [50].

In this chapter the analytic and forced solutions were used to assess the numerical methods. It was found that the finite volume based methods performed better than the finite difference methods and that second-order methods were sufficient to accurately reproduce the analytic solutions. Finally the second-order accuracy of FEVM_2 and FDVM_2 was confirmed for the wetting and drying of variable beds using forced solutions to the Serre equations.

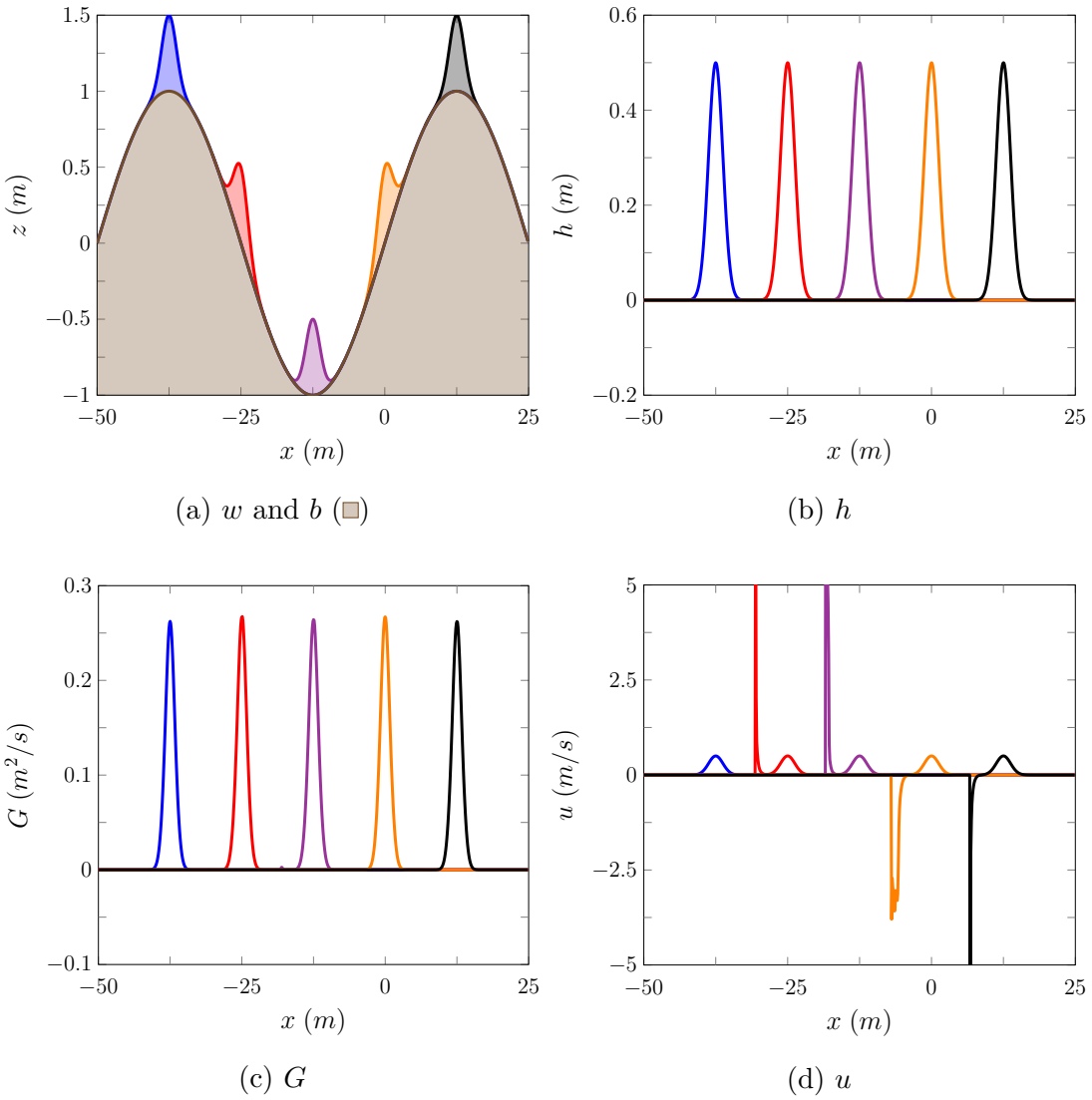

(a) w and b (□)

(b) h

(c) G

(d) u

Figure 5.11: Numerical solutions for w, b, h, G and u produced by FEVM$_2$ with $\Delta x = 100/2^{10} m$ at $t = 0s$ (– / □), $2.5s$ (–/ □), $5.0s$ (– / □), $7.5s$ (–/ □), $10.0s$ (– / □) to the dry bed forced solution problem, where $a_0 = 0m$.

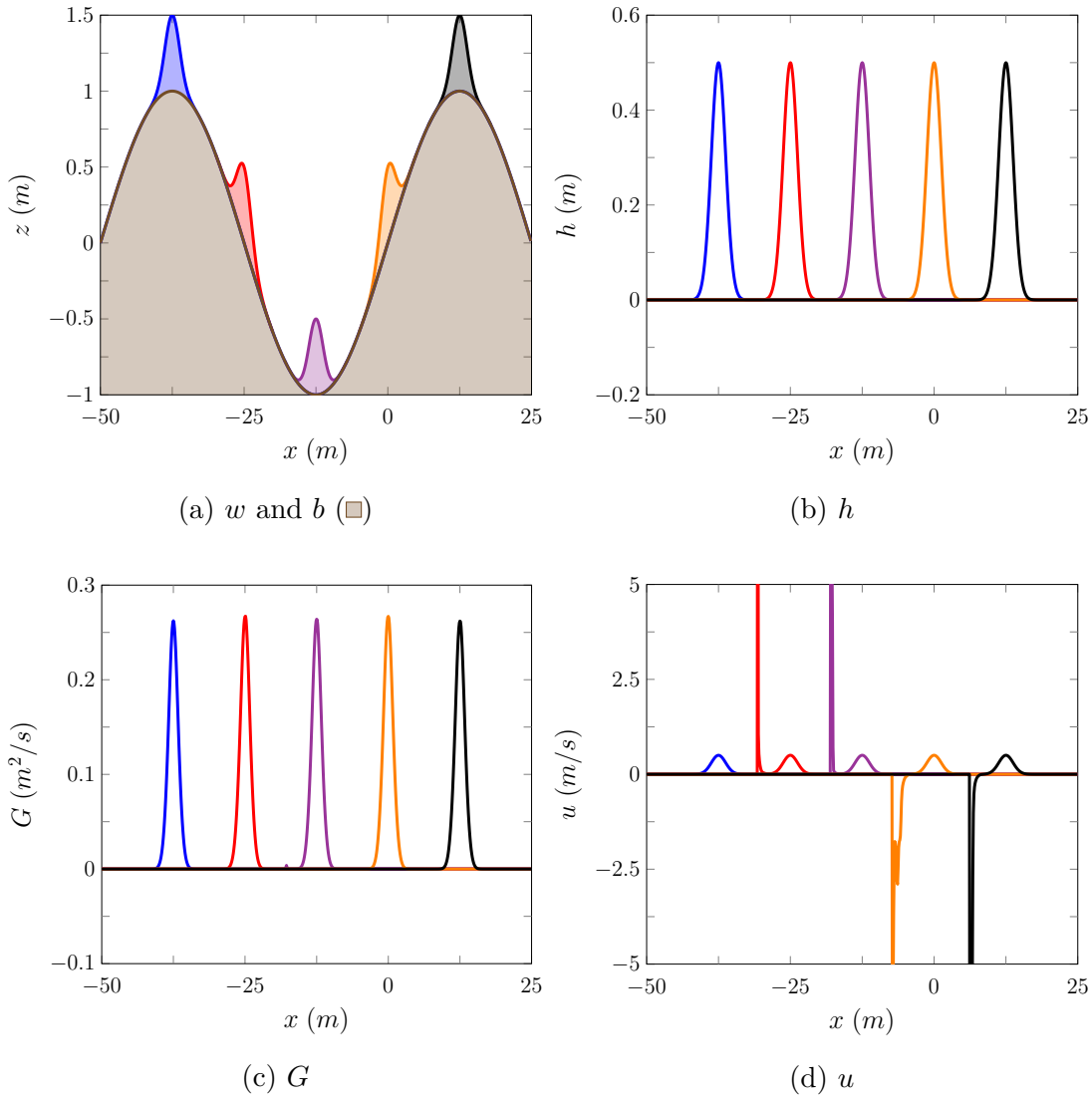

(a) w and b (■)

(b) h

(c) G

(d) u

Figure 5.12: Numerical solutions for w, b, h, G and u produced by FDVM$_2$ with $\Delta x = 100/2^{10}m$ at $t = 0s$ (– / ■), $2.5s$ (–/ ■), $5.0s$ (– / ■), $7.5s$ (–/ ■), $10.0s$ (– / ■) to the dry bed forced solution problem, where $a_0 = 0m$.

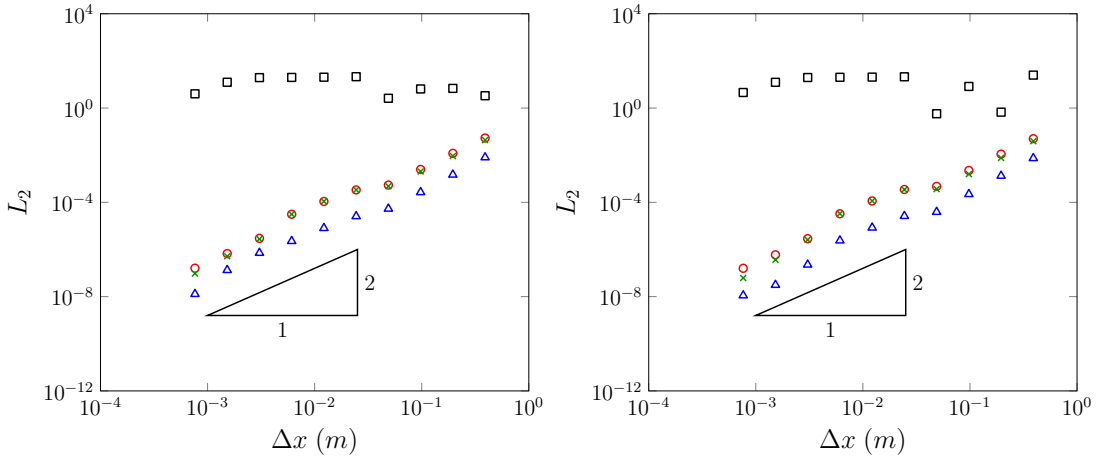

(a) FEVM$_2$ (b) FDVM$_2$

Figure 5.13: Convergence as measured by the L_2 norm against Δx for h (△), u (□), uh (×) and G (○) for the dry bed forced solution problem for FEVM$_2$ and FDVM$_2$ at $t = 10s$.

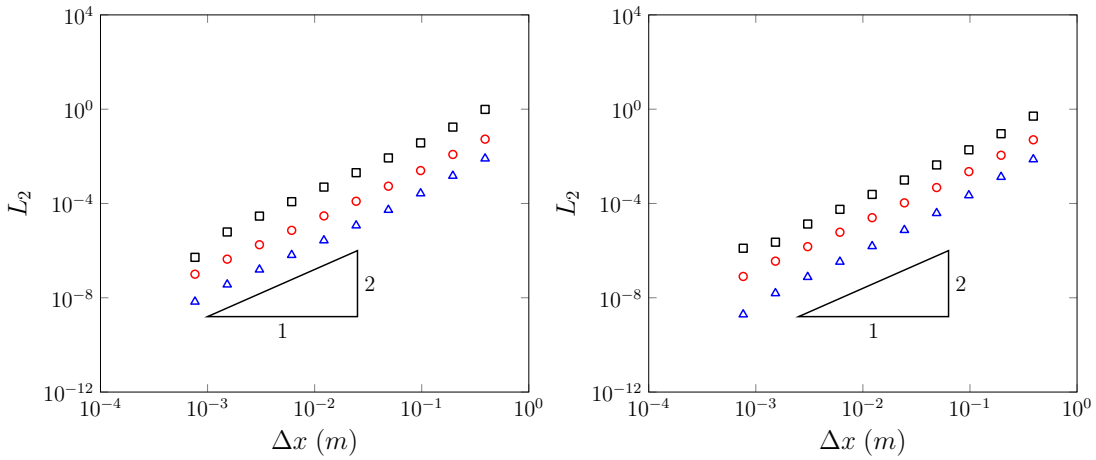

(a) FEVM$_2$ (b) FDVM$_2$

Figure 5.14: Convergence for regions where $h > 10^{-3}m$ as measured by the L_2 norm against Δx for h (△), u (□) and G (○) for the dry bed forced solution problem for FEVM$_2$ and FDVM$_2$ at $t = 10s$.

Chapter 6

Experimental Validation

The numerical methods $FDVM_2$ and $FEVM_2$ are experimentally validated by comparing their numerical solutions to experimental data. The chosen experiments allow the methods capability to model a variety of physical situations to be tested. These situations include the presence of steep gradients in the flow, the interaction of strong dispersive waves with varying bathymetry, shoaling and wave-breaking and finally the wetting and drying of a sloping beach. Thus, the ability of these methods to robustly reproduce all the experimental results well strongly demonstrates their capability to model a variety of physical situations.

6.1 Evolution of a Negative Rectangular Wave

A series of experiments studying the evolution of a negative rectangular wave in the free-surface were conducted by Hammack and Segur [55]. These experiments were performed in a wave tank that was $0.394m$ wide, $31.6m$ long and $0.61m$ high. The rectangular negative waves were generated using a piston $0.61m$ long with its left edge against the wave tank wall. The $0.1m$ deep water is initially stationary with a horizontal free surface and the piston in the up position. The experiment begins when the piston suddenly moves down. This creates a sudden negative rectangular wave in the water surface generating a dispersive wave train that is recorded at wave gauges located $0m$, $5m$, $10m$, $15m$ and $20m$ away from the right edge of the piston. A diagram of the longitudinal section of the wave-tank with the wave gauge locations marked is given in Figure 6.1.

These experiments provide a good benchmark for the capability of the numerical method to accurately model problems with steep gradients in the free surface. These experiments are affected by bed friction and viscosity and the

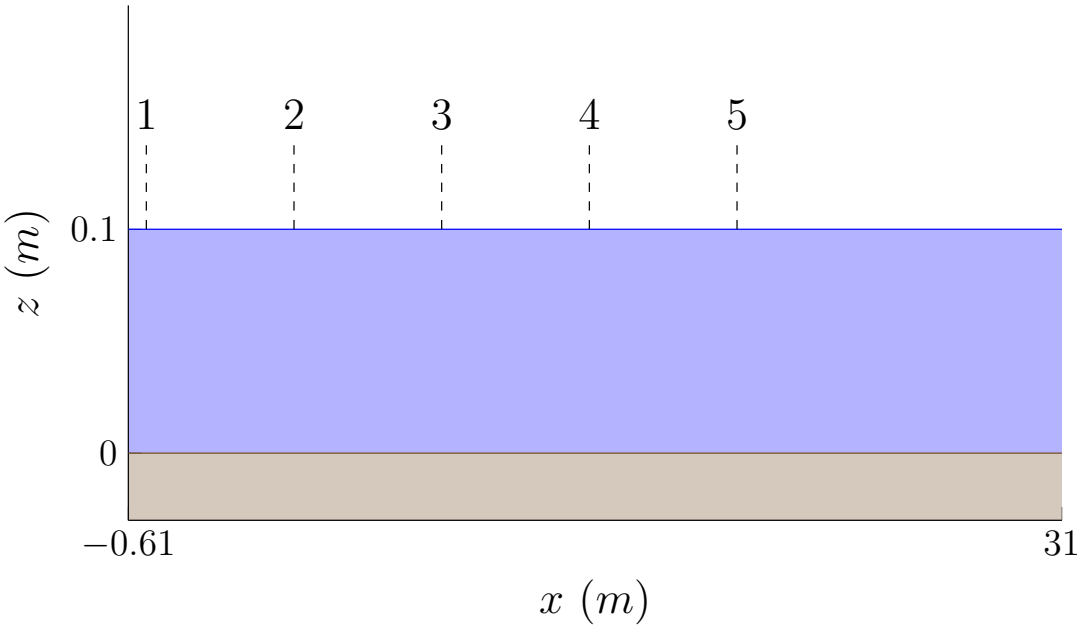

Figure 6.1: Diagram showing a longitudinal section of the wave tank for evolution of a negative rectangular wave experiments with the water (■), the bed (■) and the numbered wave gauge marked.

inability of the piston and water to move vertically instantaneously and slip free. Since the Serre equations do not contain viscosity, bed friction was neglected and discontinuous initial conditions are used to model the negative rectangular wave we expect that the numerical solutions of the Serre equations may produce many more oscillations in the dispersive wave train than are observed experimentally [14].

Hammack and Segur [55] report the results for two different initial negative wave amplitudes $0.01m$ and $0.03m$, resulting in the non-linearity parameters $\epsilon = 0.1$ and $\epsilon = 0.3$ respectively. Since these non-linearity parameters are relatively small there was no breaking of waves throughout the experiment.

This experiment was modelled numerically using the reflected problem, with the left wall of the wave tank as the axis of symmetry. In the numerical experiments the domain is $[-60m, 60m]$ and the experiment is run for $50s$ with $g = 9.81m/s^2$. For the spatial resolution we set $\Delta x = 0.01m$ to satisfy the CFL condition, (3.22) $\Delta t = 0.5\Delta x/\sqrt{g\ 0.1}$. The limiting parameter $\theta = 1.2$ was used in the reconstruction (3.2) in FEVM_2 and FDVM_2.

These results in these experiments were published for FDVM_2 [15] and have been extended here with the inclusion of the conservation error of h, G and uh

in the numerical simulation of both experiments.

6.1.1 Results for $0.01m$ Negative Rectangular Wave

Plots comparing the numerical and experimental wave gauge data for the $0.01m$ negative rectangular wave are displayed in Figures 6.2 and 6.4 for FEVM_2 and FDVM_2 respectively. We present this data using the same dimensionless scales as reported in the original paper [55]. Tables 6.1 and 6.2 which display the completely numerically calculated error in conservation C^* are also provided.

The numerical solutions agree well with the experimental results; particularly for the front of the dispersive wave train. While all the conserved quantities have indeed been conserved well by the methods.

The numerical solutions produce larger and consequently faster waves and observe oscillations in the dispersive wave train which are not present in the experimental data of wave gauge 1. Moreover, as expected the methods produce many more oscillations than were observed experimentally. These discrepancies can be attributed to the lack of viscosity and the omission of bed friction for the Serre equations in this thesis (2.6). Furthermore, it is highly likely the experiment produced some smooth approximation to a discontinuous jump in the water depth with the down-stroke of the piston. Such a smoothing of the initial conditions will significantly attenuate the high frequency waves in the generated dispersive wave train [14]. Given these differences the numerical methods do a very good job of replicating the experimental behaviour.

These numerical solutions compare well to those of Zoppou et al. [15] for FDVM_2 with $\Delta x = 0.005m$, $\Delta t = 0.2\Delta t/\sqrt{g0.1}s$ and $\theta = 1$. Where a higher resolution and a more diffusive value of the limiting parameter is chosen. These differences had little impact on the results at the wave gauges. While the more diffusive value of the limiting parameter negatively impacts the conservation of $\mathcal{H}$ reported by Zoppou et al. [15]. This is because when $\theta = 1$ the reconstruction diffuses the initial steep gradient, negatively affecting the conservation of $\mathcal{H}$ [14].

Both FEVM_2 and FDVM_2 have produced indistinguishable results at this scale and have demonstrated very good conservation of all the quantities see, Tables 6.1 and 6.2. Given the extensive examination of several numerical schemes for steep gradient problems [14], this indicates that these solutions are indicative of true solutions of the Serre equations. However, these results do not demonstrate the superiority of one of these methods over the other.

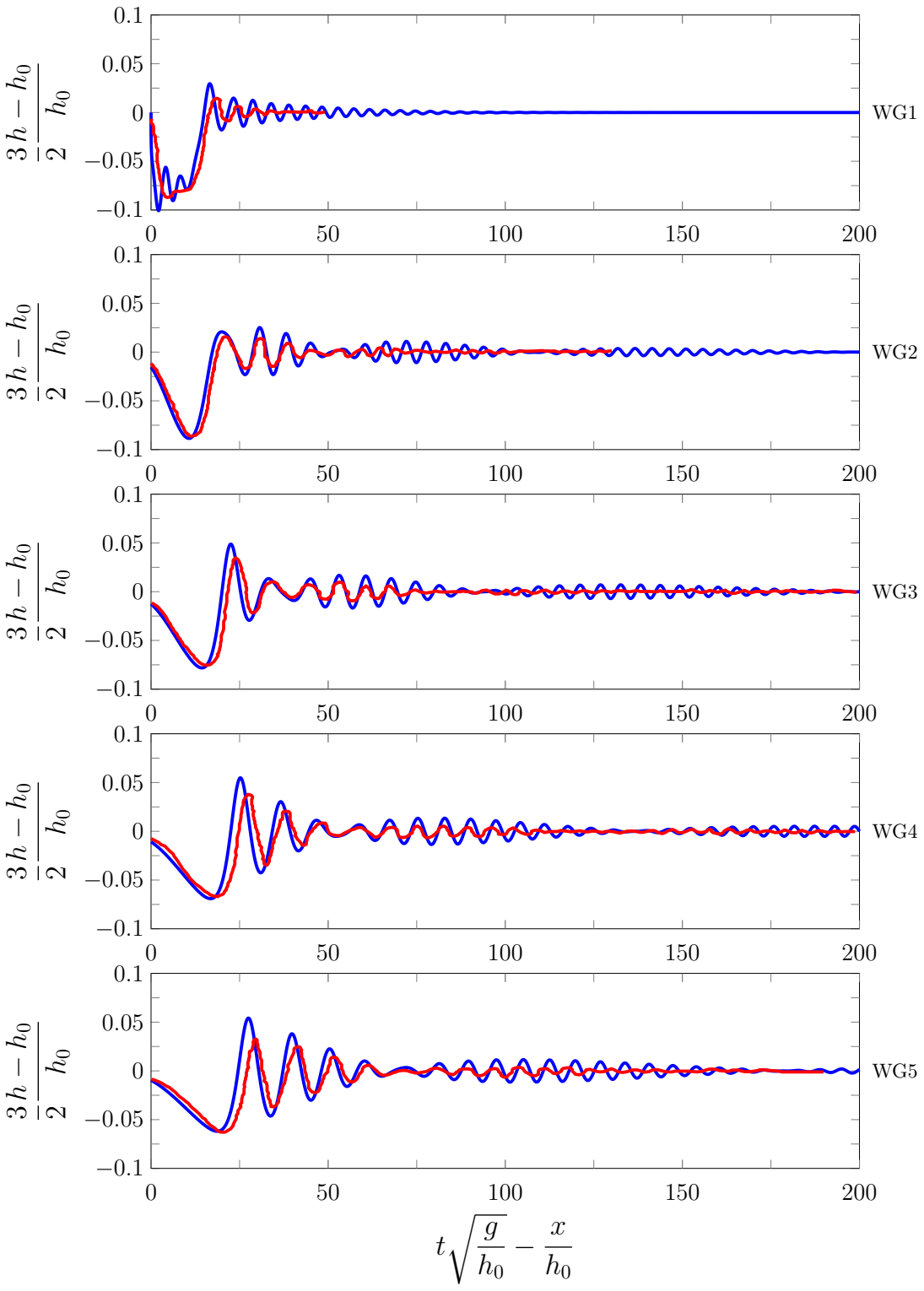

Figure 6.2: Time series of the experimental wave gauge data (–) and numerical results (–) of FEVM$_2$ for the $0.01m$ negative rectangular wave.

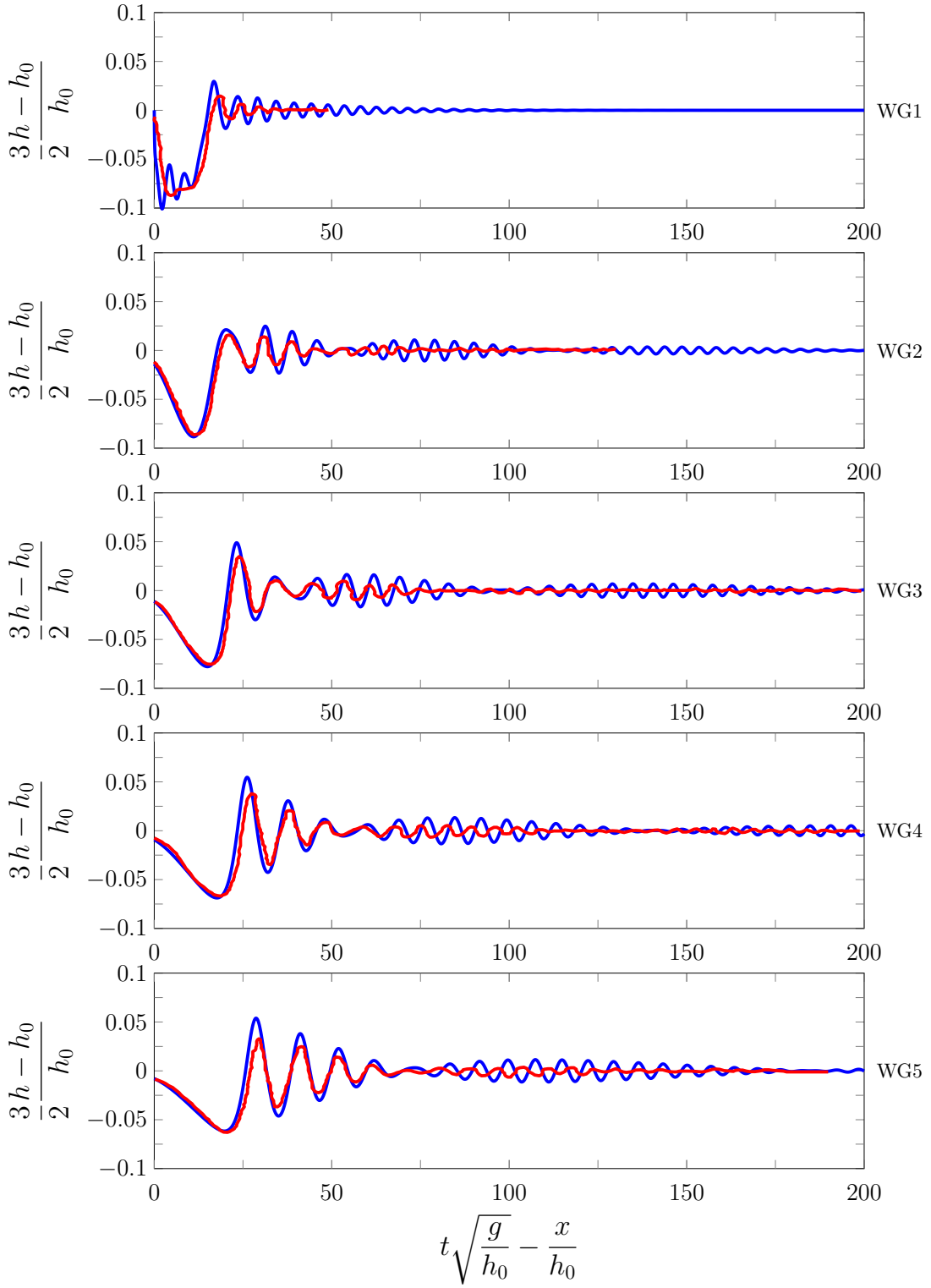

Figure 6.3: FDVM

Figure 6.4: Time series of the experimental wave gauge data (–) and numerical results (–) of FDVM_2 for the $0.01m$ negative rectangular wave.

Quantity	$\mathcal{C}^*(\boldsymbol{q}^0)$	$\mathcal{C}^*(\boldsymbol{q}^*)$	$C^*(\boldsymbol{q}^0, \boldsymbol{q}^*)$
h	11.9888	11.9888	0
uh	0	7.44×10^{-18}	7.44×10^{-18}
G	0	1.56×10^{-18}	1.56×10^{-18}
$\mathcal{H}$	5.8751	5.8751	5.70×10^{-6}

Table 6.1: Initial and final total amounts and the conservation error for all conserved quantities for numerical solution of FEVM_2 for the $0.01m$ negative rectangular wave.

Quantity	$\mathcal{C}^*(\boldsymbol{q}^0)$	$\mathcal{C}^*(\boldsymbol{q}^*)$	$C^*(\boldsymbol{q}^0, \boldsymbol{q}^*)$
h	11.9888	11.9888	0
uh	0	-1.19×10^{-17}	-1.19×10^{-17}
G	0	-8.05×10^{-18}	-8.05×10^{-18}
$\mathcal{H}$	5.8751	5.8751	6.27×10^{-6}

Table 6.2: Initial and final total amounts and the conservation error for all conserved quantities for numerical solution of FDVM_2 for the $0.01m$ negative rectangular wave.

6.1.2 Results for $0.03m$ Negative Rectangular Wave

The wave gauge data for the numerical and experimental results for the evolution of the $0.03m$ negative rectangular wave are displayed in Figures 6.5 and 6.6 for FEVM_2 and FDVM_2 respectively. These results are reported using the same dimensionless scales as in the original paper [55]. The completely numerically calculated conservation error C^* of all the conserved quantities are given in Tables 6.3 and 6.3 for FEVM_2 and FDVM_2 respectively.

Both methods again reproduce the overall behaviour of this experiment very well. Because the rectangular wave is deeper, this experiment provides a more rigorous test for the numerical methods. However, increasing the depth also strengthens the causes of the discrepancy between the experimental results and the numerical solutions of the Serre equations. This is evident for the amplitude and speed of the generated waves.

Since the negative rectangular wave is larger than in the previous example, the numerical methods have a larger error in conservation for all the quantities as compared to the $0.01m$ negative rectangular wave except mass; which is conserved exactly. For G and momentum these errors are around machine epsilon and can be disregarded, so that only the conservation of energy is significantly effected. Even with this larger error, all quantities are still well conserved by the numerical methods.

These results compare well with those by Zoppou et al. [15] for FDVM_2 with $\Delta x = 0.005m$, $\Delta t = 0.2\Delta t/\sqrt{g0.1}s$ and $\theta = 1$. The wave gauge data of those numerical solutions and the solutions displayed here are indistinguishable. The error in conservation in $\mathcal{H}$ is very similar as well, although in the numerical solutions displayed here the numerical grid is coarser. This is because the limiting parameter $\theta = 1$ diffuses the discontinuous jump, leading to poorer conservation of $\mathcal{H}$ [14] than expected given the higher resolution of the grid.

The conservation of $\mathcal{H}$ is difficult for numerical methods solving steep gradient problems [14]. More so for this simulation where two steep gradients interact with one another over short time spans. By increasing the resolution of the numerical method the conservation error decreases as demonstrated for the analytic solutions. However, the results for the wave gauge data will be indistinguishable from the results presented here and the given resolution solutions are sufficient.

These experiments have been replicated equally well by the numerical methods, and given the resolution and error in conservation and the extensive study summarised in Chapter 2; these results demonstrate the accuracy of the numerical

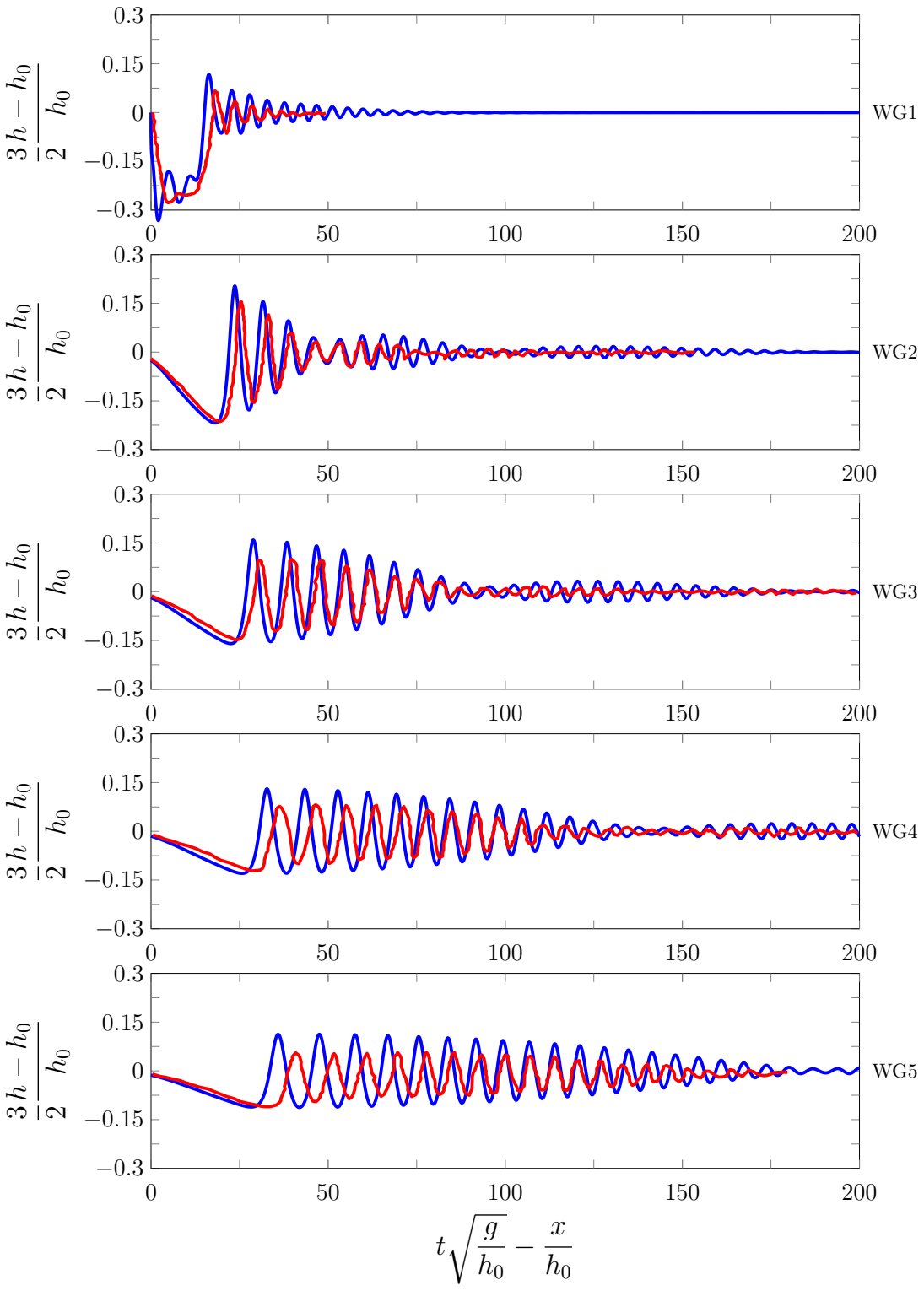

Figure 6.5: Time series of the experimental wave gauge data (–) and numerical results (–) of FEVM$_2$ for the $0.03m$ negative rectangular wave.

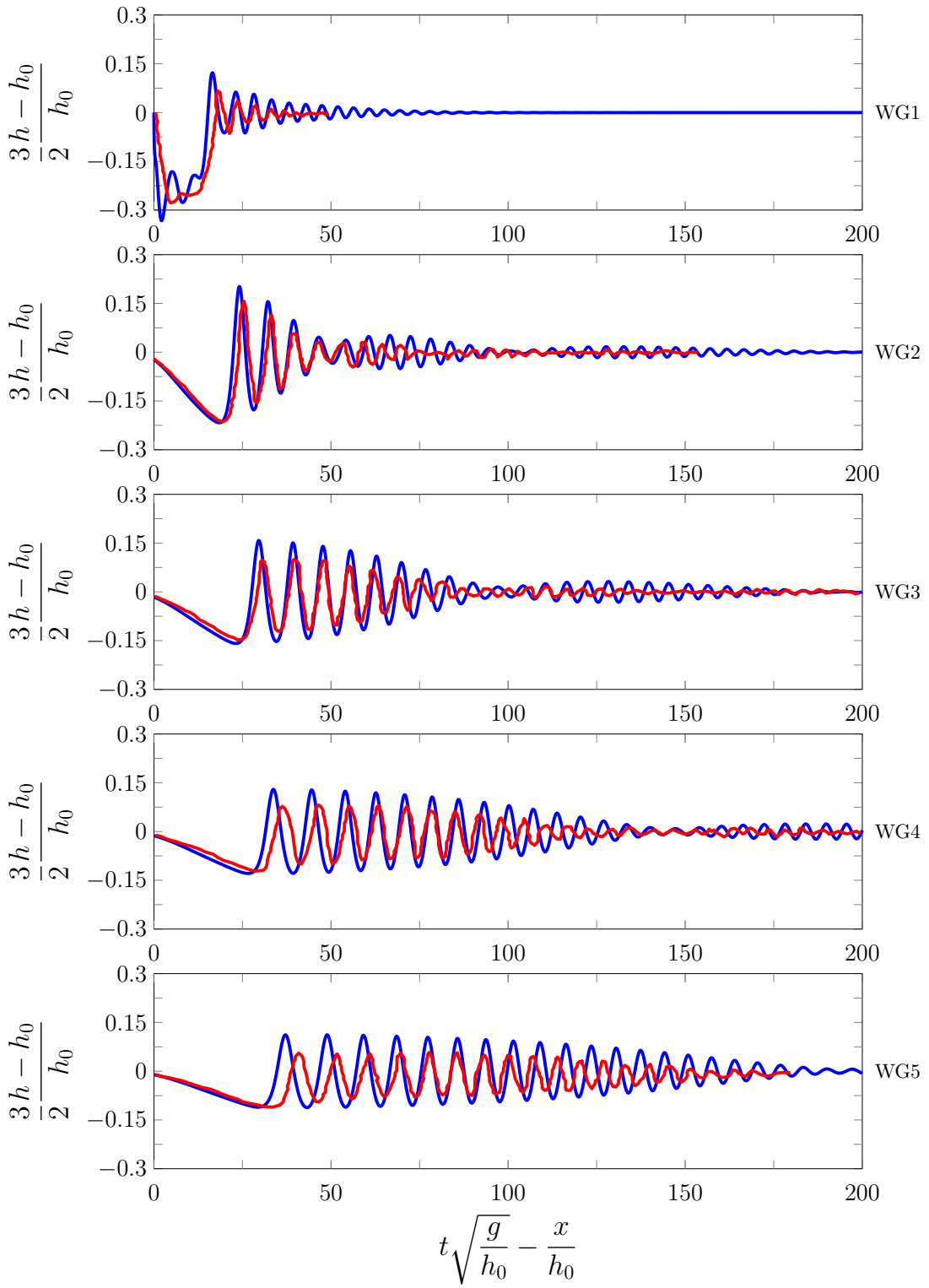

Figure 6.6: Time series of the experimental wave gauge data (–) and numerical results (–) of FDVM$_2$ for the $0.03m$ negative rectangular wave.

Quantity	$\mathcal{C}^*(\boldsymbol{q}^0)$	$\mathcal{C}^*(\boldsymbol{q}^*)$	$C^*(\boldsymbol{q}^0, \boldsymbol{q}^*)$
h	11.9644	11.9644	0
uh	0	-7.75×10^{-17}	-7.75×10^{-17}
G	0	-3.33×10^{-16}	-3.33×10^{-16}
$\mathcal{H}$	5.8560	5.8552	1.24×10^{-4}

Table 6.3: Initial and final total amounts and the conservation error for all conserved quantities for numerical solution of FEVM_2 for the $0.03m$ negative rectangular wave.

Quantity	$\mathcal{C}^*(\boldsymbol{q}^0)$	$\mathcal{C}^*(\boldsymbol{q}^*)$	$C^*(\boldsymbol{q}^0, \boldsymbol{q}^*)$
h	11.9644	11.9644	0
uh	0	-9.09×10^{-17}	-9.09×10^{-17}
G	0	-1.16×10^{-16}	-1.16×10^{-16}
$\mathcal{H}$	5.8560	5.8552	1.30×10^{-4}

Table 6.4: Initial and final total amounts and the conservation error for all conserved quantities for numerical solution of FDVM_2 for the $0.03m$ negative rectangular wave.

methods in the presence of steep gradients in the free surface.

6.2 Periodic Waves Over A Submerged Bar

Beji and Battjes conducted a series of experiments investigating the effect of submerged bars on the propagation of periodic waves [56, 57]. The behaviour of these experiments were mainly driven by the dispersion properties of the waves and their interaction with variations in bathymetry. Therefore, these experiments serve as a benchmark for the ability of the numerical schemes to accurately model the interaction of variable bathymetry and dispersive waves. For our purposes we will focus on the monochromatic wave experiments of Beji and Battjes [57].

The experiments of Beji and Battjes [57] were conducted in a wave tank $37.7m$

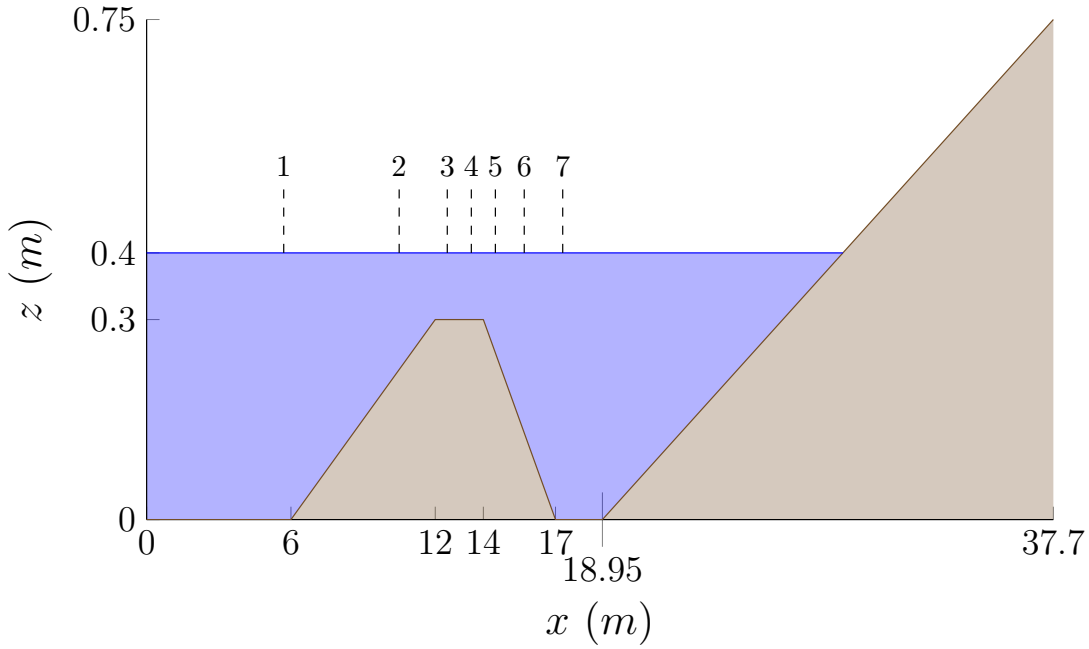

Figure 6.7: Diagram showing a longitudinal section of the wave tank for the periodic waves over a submerged bar experiments with the water (▫), the bed (▫) and the numbered wave gauge marked.

long, $0.8m$ wide and $0.75m$ high. A diagram of the longitudinal section of the wave tank is given in Figure 6.7. There are seven wave gauges at the following locations; $5.7m$, $10.5m$, $12.5m$, $13.5m$, $14.5m$, $15.7m$ and $17.3m$. Waves are generated from a piston-type wave maker located at $0m$ and travel on the initially still water $0.4m$ deep to the right, over the submerged trapezoidal bar and are absorbed by a sloping beach.

Two monochromatic non-breaking wave experiments were performed. A low frequency one with a wavelength $\lambda \approx 3.69m$ and a period of $T = 2s$, and a high frequency one with $\lambda \approx 2.05m$ and a period of $T = 1.25s$. Both experiments had a wave amplitude of $0.01m$ and so both had the same small non-linearity parameter $\epsilon = 0.01/0.4 = 0.025$.

For the numerical solutions the spatial domain was $[5.7m, 150m]$ with $\Delta x = 0.1/2^4 m \approx 0.0063m$ and $\Delta t = Sp/2^5 s \approx 0.0012s$ where $Sp = 0.039s$ is the experimental sampling period. These Δx and Δt values satisfy the CFL condition, (3.22). In our numerical experiments only the submerged trapezoidal bar is present, and the sloping beach is replaced with a very long horizontal bed that ensures that we do not observe any effects from the Dirichlet boundary conditions at the downstream boundary.

To simulate the incoming waves at the upstream boundary we used the first wave gauge as our left boundary condition together with linear extrapolation to calculate the other required h values in the left ghost cell. The velocity boundary conditions were calculated from the height values in the same way as Beji and Battjes [57] using

$$u(x,t) = \sqrt{gh_0}\,\frac{h(x,t)-h_0}{h(x,t)}.$$

Finally the boundary conditions for G were calculated using the boundary values for h and u.

We shall now present our numerical results for the low and high frequency experiments.

6.2.1 Low Frequency Results

A comparison of the wave heights η of the experimental and numerical results are located in Figures 6.8 and 6.9 for FEVM_2 and Figures 6.10 and 6.11 for FDVM_2. These numerical schemes produce indistinguishable results for all wave gauges and so this benchmark does not help us discriminate between these two methods.

These results demonstrate the ability of these numerical methods to reproduce the experimental results, particularly for wave gauge 1 to 5 where the agreement between experimental and numerical results is best. Results at these gauges validate the numerical schemes for simulating shoaling of dispersive waves as these wave gauges are all located on the windward side of the submerged bar where shoaling occurs in the experiment.

The numerical results for wave gauges 6 and 7 on the leeward side capture some of the wave behaviour but their agreement with the experiments results is much worse. The inadequacy of the numerical results here appears to be due to the discrepancy between the dispersion properties of the Serre equations and actual water waves [57, 58].

The dispersion terms in the Serre equations are vital to recreating the experimental results for wave gauges 2 to 5, as non-dispersive equations such as the SWWE are not capable of accurately simulating this experiment [59].

6.2.2 High Frequency Results

The wave heights of the experimental and numerical results are given in Figures 6.12 and 6.13 for FEVM_2. While the results for FDVM_2 are given in Figures 6.14

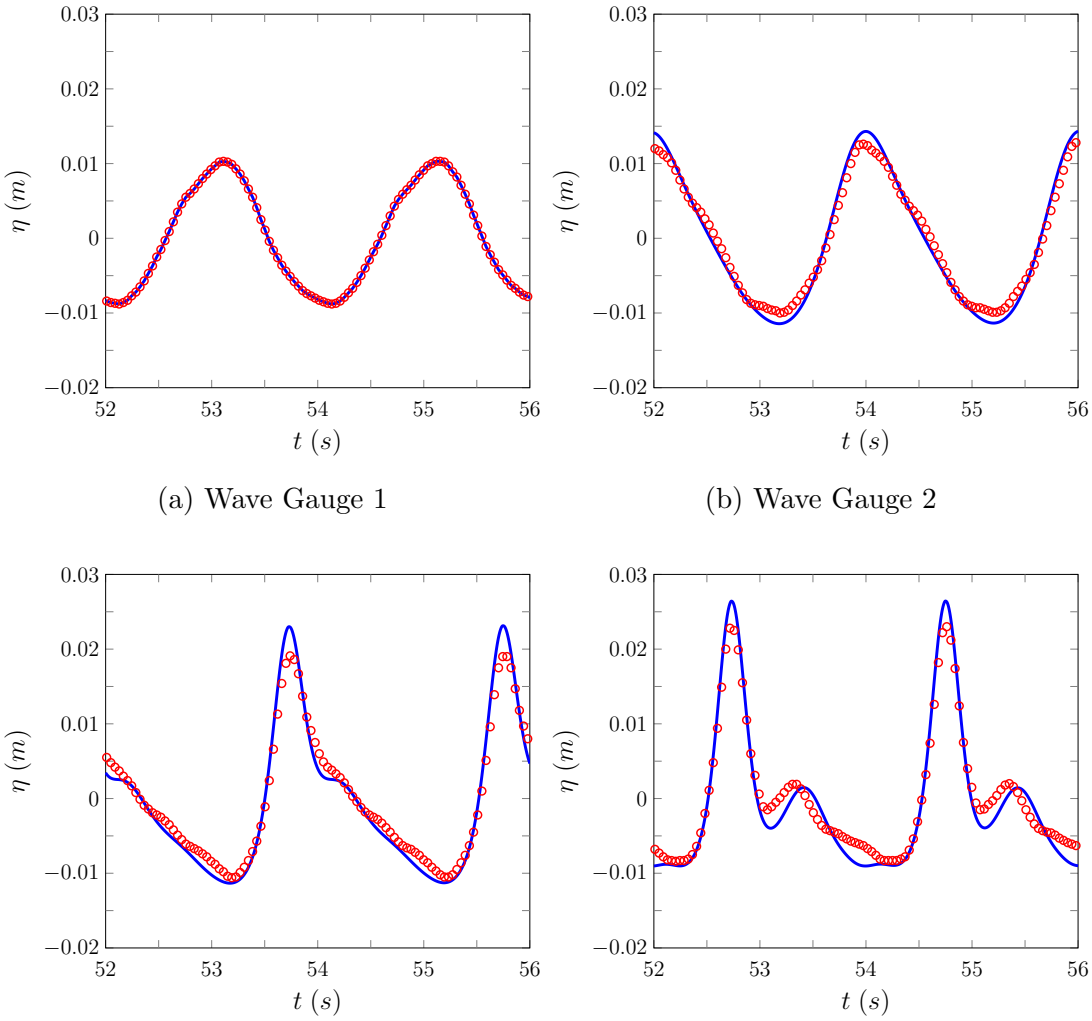

(a) Wave Gauge 1

(b) Wave Gauge 2

(c) Wave Gauge 3

(d) Wave Gauge 4

Figure 6.8: Time series of the wave heights η of the numerical results of FEVM_2 (−) and the experimental results (○) for wave gauges 1 - 4 for the low frequency experiment.

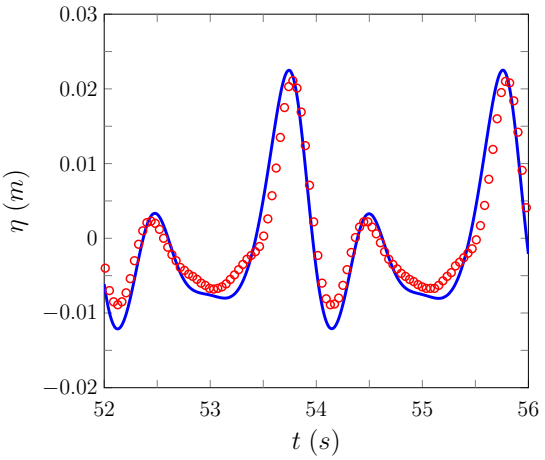

(a) Wave Gauge 5

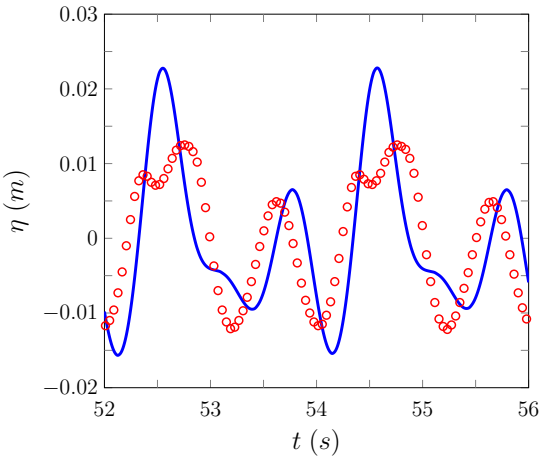

(b) Wave Gauge 6

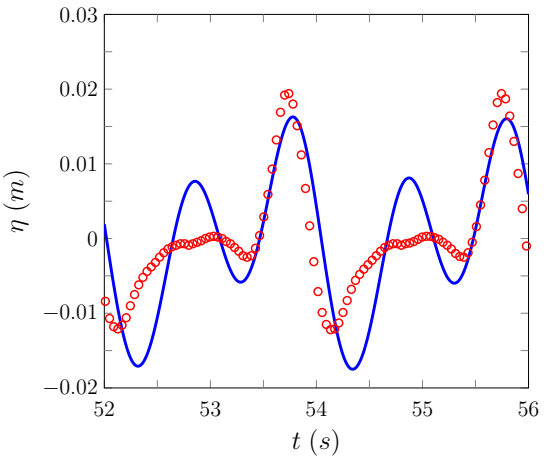

(c) Wave Gauge 7

Figure 6.9: Time series of the wave heights η of the numerical results of FEVM_2 (−) and the experimental results (○) for wave gauges 5 - 7 for the low frequency experiment.

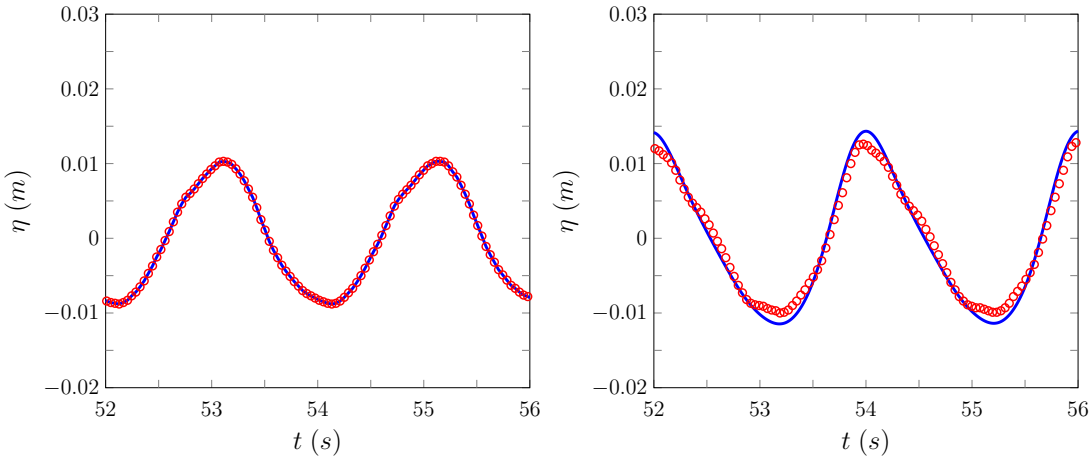

(a) Wave Gauge 1

(b) Wave Gauge 2

(c) Wave Gauge 3

(d) Wave Gauge 4

Figure 6.10: Time series of the wave heights η of the numerical results of $FDVM_2$ (−) and the experimental results (○) for wave gauges 1 - 4 for the low frequency experiment.

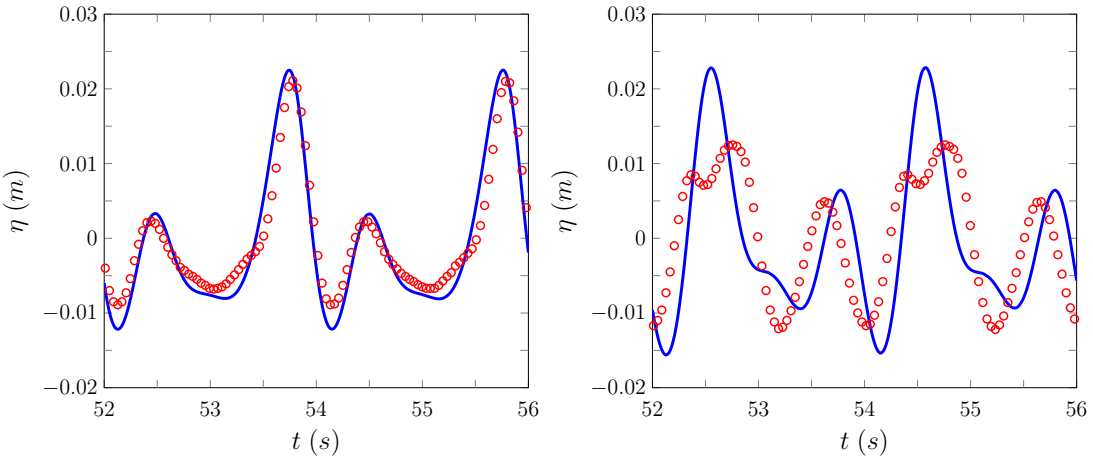

(a) Wave Gauge 5

(b) Wave Gauge 6

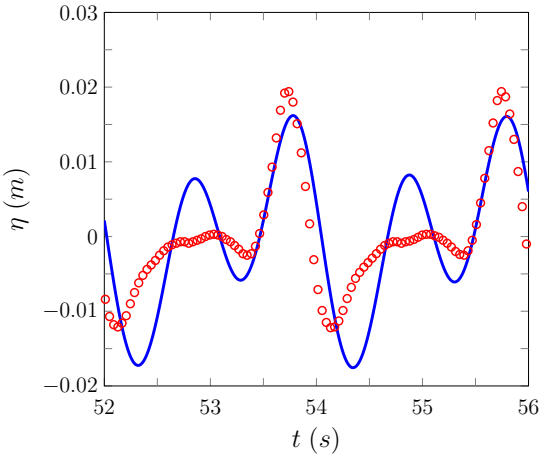

(c) Wave Gauge 7

Figure 6.11: Time series of the wave heights η of the numerical results of $FDVM_2$ (−) and the experimental results (○) for wave gauges 5 - 7 for the low frequency experiment.

and 6.15. As for the low frequency experiment FEVM_2 and FDVM_2 produce indistinguishable results for all wave gauges at this scale and so this benchmark does not discriminate between these two methods.

As in the low frequency experiment we observe that the numerical results perform well on the windward side of the slope for wave gauges 1 to 4 but perform poorly for the leeward side of the slope for wave gauges 5 to 7. With the high frequency experiment we see the divergence between the numerical and experimental results earlier than the low frequency experiment, so that now wave gauge 5 which is on the leeward side exhibits a significant difference between the numerical and experimental results. As in the low frequency example this is caused by the difference in the dispersion relations of the Serre equations and the linear theory for water waves [57, 58]. Because the difference between the dispersion relation of the Serre equations and water waves is largest for higher frequency and therefore for shorter waves [21] the earlier divergence between experimental and numerical results is not surprising.

These numerical results for the FDVM_2 and FEVM_2 agree well with other numerical results for weakly dispersive equations without improved dispersion properties for the simulation of periodic waves over a submerged bar in the literature [25, 57, 58, 60]. Therefore, without changing the underlying partial differential equations, our numerical methods perform as well as other numerical schemes in the literature at recreating the experimental results of Beji and Battjes [57].

6.3 Solitary Wave Over a Fringing Reef

To study the evolution of waves on fringing reefs a series of experiments were conducted by Roeber [61]. These experiments were performed in a wave tank $3.66m$ wide, $83.7m$ long and $4.57m$ high with a removable bed that allowed for the wide range of experiments reported by Roeber [61]. We have computationally modelled the experiment with the bathymetry displayed in Figure 6.16, where a solitary wave is generated from the wave maker at $0m$ and is recorded at the wave gauges $17.6m$, $28.6m$, $35.9m$, $40.6m$, $44.3m$, $46.1m$, $48.2m$, $50.4m$, $54.4m$, $58.0m$, $61.7m$, $65.4m$, $72.7m$ and $80.0m$ downstream of the wave maker.

This experiment investigates the behaviour of a wave with high non-linearity $\epsilon \approx 1.23/2.46 = 0.5$ as it shoals over a linear bed into a very shallow body of water. Given the high non-linearity of this wave, it is not surprising that as it shoals it becomes a plunging breaker by $t \approx 32s$ with an elliptical air cavity

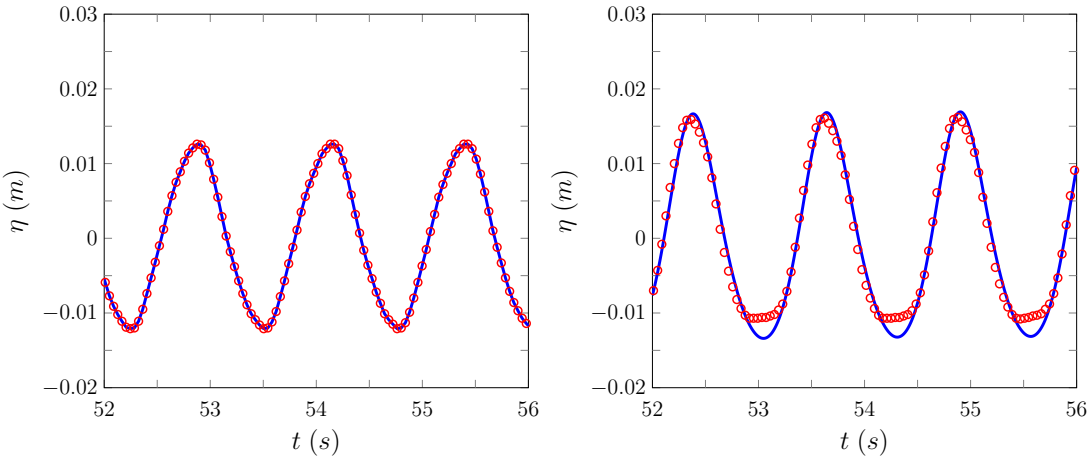

(a) Wave Gauge 1

(b) Wave Gauge 2

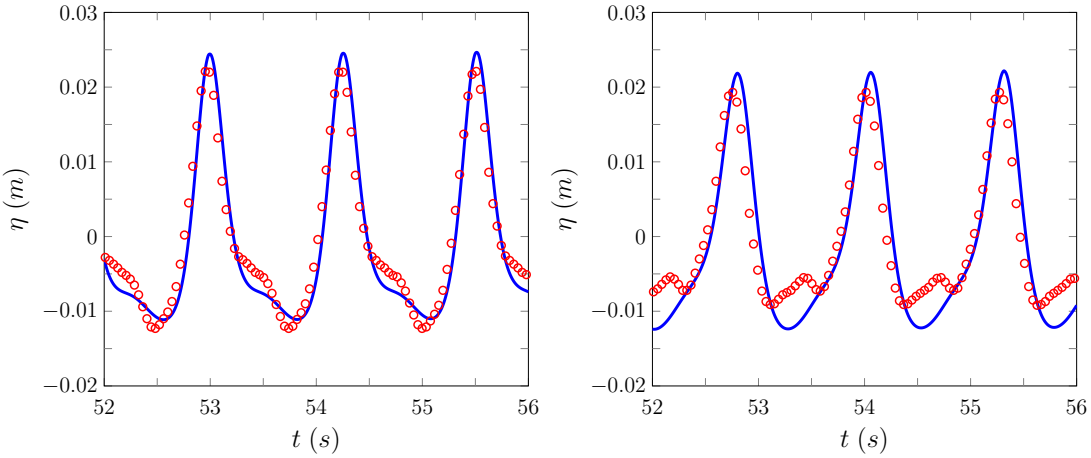

(c) Wave Gauge 3

(d) Wave Gauge 4

Figure 6.12: Time series of the wave heights η of the numerical results of FEVM_2 (–) and the experimental results (○) for wave gauges 1 - 4 for the low frequency experiment.

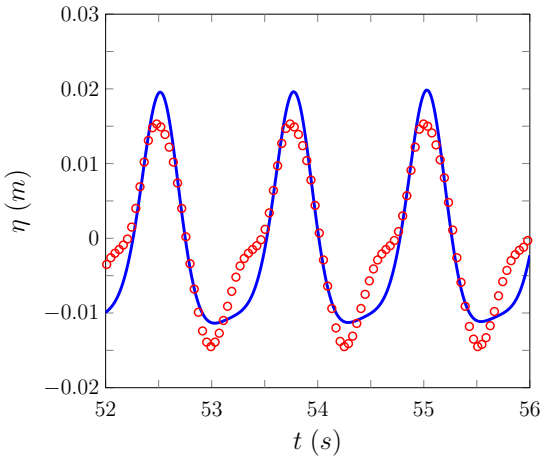

(a) Wave Gauge 5

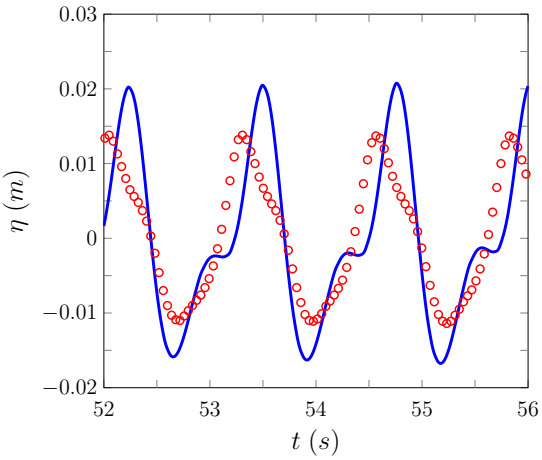

(b) Wave Gauge 6

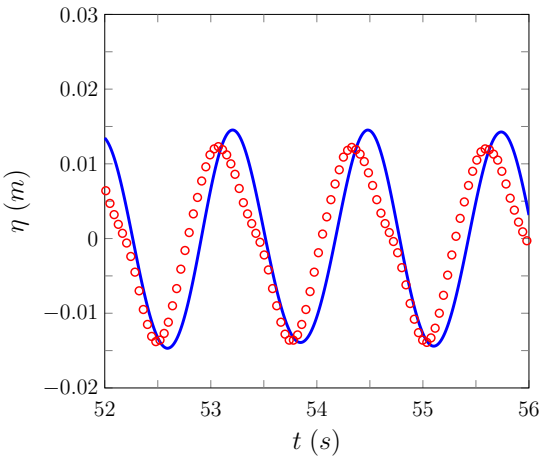

(c) Wave Gauge 7

Figure 6.13: Time series of the wave heights η of the numerical results of FEVM_2 (−) and the experimental results (○) for wave gauges 5 - 7 for the high frequency experiment.

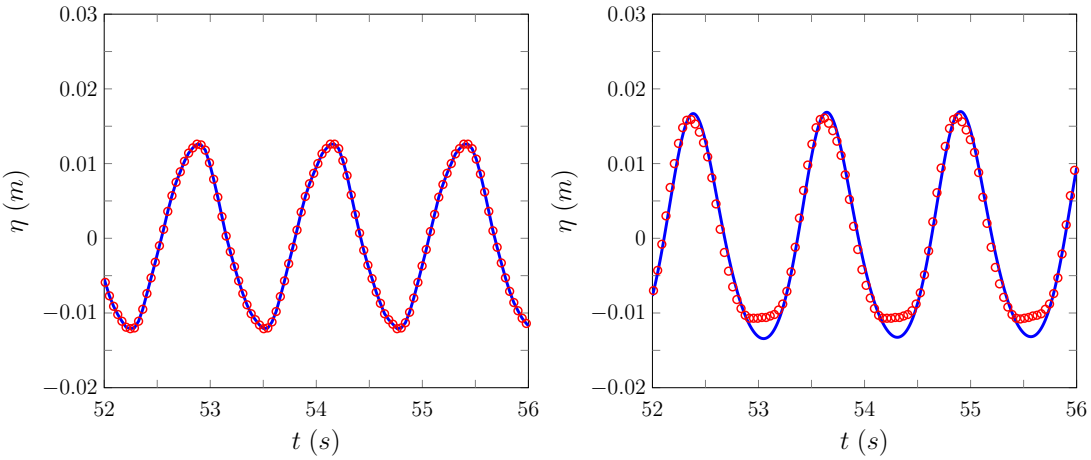

(a) Wave Gauge 1

(b) Wave Gauge 2

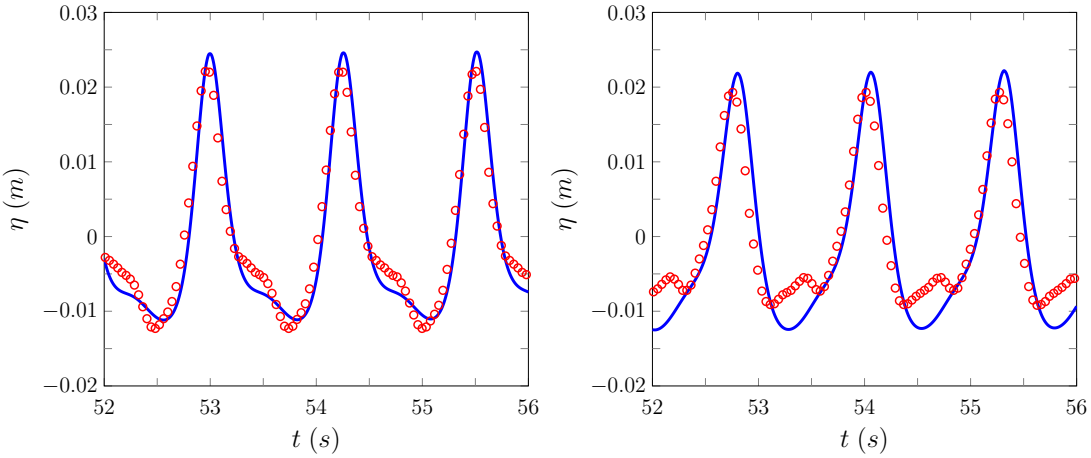

(c) Wave Gauge 3

(d) Wave Gauge 4

Figure 6.14: Time series of the wave heights η of the numerical results of $FDVM_2$ (–) and the experimental results (○) for wave gauges 1 - 4 for the high frequency experiment.

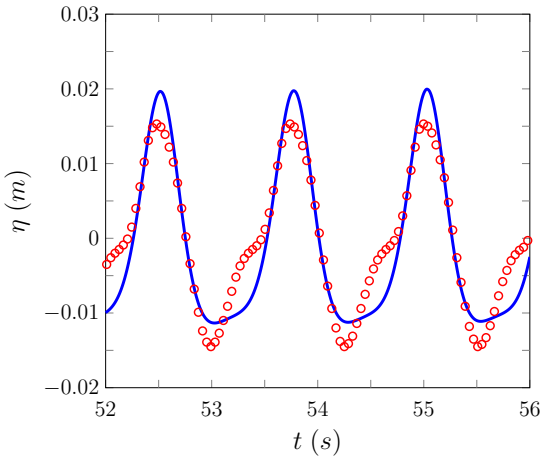

(a) Wave Gauge 5

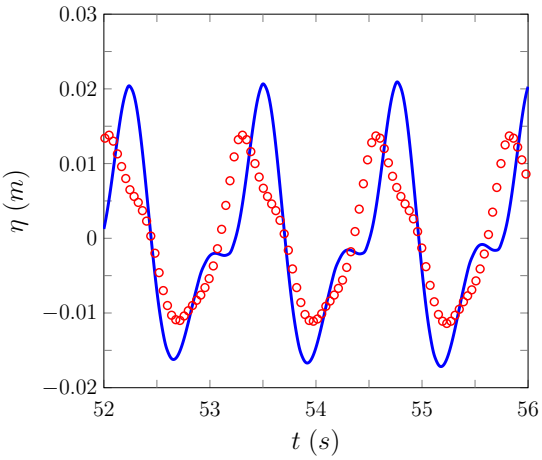

(b) Wave Gauge 6

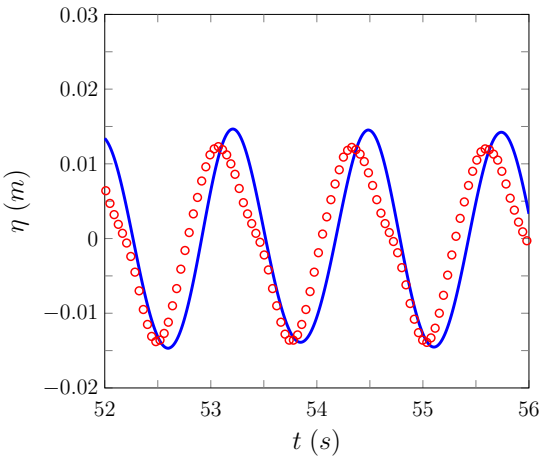

(c) Wave Gauge 7

Figure 6.15: Time series of the wave heights η of the numerical results of FDVM$_2$ (−) and the experimental results (○) for wave gauges 5 - 7 for the high frequency experiment.

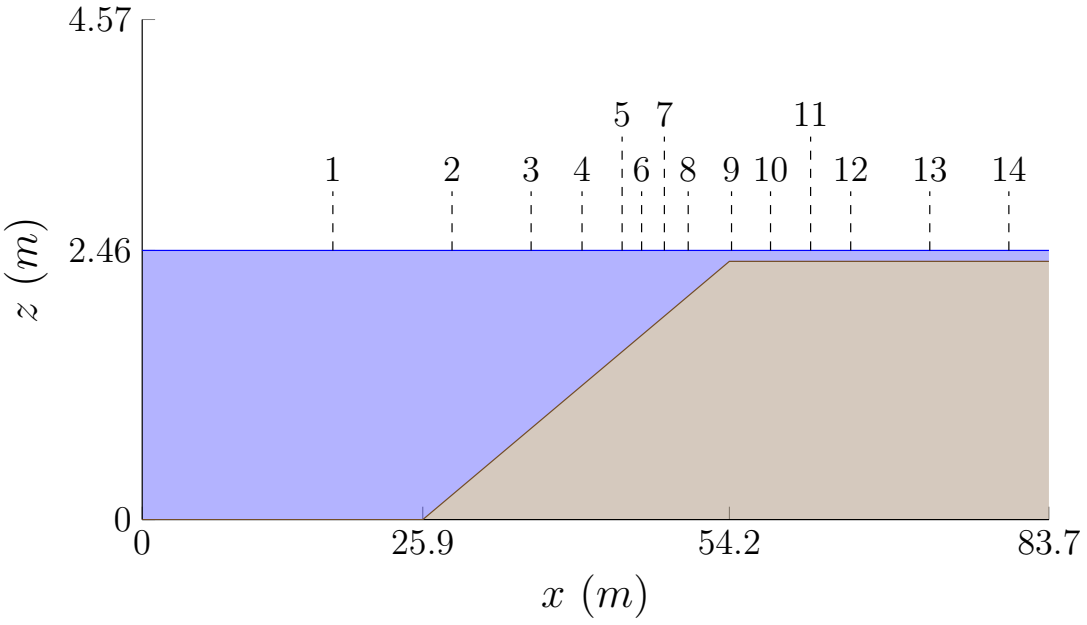

Figure 6.16: Diagram showing a longitudinal section of the wave tank for the solitary wave over a fringing reef experiment with the water (■), the bed (■) and the numbered wave gauge marked.

observed at $t \approx 33s$ [61]. As with other depth averaged equations, the Serre equations are only appropriate up to breaking waves so this experiment is not an entirely appropriate test of the numerical methods, particularly after $t = 32s$.

This experiment was numerically modelled on the domain $[17.6m, 400m]$ and was run until $t = 60s$ after which the reflections from the downstream end of the tank become significant in the experiment. The beginning of the domain was chosen so that wave gauge 1 could be used as the left boundary conditions, where the technique for the boundary condition in Section 6.2 was employed. The spatial resolution was $\Delta x = 0.025m$ and the temporal resolution was $\Delta t = Sp/8s = 0.0025$ where $Sp = 0.02s$ was the sampling period of the wave gauges, these spatial and temporal resolutions satisfy the CFL condition (3.22). The right edge of the domain used Dirichlet boundary conditions, since the domain was large no effects from the downstream boundary were observed throughout the numerical simulation.

The wave gauge results comparing the numerical and experimental data are displayed in Figures 6.17, 6.18 and 6.19 for FEVM_2 and 6.20 and 6.21 for FDVM_2.

Both methods accurately reproduce the shoaling of the solitary wave, partic-

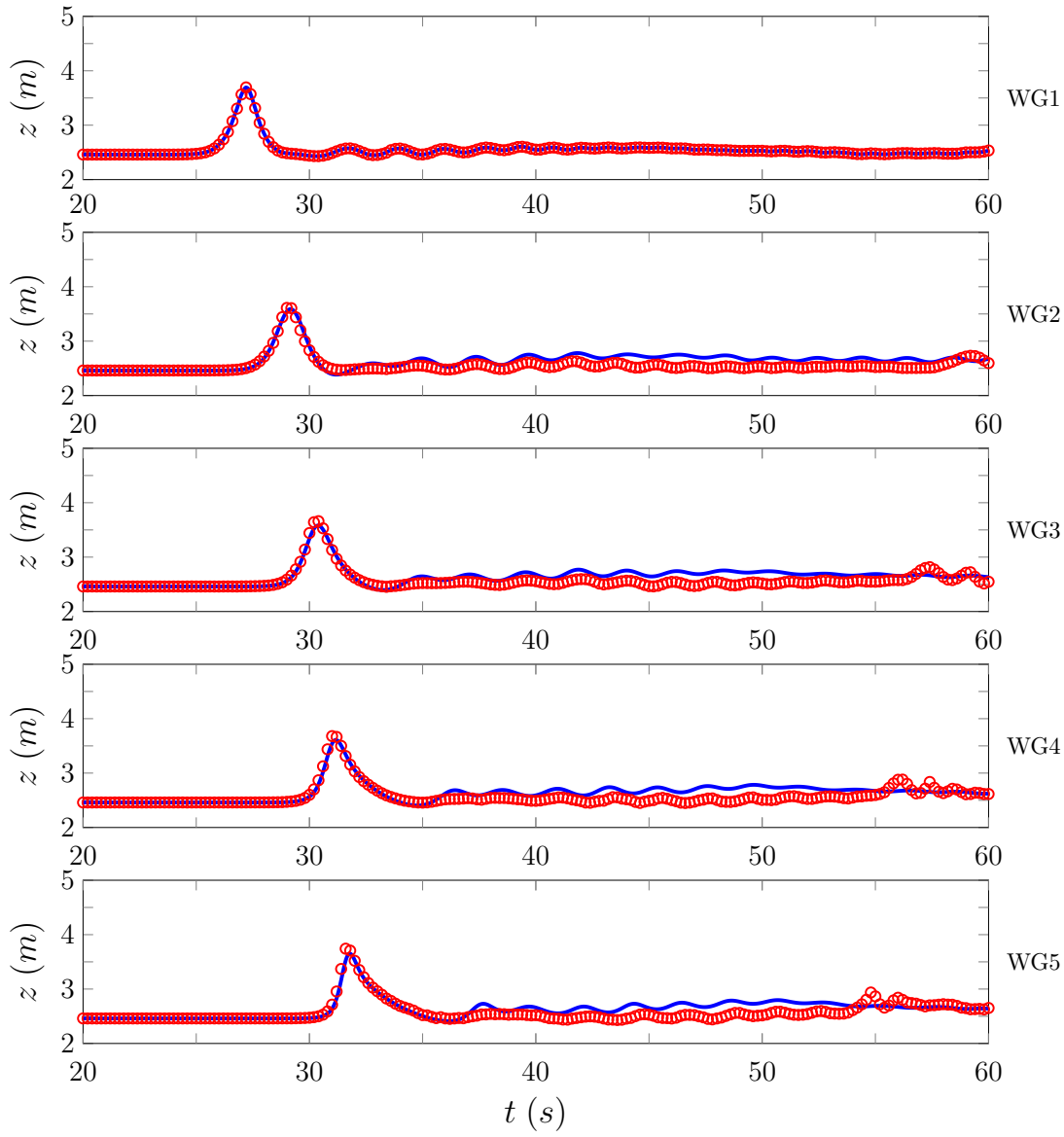

Figure 6.17: Time series of the experimental (○) and numerical (—) wave gauge data produced by FEVM_2 for gauges 1 to 5.

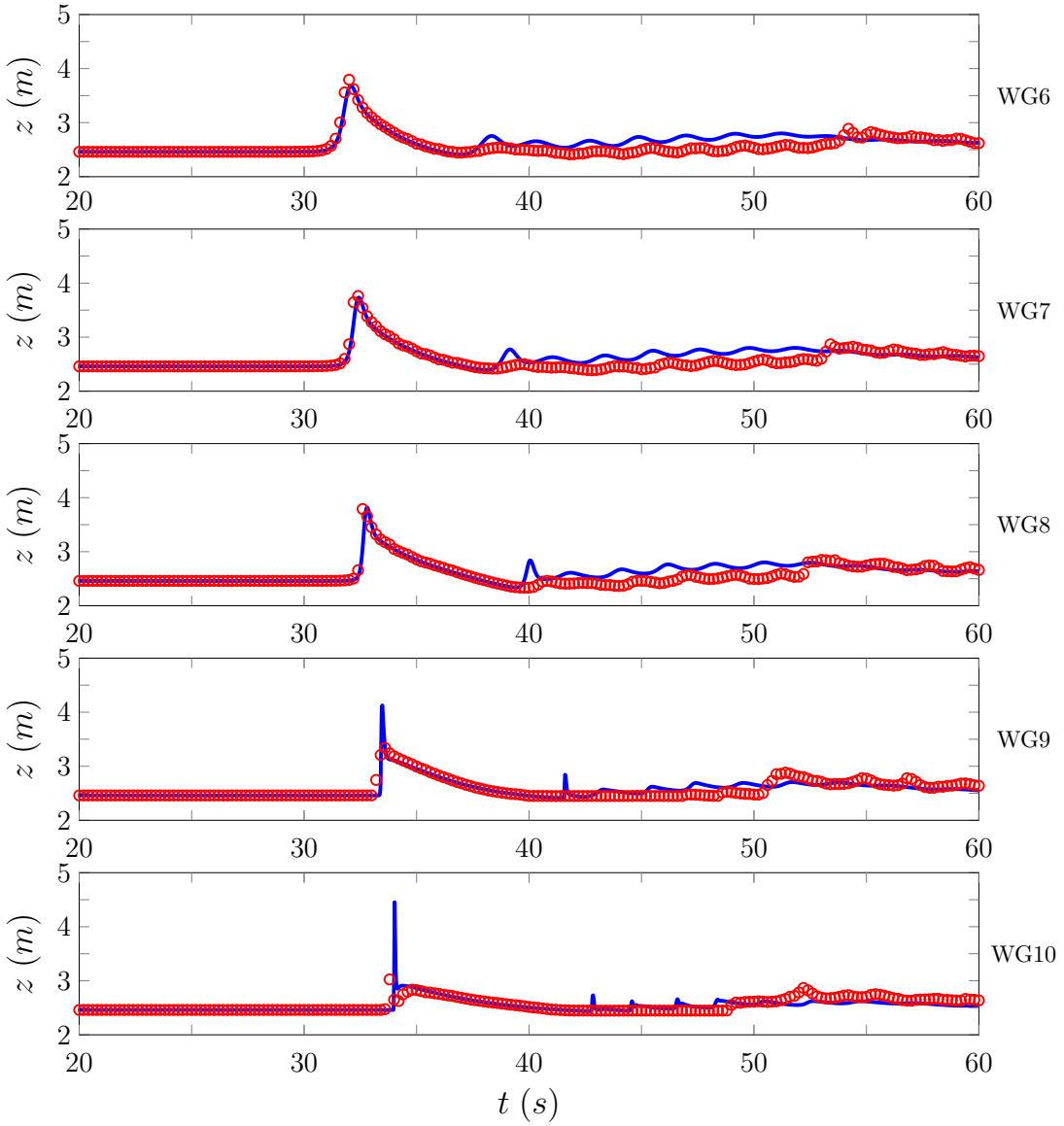

Figure 6.18: Time series of the experimental (○) and numerical (–) wave gauge data produced by FEVM$_2$ for gauges 6 to 10.

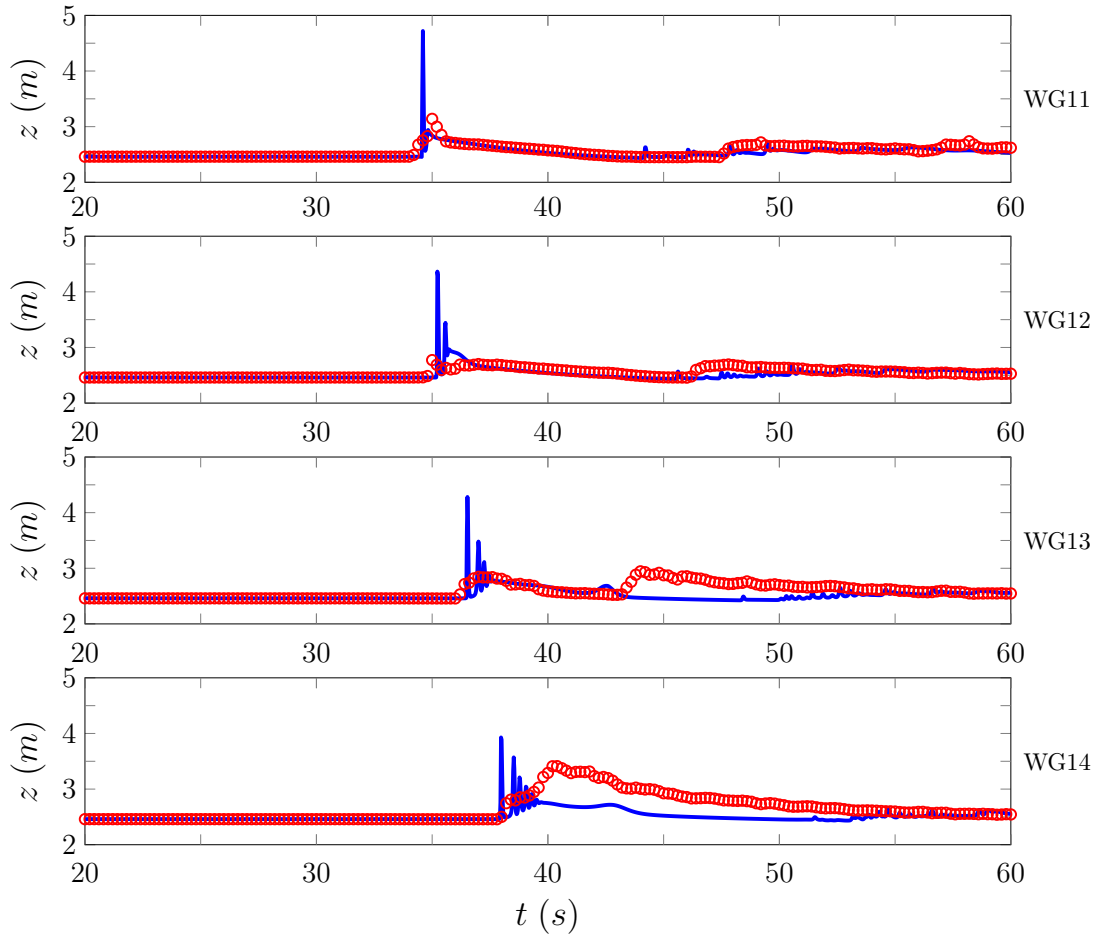

Figure 6.19: Time series of the experimental (○) and numerical (—) wave gauge data produced by FEVM_2 for gauges 11 to 14.

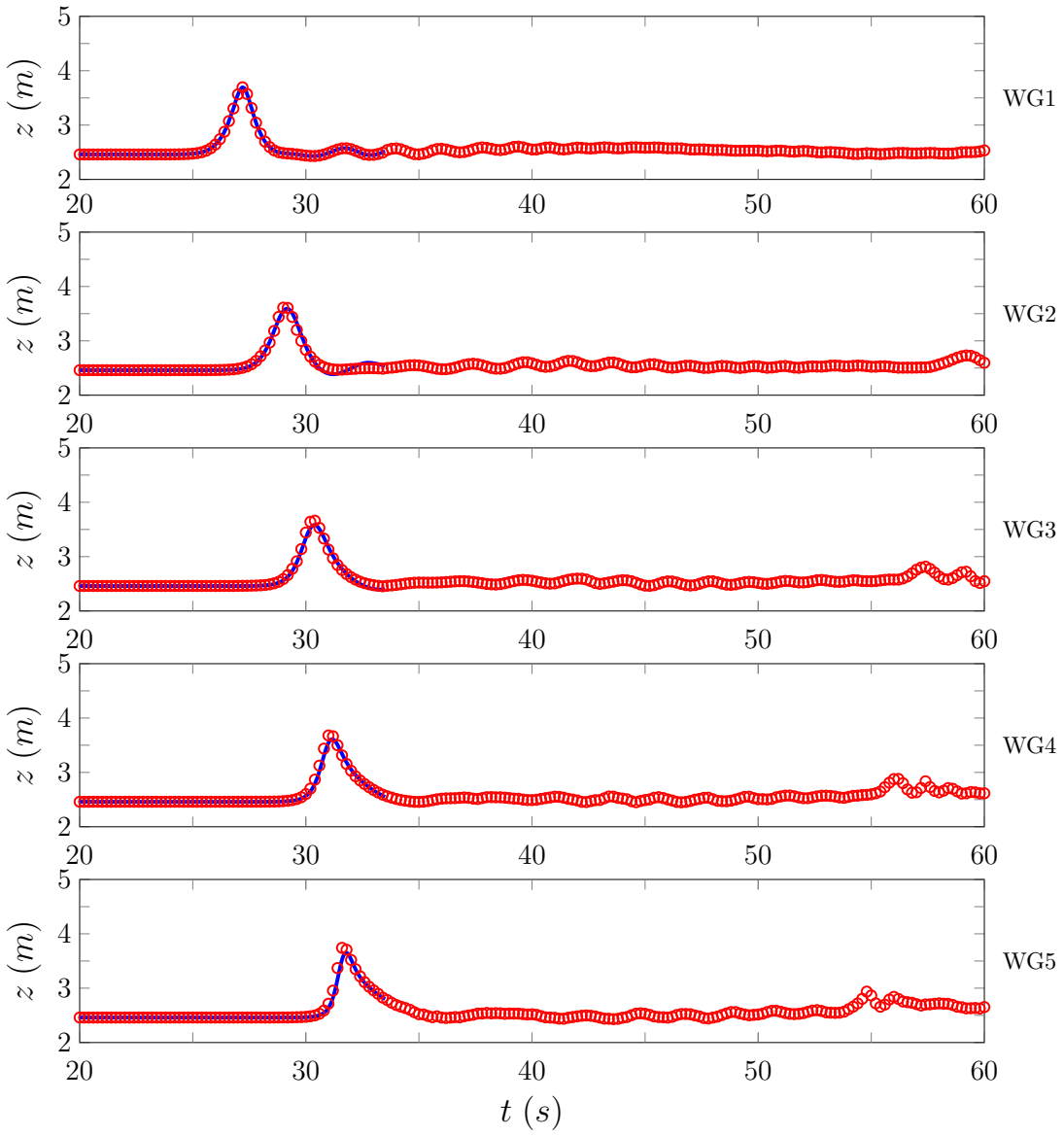

Figure 6.20: Time series of the experimental (○) and numerical (–) wave gauge data produced by $FDVM_2$ for gauges 1 to 7.

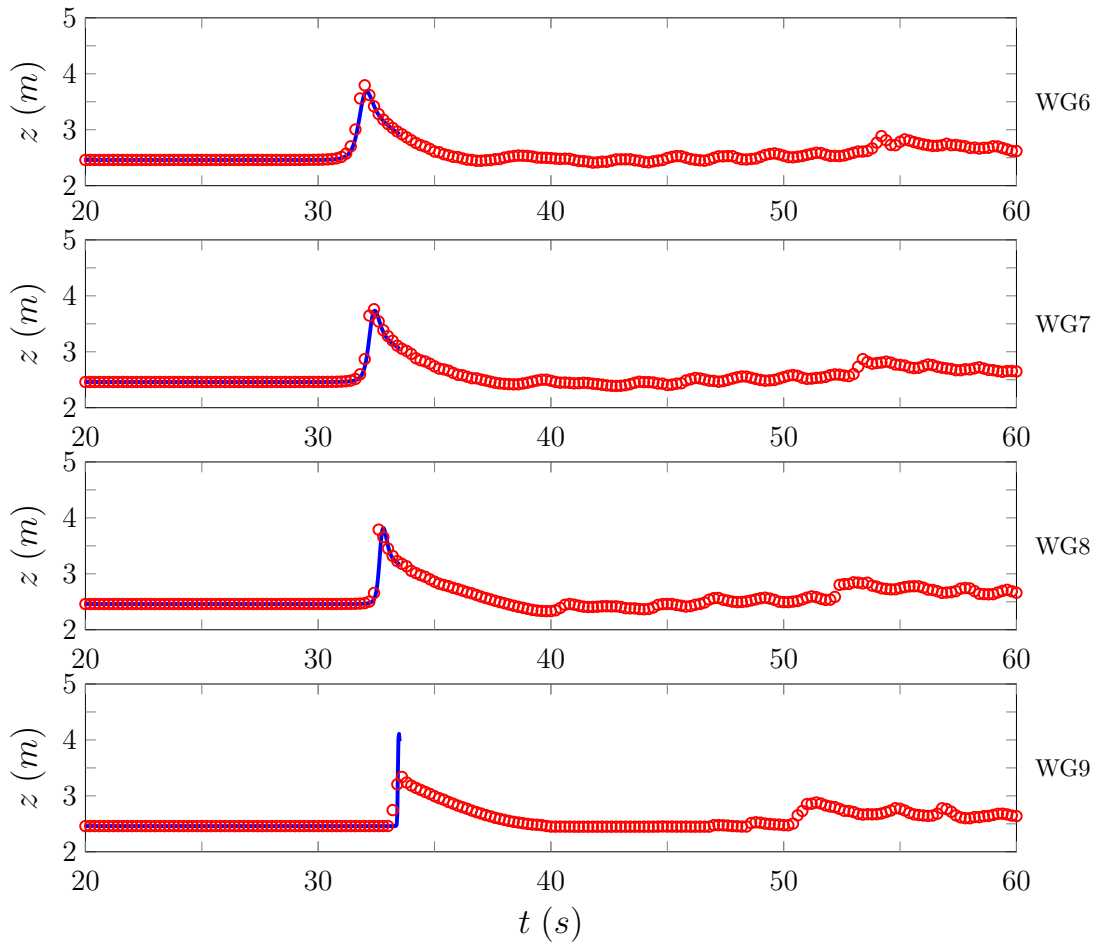

Figure 6.21: Time series of the experimental (○) and numerical (–) wave gauge data produced by $FDVM_2$ for gauges 6 to 9.

ularly in wave gauges 1 through 8 which record the wave before breaking begins. The behaviour of the trailing waves is not as well replicated, with the numerical solutions overestimating their amplitude and speed as in the previous experiments. The reflected wave can also be observed in the wave gauges and since the numerical simulation did not have reflective boundaries these waves are not replicated in their numerical solutions.

When breaking begins the numerical solutions perform much worse as expected; most notably FDVM_2 becomes unstable and the solution blows up. Because of this the numerical solution of FDVM_2 was only plotted until $t = 34s$. The instability is caused by the appearance of a very steep gradient with a large jump in the water depth compared to the depth of water that surrounds it as the wave breaks. The FEVM_2 method does not suffer from these instability issues, but due to the limitations of the Serre equations does produce a dispersive wave train with amplitudes far exceeding the observed amplitudes of the experiment.

Given the limitations of the underlying Serre equations the results for FEVM_2 are robust and accurately model the shoaling of the solitary wave. However, these results indicate the need for more accurate handling of breaking waves to be able to accurately model some physical situations.

6.4 Run-up Experiment

To study the run-up of incoming waves on linear beaches a series of experiments were conducted by Synolakis [62]. These experiments consisted of a number of run-up events for a wide array of breaking and non-breaking waves where snapshots of the entire water surface were taken at certain times. These experiments were all performed on the beach profile depicted in Figure 6.22, where all the quantities are non-dimensionalised [62]. To denote that a quantity is non-dimensionalised we use with the prime symbol. To assess the computational models we recreated one of these experiments, which captured the run-up of a non-breaking solitary wave with a non-linearity parameter of $\epsilon = 0.0185$.

This experiment allows us to compare the inundation behaviour of our numerical methods with experimental results. For this experiment the effect of dispersion on the run-up behaviour is minimal, and there is good agreement between numerical solutions of the SWWE and this particular experiment [63]. Therefore, the effect of the extra dispersive terms included by the Serre equations on the inundation process is not well tested by this experiment. Importantly, this

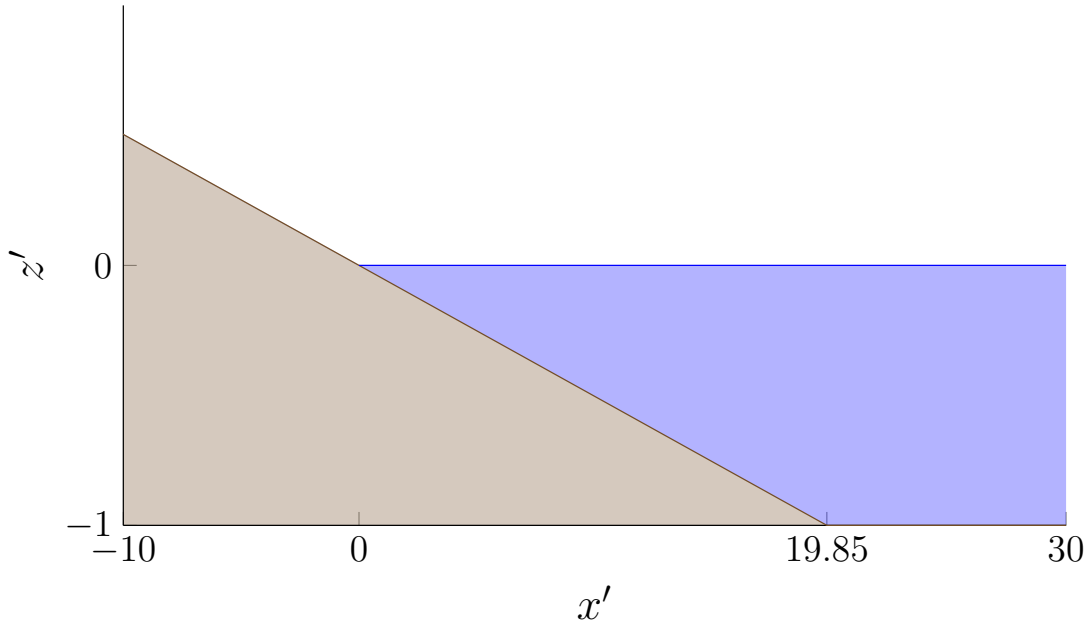

Figure 6.22: Diagram showing a longitudinal section of the wave tank for run-up experiment with the water (■), the bed (■) and the numbered wave gauge marked where the coordinates have been non-dimensionalised [62].

experiment demonstrates the methods robustness during the wetting and drying of the bed.

The numerical experiments used the non-dimensionalised quantities reported by Synolakis [62] to reproduce the experiment. The spatial domain was $x' \in [-30, 150]$ with a resolution of $\Delta x = 0.05$ and was run until $t' = 70$ with the CFL condition (3.22) satisfied by setting $\Delta t = 0.1\Delta x$. The spatial reconstruction used the input parameter $\theta = 1.2$ and acceleration due to gravity $g = 1$ was chosen to match the non-dimensionalisation.

The non-dimensionalised water surface data is given at the various times in Figure 6.24 for FDVM_2 and 6.23 for FEVM_2. The error in conservation of h and $\mathcal{H}$ as measured by C^* are given in Tables 6.5 and 6.6 for FEVM_2 and FDVM_2 respectively.

The results for FEVM_2 and FDVM_2 are indistinguishable, replicating the incoming wave properties and the maximum run-up well. The experimental wave appears to be more skewed towards the shoreline, but this shape difference has all but disappeared as the wave begins to inundate the shore. The only other noticeable difference is that the numerical solutions appear to run-down further than the experimental results. The observed larger run-down is likely caused by

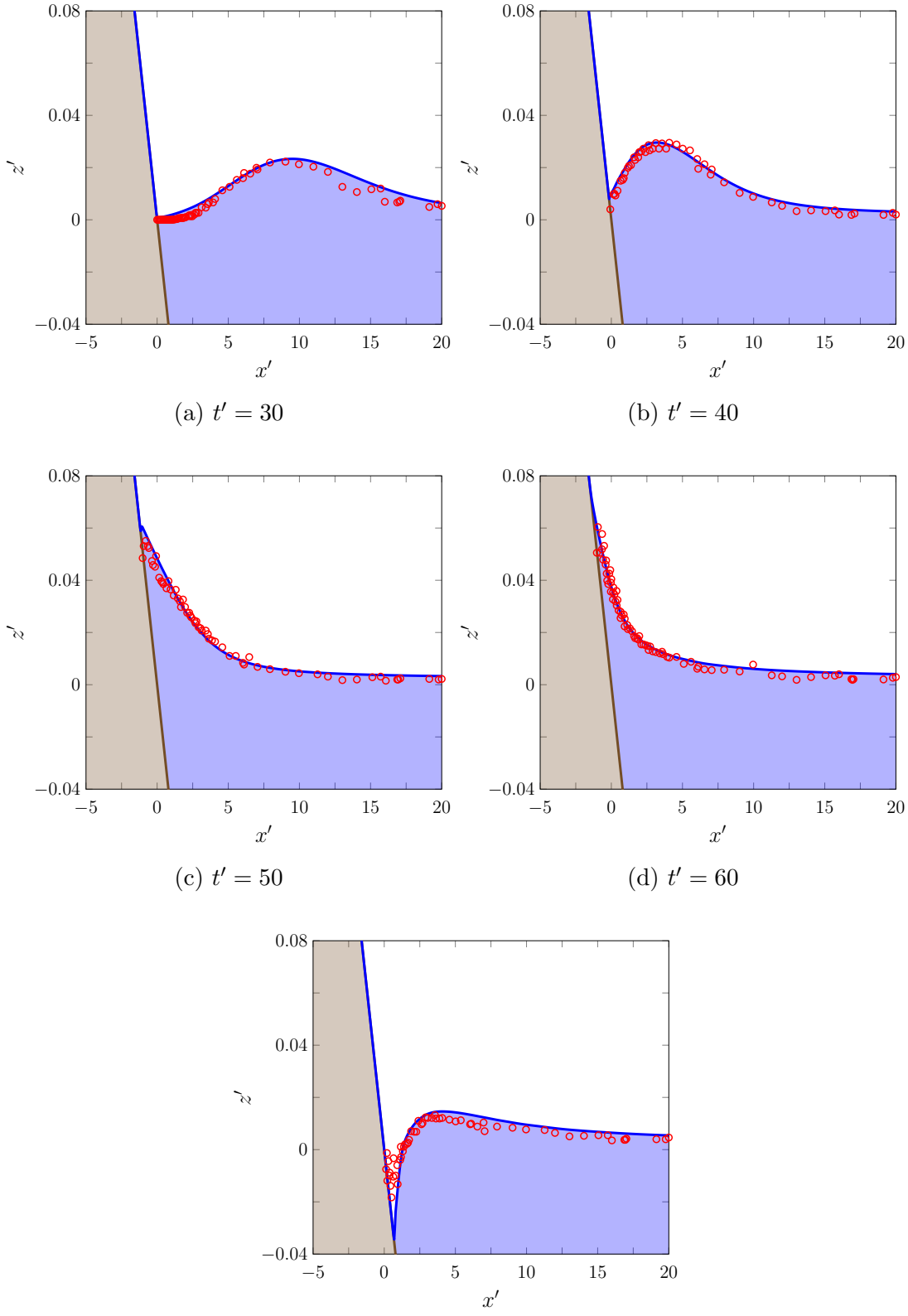

(a) $t' = 30$ (b) $t' = 40$

(c) $t' = 50$ (d) $t' = 60$

(e) $t' = 70$

Figure 6.23: A comparison of the water surface profiles $w(x', t')$ for the experiment (○) and the numerical solution (□) produced by FEVM$_2$ over the bed (□) at various times.

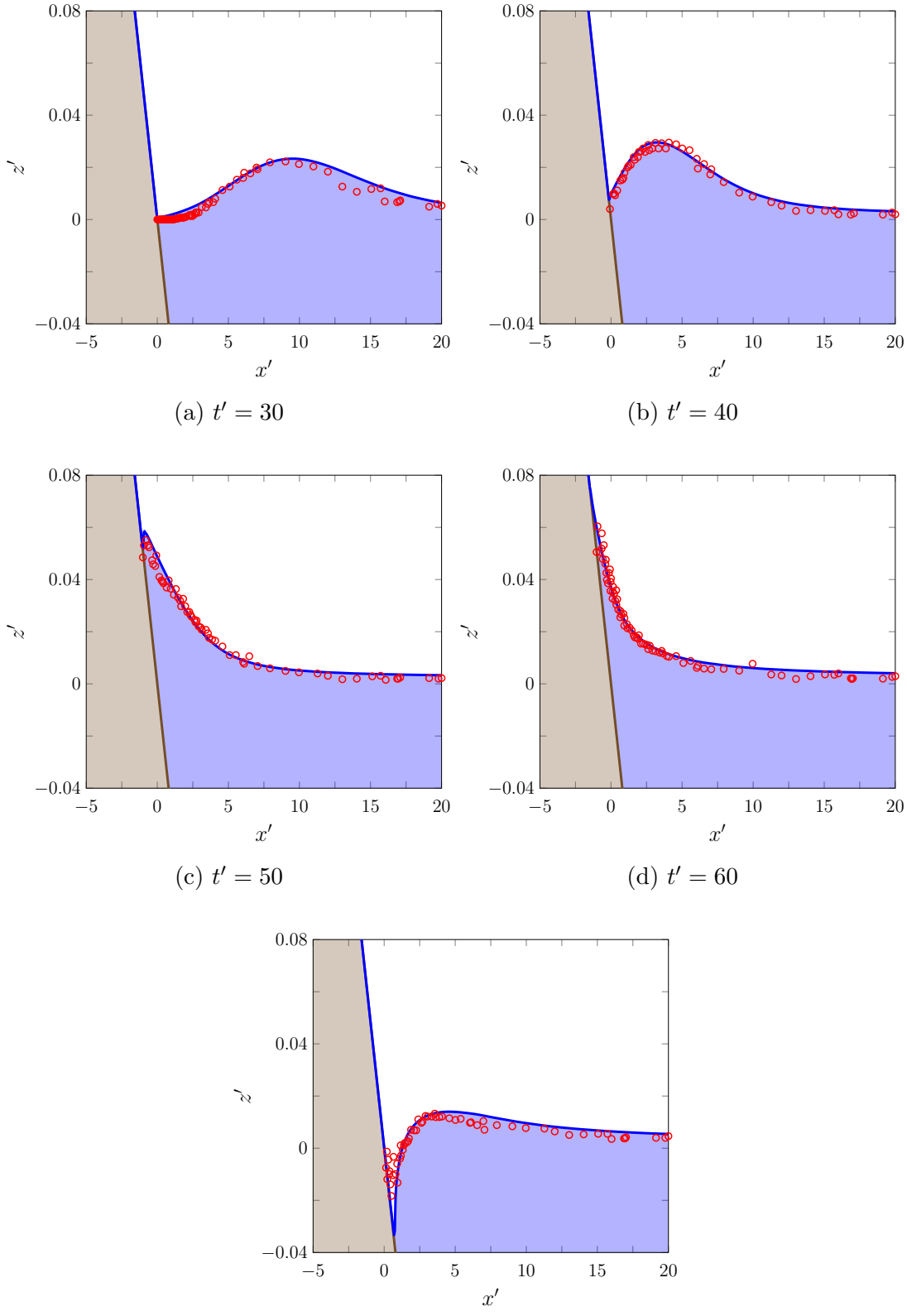

(a) $t' = 30$ (b) $t' = 40$

(c) $t' = 50$ (d) $t' = 60$

(e) $t' = 70$

Figure 6.24: A comparison of the water surface profiles $w(x', t')$ for the experiment (○) and the numerical solution (□) produced by FDVM$_2$ over the bed (□) at various times.

Quantity	$\mathcal{C}^*(\boldsymbol{q}^0)$	$\mathcal{C}^*(\boldsymbol{q}^*)$	$C^*(\boldsymbol{q}^0, \boldsymbol{q}^*)$
h	140.4170	140.4170	7.65×10^{-12}
$\mathcal{H}$	68.3900	68.3914	2.16×10^{-5}

Table 6.5: Initial and final total amounts and the conservation error for h and $\mathcal{H}$ for the numerical solution of FEVM_2 for the run-up experiment.

Quantity	$\mathcal{C}^*(\boldsymbol{q}^0)$	$\mathcal{C}^*(\boldsymbol{q}^*)$	$C^*(\boldsymbol{q}^0, \boldsymbol{q}^*)$
h	140.4170	140.4170	1.11×10^{-7}
$\mathcal{H}$	68.3900	68.3914	2.16×10^{-5}

Table 6.6: Initial and final total amounts and the conservation error for h and $\mathcal{H}$ for the numerical solution of FDVM_2 for the run-up experiment.

the omission of bed friction for the Serre equations in this thesis.

Both h and $\mathcal{H}$ are well conserved by the method throughout the run-up and run-down of the wave, particularly h. The total energy $\mathcal{H}$ of the method is also well conserved, however $\mathcal{H}$ appears to have slightly increased in the method during the run-up process due to the methods handling of the dry bed problem. During this experiment kinetic energy is converted into gravitational potential energy and then back again as the wave is reflected, therefore uh and G will only be conserved in this experiment after the wave has completely reflected from the beach. Full reflection of the wave has not occurred by $t' = 70s$ and so the conservation results for uh and G were omitted from Tables 6.5 and 6.6.

These numerical solutions demonstrate good agreement with experimental results and display the capability of the method to model the inundation of non-breaking waves.

In this chapter FEVM_2 and FDVM_2 were validated using experimental data. It was found that for most experiments the solutions of FEVM_2 and FDVM_2 were indistinguishable although FEVM_2 is the preferred method due to its greater robustness.

Chapter 7

Conclusion

The evolution of the dam-break problem for the Serre equations was comprehensively studied using various numerical methods resulting in the observation of new behaviours and the resolution of differences previously reported in the literature.

A well balanced second-order FEVM was described for the one-dimensional Serre equations. This method makes use of a consistent polynomial representation of the quantities over the cells from which all necessary terms can be calculated locally over the cell; making it a readily parrallelisable computational method. The method uses a finite element and a finite volume method and thus is robust to steep gradients present in the conserved variables h and G.

A linear analysis of the convergence and dispersion properties of FDVM_1, FDVM_2, FDVM_3, FEVM_2 , D and W was performed. The analysis demonstrated that FDVM_1, FDVM_2, FDVM_3, FEVM_2 and $\mathcal{D}$ are convergent methods, while $\mathcal{W}$ is only convergent when the mean background flow velocity is zero. The dispersion analysis demonstrated that all methods approximated the dispersion relation of the Serre equations with the expected order of accuracy. This analysis extended a previous analysis of the dispersion relationships of numerical methods [37] by allowing non-zero mean flow, combining the spatial and temporal analyses and comparing the real and imaginary parts of the dispersion error.

A comparison of the various numerical methods and the analytic solitary travelling wave solution of the Serre equations was performed. The expected order of accuracy and conservation properties of all the methods was observed. However, these results also demonstrated that the increase in accuracy achieved by a third-order method over a second-order method did not warrant the extra computational effort, justifying the further development of second-order methods over third-order methods for future work. For this reason only the second-order

$FDVM_2$ and $FEVM_2$ were developed further to allow varying bathymetry and dry beds.

The second-order $FDVM_2$ and $FEVM_2$ were then validated against the lake at rest steady state and the forced solutions. These results demonstrated that these methods are well balanced and accurately approximate all terms in the Serre equations in the presence of dry beds.

Finally the second-order $FDVM_2$ and $FEVM_2$ were compared to experimental data; demonstrating their modelling capabilities across a wide array of physical scenarios. These results established the greater robustness of $FEVM_2$; as $FDVM_2$ was found to be unstable for the solitary wave over a fringing reef experiment due to the presence of large jumps in the water surface as the wave moved into shallow water.

To summarise the major contributions of my research are

- Observation and justification of a new structure in the solution of the Serre equations to the dam-break problem;
- Development and description of the well balanced second-order finite element volume method that can handle dry beds and conserves h and G;
- Linear analysis of the convergence properties of the developed finite volume based methods and the mentioned finite difference methods;
- Analysis of the dispersion properties of the numerical methods, allowing for non-zero mean flow velocity and accounting for the total dispersion error;
- Validation of the numerical method against analytic and forced solutions and experimental results.

7.1 Future Work

Following the work conducted in this thesis; some natural extensions are

- Inclusion of wave-breaking in the model;
- Implementation of different boundary conditions;
- Incorporation of discontinuous bed profiles;
- Incorporation of bed friction in the method;

- A complete analysis of the convergence properties of the FEVM;
- Extension of the FEVM to the two-dimensional Serre equations on unstructured meshes.

Appendix A

Additional Conservation Information

To calculate the conservation errors requires an analytic expression for the total amount of h, uh, G and $\mathcal{H}$ present in the initial conditions. Therefore, to facilitate the validation tests against the analytic solutions performed in Chapter 5 we present these analytic expressions for the initial conditions of the solitary travelling wave and the lake at rest solutions described in Chapter 2. To allow for the simple calculation of the integrals in a concise way for any domains we present the integrals in indefinite form.

A.1 Solitary Travelling Wave Solution

The solitary wave solution (2.11) is

$$h(x,t) = a_0 + a_1 \text{sech}^2\left(\kappa\left[x - ct\right]\right),$$

$$u(x,t) = c\left(1 - \frac{a_0}{h(x,t)}\right),$$
$$b(x) = 0.$$

When $t = 0$ the indefinite spatial integrals of the conserved quantities are

$$\int h(x,0)\, dx = a_0 x + \frac{a_1}{\kappa}\tanh\left(\kappa x\right) + \text{constant}, \tag{A.1a}$$

$$\int u(x,0)h(x,0)\, dx = \frac{a_1 c}{\kappa}\tanh\left(\kappa x\right) + \text{constant}, \tag{A.1b}$$

$$\int G(x,0)\,dx = \frac{ca_1}{3\kappa}\Bigg(3 + 2a_0^2\kappa^2\mathrm{sech}^2\left(\kappa x\right) + 2a_0a_1\kappa^2\mathrm{sech}^4\left(\kappa x\right)\Bigg)\tanh\left(\kappa x\right) + \text{constant}, \tag{A.1c}$$

$$\int \mathcal{H}(x,0)\,dx = \frac{1}{2}\Bigg(\int g\left[h(x,0)\right]^2\,dx + \int h(x,0)\left[u(x,0)\right]^2\,dx + \int \left[h(x,0)\right]^3\left[\frac{\partial u(x,0)}{\partial x}\right]^2\,dx\Bigg) \tag{A.1d}$$

where these integrals making up $\mathcal{H}$ are

$$\int g\left[h(x,0)\right]^2\,dx = \frac{g}{12\kappa}\mathrm{sech}^3\left(\kappa x\right)\Bigg(9a_0^2\kappa x\cosh\left(\kappa x\right) + 4a_1\left[3a_0 + 2a_1 + \left(3a_0 + a_1\right)\cosh\left(2\kappa x\right)\right]\sinh\left(\kappa x\right) + 3a_0^2\kappa x\cosh\left(3\kappa x\right)\Bigg) + \text{constant},$$

$$\int h(x,0)\left[u(x,0)\right]^2\,dx = \frac{\sqrt{a_1}c^2}{\kappa}\Bigg(-\frac{a0}{\sqrt{a_0+a_1}}\mathrm{arctanh}\left(\frac{\sqrt{a1}\tanh\left(\kappa x\right)}{\sqrt{a_0+a1}}\right) + \frac{\sqrt{a_1}}{\kappa}\tanh\left(\kappa x\right)\Bigg) + \text{constant},$$

$$\int \left[h(x,0)\right]^3\left[\frac{\partial u(x,0)}{\partial x}\right]^2\,dx = \frac{2a_0^2c^2\kappa}{9\sqrt{a_1}\left(a_0 + a_1\mathrm{sech}^2\left(\kappa x\right)\right)} \times \left(a_0 + 2a_1 + a_0\cosh\left(2\kappa x\right)\right)\mathrm{sech}^2\left(\kappa x\right) \times \Bigg(-3a_0\sqrt{a_0+a_1}\mathrm{arctanh}\left(\frac{\sqrt{a1}\tanh\left(\kappa x\right)}{\sqrt{a_0+a1}}\right) + \sqrt{a_1}\left[3a_0 + a_1 - a_1\mathrm{sech}^2\left(\kappa x\right)\right]\tanh(\kappa x)\Bigg) + \text{constant}.$$

Therefore, we have the analytic values of the total amounts of our conserved quantities for the solitary travelling wave solution (2.11) when $t = 0s$, as desired.

A.2 Lake At Rest Solution

The lake at rest solution (2.12) for an arbitrary bed profile $b(x)$ is

$$\begin{aligned} h(x,t) &= \max\left\{a_0 - b(x), 0\right\}, \\ u(x,t) &= 0, \\ G(x,t) &= 0. \end{aligned}$$

The total amount of uh and G in the system are straightforward to calculate as both are zero everywhere and so we have

$$\begin{aligned} \int u(x,0)h(x,0)\ dx &= 0 + \text{constant}, \\ \int G(x,0)\ dx &= 0 + \text{constant}. \end{aligned}$$

To calculate the total h and $\mathcal{H}$ in the solution we must partition the domain into wet regions where $b(x) < a_0$ and dry regions where $b(x) \geq a_0$. For the dry regions the h and $\mathcal{H}$ are zero everywhere and so we have

$$\begin{aligned} \int h(x,0)\ dx &= 0 + \text{constant}, \\ \int \mathcal{H}(x,0)\ dx &= 0 + \text{constant} \end{aligned}$$

whilst in a wet region we have

$$\int h(x,0)\ dx = a_0 x - \int b(x)\ dx + \text{constant}, \tag{A.2a}$$

$$\int \mathcal{H}(x,0)\ dx = \frac{g}{2}\left(a_0^2 x - 2a_0 \int b(x)\ dx + \int b(x)^2\ dx\right) + \text{constant}. \tag{A.2b}$$

By summing all the wet regions in a given domain together we can calculate the total amount of h and $\mathcal{H}$ in the system from these expressions, in terms of the bed profile $b(x)$, as desired.

Appendix B

Finite Element Method Details

The definitions of the basis functions of the finite element method used by FEVM_2 described in Chapter 3 and the function spaces mentioned in Chapter 3 are provided here. Beginning with the basis function definitions.

B.1 Basis Functions

Since all integrals of the basis functions are calculated with respect to the variable ξ, the basis functions are given in terms of ξ. The mapping from the x-space of the numerical grid to the canonical ξ-space is

$$x = x_j + \xi \frac{\Delta x}{2}.$$

This mapping takes the j^{th} cell $\left[x_{j-1/2}, x_{j+1/2}\right]$ in the x-space to the interval $[-1, 1]$ in the ξ-space.

The basis functions ψ for h and G shown in Figure B.1 are

$$\psi^{+}_{j-1/2} = \begin{cases} \frac{1}{2}(1-\xi) & -1 \leq \xi \leq 1 \\ 0 & \text{otherwise,} \end{cases} \tag{B.1a}$$

$$\psi^{-}_{j+1/2} = \begin{cases} \frac{1}{2}(1+\xi) & -1 \leq \xi \leq 1 \\ 0 & \text{otherwise.} \end{cases} \tag{B.1b}$$

The basis functions ϕ for u and the test function v displayed in Figure B.2

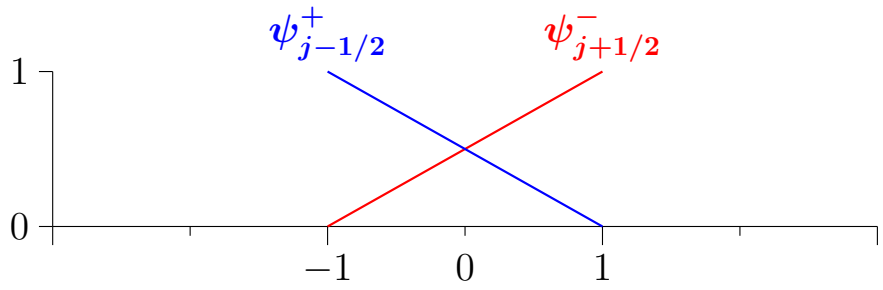

Figure B.1: Support of the discontinuous linear basis functions ψ in the ξ-space.

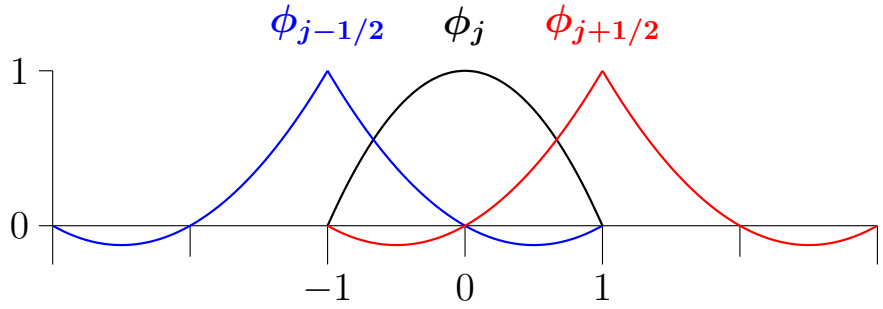

Figure B.2: Support of the continuous piecewise quadratic basis functions ϕ in the ξ-space.

are given by

$$\phi_{j-1/2} = \begin{cases} 2\left(\xi + \frac{3}{2}\right)(\xi + 2) & -2 \le \xi \le -1 \\ \frac{1}{2}\xi(\xi - 1) & -1 \le \xi \le 1 \\ 0 & \text{otherwise,} \end{cases} \tag{B.2a}$$

$$\phi_j = \begin{cases} -(\xi - 1)(\xi + 1) & -1 \le \xi \le 1 \\ 0 & \text{otherwise,} \end{cases} \tag{B.2b}$$

$$\phi_{j+1/2} = \begin{cases} \frac{1}{2}\xi(\xi + 1) & -1 \le \xi \le 1 \\ 2(\xi - 2)\left(\xi - \frac{3}{2}\right) & 1 \le \xi \le 2 \\ 0 & \text{otherwise.} \end{cases} \tag{B.2c}$$

Finally the basis functions γ for the bed profile b displayed in Figure 3.5 are

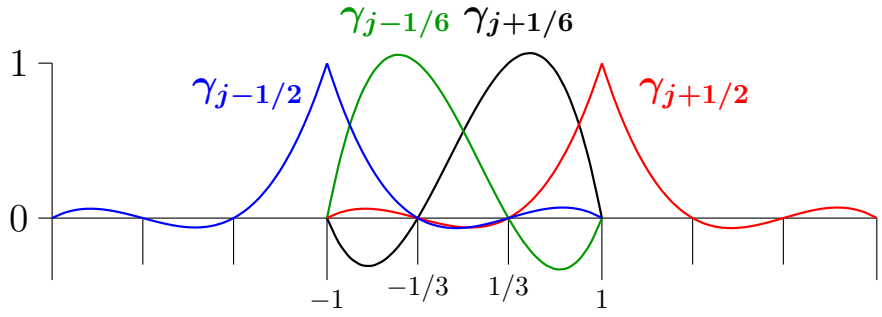

Figure B.3: Support of the continuous piecewise cubic basis functions γ in the ξ-space.

given by

$$\gamma_{j-1/2} = \begin{cases} \frac{9}{2}\left(\xi+\frac{4}{3}\right)\left(\xi+\frac{5}{3}\right)(\xi+2) & -2 \le \xi \le -1 \\ \frac{9}{16}(\xi-1)\left(\xi-\frac{1}{3}\right)\left(\xi+\frac{1}{3}\right) & -1 \le \xi \le 1 \\ 0 & \text{otherwise,} \end{cases} \tag{B.3a}$$

$$\gamma_{j-1/6} = \begin{cases} \frac{27}{16}(\xi-1)\left(\xi-\frac{1}{3}\right)(\xi+1) & -1 \le \xi \le 1 \\ 0 & \text{otherwise,} \end{cases} \tag{B.3b}$$

$$\gamma_{j+1/6} = \begin{cases} -\frac{27}{16}(\xi-1)\left(\xi+\frac{1}{3}\right)(\xi+1) & -1 \le \xi \le 1 \\ 0 & \text{otherwise,} \end{cases} \tag{B.3c}$$

$$\gamma_{j-1/2} = \begin{cases} \frac{9}{16}(\xi+1)\left(\xi-\frac{1}{3}\right)\left(\xi+\frac{1}{3}\right) & -1 \le \xi \le 1 \\ -\frac{9}{2}\left(\xi-\frac{4}{3}\right)\left(\xi-\frac{5}{3}\right)(\xi-2) & 1 \le \xi \le 2 \\ 0 & \text{otherwise.} \end{cases} \tag{B.3d}$$

The calculation of the derivatives of these basis functions with respect to ξ are straightforward and hence omitted.

B.2 Function Spaces

The function spaces mentioned in Chapter 3 are the space of square integrable functions $\mathbb{L}^2(\Omega)$ and the Sobolev space $\mathbb{W}^{k,2}(\Omega)$. To be precise we now define these function spaces here.

A function $f(x)$ is in $\mathbb{L}^2(\Omega)$ if

$$\left(\int_\Omega f(x)^2\, dx\right)^{\frac{1}{2}} < \infty.$$

While $f(x)$ is in $\mathbb{W}^{k,2}(\Omega)$ if

$$\left(\int_{\Omega} f(x)^2 \, dx + \sum_{j=1}^{k} \int_{\Omega} \left[D^j f(x) \right]^2 \, dx \right)^{\frac{1}{2}} < \infty.$$

where $D^j f(x)$ is the j^{th} weak derivative of $f(x)$.

Appendix C

Linear Analysis Results

In this appendix we present all the components to calculate the evolution matrix $\mathbf{E}$ for FDVM_1, FDVM_2, FDVM_3, $\mathcal{D}$ and $\mathcal{W}$. Descriptions of FDVM_1, FDVM_2 and FDVM_3 were published by Zoppou et al. [15] and descriptions of $\mathcal{D}$ and $\mathcal{W}$ were published by Pitt et al. [14]. Given the results in Chapter 4 for FEVM_2 the evolution matrix for FDVM_1, FDVM_2 and FDVM_3 can be straightforwardly calculated following the procedure outlined here. While for $\mathcal{D}$ and $\mathcal{W}$ the evolution matrix itself is provided.

C.1 Finite Difference Volume Methods

For the Finite Difference Volume Methods (FDVM) the evolution matrix is a 2×2 matrix that gives the following relationship (4.1)

$$\begin{bmatrix} \overline{\eta} \\ \overline{G} \end{bmatrix}_j^{n+1} = \mathbf{E} \begin{bmatrix} \overline{\eta} \\ \overline{G} \end{bmatrix}_j^{n} \tag{C.1}$$

The evolution matrices for the FDVM can be calculated in terms of the flux matrix $\mathbf{F}$ based on the order of the SSP Runge-Kutta timestepping used in the method. The expressions for $\mathbf{E}$ in terms of $\mathbf{F}$ for each FDVM are summarised in Table C.1.

To calculate the flux matrix $\mathbf{F}$ we have from (4.12) that

$$\mathbf{F} = -\frac{\left(1 - e^{-ik\Delta x}\right)}{\Delta x} \begin{bmatrix} \mathcal{F}^{\eta,\eta} & \mathcal{F}^{\eta,G} \\ \mathcal{F}^{G,\eta} & \mathcal{F}^{G,G} \end{bmatrix}.$$

Where $\mathcal{F}^{\eta,\eta}$, $\mathcal{F}^{G,\eta}$, $\mathcal{F}^{G,G}$ depend on the Froude number $Fr = U/\sqrt{gH}$ and the constituent operators of the method. The factor $\mathcal{F}^{\eta,G}$ in the flux matrix does not

Method	$\mathbf{E}$
FDVM_1	$\mathbf{I} - \Delta t\mathbf{F}$
FDVM_2 and FEVM_2	$\mathbf{I} - \Delta t\mathbf{F} + \frac{1}{2}\Delta t^2\mathbf{F}^2$
FDVM_3	$\mathbf{I} - \Delta t\mathbf{F} + \frac{1}{2}\Delta t^2\mathbf{F}^2 - \frac{1}{6}\Delta t^3\mathbf{F}^3$

Table C.1: Formula for $\mathbf{E}$ given $\mathbf{F}$ determined by the SSP Runge-Kutta timestepping method.

vary with the Froude number and is

$$\mathcal{F}^{\eta,G} = H\mathcal{G}^G$$

The expressions for the other coefficients of $\mathbf{F}$ are summarised in Tables C.2-C.4 for all values of Fr with $\mathcal{F}^{\eta,\eta}$ in Table C.2, $\mathcal{F}^{G,\eta}$ in Table C.3 and $\mathcal{F}^{G,G}$ in Table C.4.

Given the expressions for $\mathcal{F}^{\eta,\eta}$, $\mathcal{F}^{\eta,G}$, $\mathcal{F}^{G,\eta}$ and $\mathcal{F}^{G,G}$. Replace the operators $\mathcal{R}_j$, $\mathcal{R}^+_{j-1/2}$, $\mathcal{R}^-_{j+1/2}$, $\mathcal{G}^\eta$ and $\mathcal{G}^G$ with the appropriate ones for the FDVM. The expressions for these fundamental operators of each FDVM are given in Table C.5 for $\mathcal{R}_j$, Table C.6 for $\mathcal{R}^+_{j-1/2}$, Table C.7 for $\mathcal{R}^-_{j+1/2}$ and Table C.8 for $\mathcal{G}^G$. Since $\mathcal{G}^\eta = -U\mathcal{G}^G$ we have only provided the table for $\mathcal{G}^G$.

From this process the evolution matrix $\mathbf{E}$ for all FDVM for all flow scenarios is obtained as desired.

Tables C.5-C.8 also include the operators for FEVM_2 summarising the work in Chapter 4. Additionally, the analytic value of the operators for an exact method are also provided as well as the lowest order term of the Taylor series of the difference between the operator in a method and the exact operator. The reported Taylor series results demonstrate that all methods use operators with the appropriate order of accuracy or better.

Froude Number	$\mathcal{F}^{\eta,\eta}$
$Fr < -1$	$H\mathcal{G}^{\eta} + U\mathcal{R}^{+}_{j+1/2}$
$-1 \leq Fr \leq 1$	$H\mathcal{G}^{\eta} + \frac{U}{2}\left(\mathcal{R}^{-}_{j+1/2} + \mathcal{R}^{+}_{j+1/2}\right) - \frac{\sqrt{gH}}{2}\left(\mathcal{R}^{+}_{j+1/2} - \mathcal{R}^{-}_{j+1/2}\right)$
$1 < Fr$	$H\mathcal{G}^{\eta} + U\mathcal{R}^{-}_{j+1/2}$

Table C.2: Factor $\mathcal{F}^{\eta,\eta}$ that multiples η in the flux function for η for each FDVM and the FEVM.

Froude Number	$\mathcal{F}^{G,\eta}$
$Fr < -1$	$UH\mathcal{G}^{\eta} + gH\mathcal{R}^{+}_{j+1/2}$
$-1 \leq Fr \leq 1$	$\frac{U\sqrt{gH}}{2}\left(\mathcal{R}^{-}_{j+1/2} - \mathcal{R}^{+}_{j+1/2}\right) + UH\mathcal{G}^{\eta} + \frac{gH}{2}\left(\mathcal{R}^{-}_{j+1/2} + \mathcal{R}^{+}_{j+1/2}\right)$
$1 < Fr$	$UH\mathcal{G}^{\eta} + gH\mathcal{R}^{-}_{j+1/2}$

Table C.3: Factor $\mathcal{F}^{G,\eta}$ that multiples η in the flux function for G for each FDVM and the FEVM.

Froude Number	$\mathcal{F}^{G,G}$
$Fr < -1$	$U\mathcal{R}^{+}_{j+1/2} + UH\mathcal{G}^{G}$
$-1 \leq Fr \leq 1$	$UH\mathcal{G}^{G} + + \frac{U}{2}\left(\mathcal{R}^{-}_{j+1/2} + \mathcal{R}^{+}_{j+1/2}\right) - \frac{\sqrt{gH}}{2}\left(\mathcal{R}^{+}_{j+1/2} - \mathcal{R}^{-}_{j+1/2}\right)$
$1 < Fr$	$U\mathcal{R}^{+}_{j+1/2} + UH\mathcal{G}^{G}$

Table C.4: Factor $\mathcal{F}^{G,G}$ that multiples G in the flux function for G for each FDVM and the FEVM.

Method	$\mathcal{R}_j$	Lowest Order Term of Method - Exact
Exact	$\frac{k\Delta x}{2\sin\left(k\frac{\Delta x}{2}\right)}$	-
FDVM_1	1	$-\frac{1}{24}k^2\Delta x^2$
FDVM_2 and FEVM_2	1	$-\frac{1}{24}k^2\Delta x^2$
FDVM_3	$\frac{26 - 2\cos(k\Delta x)}{24}$	$-\frac{3}{640}k^4\Delta x^4$

Table C.5: Factor $\mathcal{R}_j$ from reconstructing the nodal value at the midpoint and the lowest order term of the Taylor series of the factor in the method minus the exact factor for each finite volume based method.

Method	$\mathcal{R}^{+}_{j-1/2}$	Lowest Order Term of Method - Exact
Exact	$e^{-\frac{ik\Delta x}{2}} \frac{k\Delta x}{2\sin\left(\frac{k\Delta x}{2}\right)}$	-
$FDVM_1$	1	$\frac{i}{2}k\Delta x$
$FDVM_2$ and $FEVM_2$	$1 - \frac{i\sin(k\Delta x)}{2}$	$\frac{1}{12}k^2\Delta x^2$
$FDVM_3$	$\frac{1}{6}\left(5 + 2e^{-ik\Delta x} - e^{ik\Delta x}\right)$	$\frac{i}{12}k^3\Delta x^3$

Table C.6: Factor $\mathcal{R}^{+}_{j-1/2}$ from the reconstruction of η and G at $x_{j+1/2}$ from the $(j+1)^{th}$ cell and the lowest order term of the Taylor series of the factor in the method minus the exact factor for each finite volume based method.

Method	$\mathcal{R}^{-}_{j+1/2}$	Lowest Order Term of Method - Exact
Exact	$e^{\frac{ik\Delta x}{2}} \frac{k\Delta x}{2\sin\left(\frac{k\Delta x}{2}\right)}$	-
$FDVM_1$	1	$-\frac{i}{2}k\Delta x$
$FDVM_2$ and $FEVM_2$	$1+\frac{i\sin(k\Delta x)}{2}$	$\frac{1}{12}k^2\Delta x^2$
$FDVM_3$	$\frac{1}{6}\left(5-e^{-ik\Delta x}+2e^{ik\Delta x}\right)$	$-\frac{i}{12}k^3\Delta x^3$

Table C.7: Factor $\mathcal{R}^{-}_{j+1/2}$ from the reconstruction of η and G at $x_{j+1/2}$ using the j^{th} cell and the lowest order term of the Taylor series of the factor in the method minus the exact factor for each finite volume based method.

Method	$\mathcal{G}^G$	Lowest Order Term of Method - Exact
Exact	$\frac{3}{3H+H^3k^2}\frac{k\Delta x}{2\sin\left(\frac{k\Delta x}{2}\right)}e^{\frac{ik\Delta x}{2}}$	-
FDVM_1	$\frac{3\Delta x^2\left(1+e^{ik\Delta x}\right)}{6\Delta x^2H-2H^3\left(2\cos\left(k\Delta x\right)-2\right)}$	$-\frac{6+H^2k^2}{4H\left(3+H^2k^2\right)^2}k^2\Delta x^2$
FDVM_2	$\frac{3\Delta x^2\left(1+e^{ik\Delta x}\right)}{6\Delta x^2H-2H^3\left(2\cos\left(k\Delta x\right)-2\right)}$	$-\frac{6+H^2k^2}{4H\left(3+H^2k^2\right)^2}k^2\Delta x^2$
FEVM_2	$\frac{\Delta x}{6}\left(1+\frac{i\sin\left(k\Delta x\right)}{2}+e^{ik\Delta x}\left[1-\frac{i\sin\left(k\Delta x\right)}{2}\right]\right)$ $\div\left(H\frac{\Delta x}{30}\left[4\cos\left(\frac{k\Delta x}{2}\right)-2\cos\left(k\Delta x\right)+8\right]\right.$ $\left.+\frac{H^3}{9\Delta x}\left[-16\cos\left(\frac{k\Delta x}{2}\right)+2\cos\left(k\Delta x\right)+14\right]\right)$	$\frac{12+5H^2k^2}{40H\left(3+H^2k^2\right)^2}k^2\Delta x^2$
FDVM_3	$\frac{9\Delta x^2\left(-e^{-ik\Delta x}+9e^{ik\Delta x}-e^{2ik\Delta x}+9\right)}{144\Delta x^2H-4H^3\left(32\cos\left(k\Delta x\right)-2\cos\left(2k\Delta x\right)-30\right)}$	$-\frac{243+49H^2k^2}{960H\left(3+H^2k^2\right)^2}k^4\Delta x^4$

Table C.8: Factor $\mathcal{G}^G$ that multiples G given by solving (4.3c) for $v_{j+1/2}$ and the lowest order term of the Taylor series of the factor in the method minus the exact factor for each finite volume based method.

C.2 Finite Difference Methods

For the Finite Difference Methods (FDM) the evolution matrix $\mathbf{E}$ can be thought of in two ways. Naively as a 4×4 matrix producing the following relationship

$$\begin{bmatrix} \eta^{n+1} \\ \mu^{n+1} \\ \eta^{n} \\ \mu^{n} \end{bmatrix}_j = \mathbf{E} \begin{bmatrix} \eta^{n} \\ \mu^{n} \\ \eta^{n-1} \\ \mu^{n-1} \end{bmatrix}_j \tag{C.2}$$

where the time superscript was brought inside the vector to make clear the time step at which the different elements are placed. Since the FDM are used to calculate η_j^{n+1} and μ_j^{n+1} given η_j^n, μ_j^n, η_j^{n-1} and μ_j^{n-1} their evolution matrices have the following structure

$$\mathbf{E} = \begin{bmatrix} E_{0,0} & E_{0,1} & E_{0,2} & E_{0,3} \\ E_{1,0} & E_{1,1} & E_{1,2} & E_{1,3} \\ 1 & 0 & 0 & 0 \\ 0 & 1 & 0 & 0 \end{bmatrix}. \tag{C.3}$$

Because $\eta_j^{n-1} = e^{-i\omega^{\pm}\Delta t}\eta_j^n$ and $\mu_j^{n-1} = e^{-i\omega^{\pm}\Delta t}\mu_j^n$ as η and μ are Fourier modes (4.5) then (C.2) can be rewritten as

$$\begin{bmatrix} \eta \\ \mu \end{bmatrix}_j^{n+1} = \mathbf{E}^{(2\times 2)} \begin{bmatrix} \eta \\ \mu \end{bmatrix}_j^{n} \tag{C.4}$$

where $\mathbf{E}^{(2\times 2)}$ is a 2×2 matrix that depends on the elements of $\mathbf{E}$ in the following way

$$\mathbf{E}^{(2\times 2)} = \begin{bmatrix} E_{0,0} + e^{-i\omega^{\pm}\Delta t}E_{0,2} & E_{0,1} + e^{-i\omega^{\pm}\Delta t}E_{0,3} \\ E_{1,0} + e^{-i\omega^{\pm}\Delta t}E_{1,2} & E_{1,1} + e^{-i\omega^{\pm}\Delta t}E_{1,3} \end{bmatrix}. \tag{C.5}$$

The stability analysis was then performed by finding the spectral radius of the naive evolution matrix $\mathbf{E}$ of the FDM (C.2). The consistency analysis was based on comparing the 2×2 evolution matrix $\mathbf{E}^{(2\times 2)}$ (C.5) to the exact evolution matrix $e^{i\omega^{\pm}\Delta t}\mathbf{I}$. Finally, the dispersion error was based on the eigenvalues of $\mathbf{E}$ (C.2), this matrix has an additional two eigenvalues beyond the ones given by $e^{i\omega^{+}\Delta t}$ and $e^{i\omega^{-}\Delta t}$ that we ignored. We found the methods had the same stability and dispersion properties when $\mathbf{E}^{(2\times 2)}$ was investigated. We will now present the 4×4 evolution matrices for $\mathcal{D}$ and $\mathcal{W}$. Given these matrices the corresponding 2×2 evolution matrix $\mathbf{E}^{(2\times 2)}$ can be calculated using (C.5).

By using (4.6) all the derivative approximations in the finite difference methods $\mathcal{D}$ and $\mathcal{W}$ can be written as operators that are constant in j and n as was done for the finite volume based methods.

The evolution matrix for $\mathcal{D}$ is

$$\mathbf{E} = \begin{bmatrix} E_{0,0} & E_{0,1} & 1 & 0 \\ E_{1,0} & E_{1,1} & 0 & 1 \\ 1 & 0 & 0 & 0 \\ 0 & 1 & 0 & 0 \end{bmatrix} \tag{C.6}$$

with

$$E_{0,0} = -\frac{2i\Delta t}{\Delta x} U \sin\left(k\Delta x\right),$$

$$E_{0,1} = -\frac{2i\Delta t}{\Delta x} H \sin\left(k\Delta x\right),$$

$$E_{1,0} = -\frac{6gi\Delta x\Delta t}{3\Delta x^2 - 2H^2\left(\cos\left(k\Delta x\right) - 1\right)} \sin\left(k\Delta x\right),$$

$$E_{1,1} = -\frac{2i\Delta t}{\Delta x} U \sin\left(k\Delta x\right).$$

While for $\mathcal{W}$ the evolution matrix is

$$\mathbf{E} = \begin{bmatrix} E_{0,0} & E_{0,1} & 0 & E_{0,3} \\ E_{1,0} & E_{1,1} & 0 & 1 \\ 1 & 0 & 0 & 0 \\ 0 & 1 & 0 & 0 \end{bmatrix} \tag{C.7}$$

with

$$E_{0,0} = 1 - \frac{\Delta t}{\Delta x}\left(-\frac{6gi\Delta x\Delta t}{3\Delta x^2 - 2H^2\left(\cos\left(k\Delta x\right)-1\right)}\sin\left(k\Delta x\right)\right)H\frac{i\sin\left(k\Delta x\right)}{2} - \frac{\Delta t}{\Delta x}U\left(i\sin\left(k\Delta x\right) - \frac{\Delta t}{\Delta x}U\left(\cos\left(k\Delta x\right)-1\right)\right),$$

$$E_{0,1} = -\frac{\Delta t}{\Delta x}\left(H\frac{i\sin\left(k\Delta x\right)}{2}\left[1 - \frac{2i\Delta t}{\Delta x}U\sin\left(k\Delta x\right)\right] - U\left[\frac{\Delta t}{\Delta x}H\left(\cos\left(k\Delta x\right)-1\right)\right]\right),$$

$$E_{0,3} = -\frac{\Delta t}{\Delta x}H\frac{i\sin\left(k\Delta x\right)}{2},$$

$$E_{1,0} = -\frac{6gi\Delta x\Delta t}{3\Delta x^2 - 2H^2\left(\cos\left(k\Delta x\right)-1\right)}\sin\left(k\Delta x\right),$$

$$E_{1,1} = -\frac{2i\Delta t}{\Delta x}U\sin\left(k\Delta x\right).$$

C.3 Consistency Results

The consistency results for FDVM_1, FDVM_2, FDVM_3, $\mathcal{D}$ and $\mathcal{W}$ are provided here. For FDVM_1, FDVM_2 and FDVM_3 we compare the evolution matrices $\mathbf{E}$ given by the finding the relationship (C.1) to the exact evolution matrix $e^{i\omega^{\pm}\Delta t}\mathbf{I}$ (4.16). Since the results are similar for ω^- and ω^+ we only give the results for ω^+. These results are presented in Tables C.9 and C.10 for FDVM_1, Table C.11 for FDVM_2 and Tables C.12 and C.13 for FDVM_3.

For $\mathcal{D}$ and $\mathcal{W}$ we compare the 2×2 evolution matrices $\mathbf{E}^{(2\times 2)}$ (C.5) to the exact evolution matrix $e^{i\omega^{\pm}\Delta t}\mathbf{I}$ (4.16). Since the results are similar for ω^- and ω^+ we only give the results for ω^+. The results for ω^+ are presented in Table C.14 for $\mathcal{D}$ and Table C.15 for $\mathcal{W}$.

Element	Lowest Order Δx Term of $\mathbf{E} - e^{i\omega^+\Delta t}\mathbf{I}$ for FDVM$_1$		
	$Fr < -1$	$-1 < Fr < 1$	$Fr > 1$
$E_{0,0} - e^{i\omega^+\Delta t}$	$\frac{1}{2}k^2U\Delta t\Delta x$	$-\frac{1}{2}\sqrt{gH}k^2\Delta t\Delta x$	$-\frac{1}{2}k^2U\Delta t\Delta x$
$E_{0,1}$	$\frac{1}{2}gHk^2\Delta t\Delta x$	$\frac{3+\beta}{4\beta^2}ik^3\Delta t\Delta x^2$	$\frac{1}{2}gHk^2\Delta t\Delta x$
$E_{1,0}$	$-\frac{1}{2}\sqrt{gH}k^2\Delta t\Delta x$	$-\frac{1}{2}\sqrt{gH}k^2\Delta t\Delta x$	$-\frac{1}{2}\sqrt{gH}k^2\Delta t\Delta x$
$E_{1,1} - e^{i\omega^+\Delta t}$	$\frac{1}{2}k^2U\Delta t\Delta x$	$-\frac{1}{2}\sqrt{gH}k^2\Delta t\Delta x$	$-\frac{1}{2}k^2U\Delta t\Delta x$

Table C.9: Lowest order Δx term of the Taylor series for the elements of $\mathbf{E} - e^{i\omega^+\Delta t}\mathbf{I}$ for FDVM$_1$. Here $\beta = 3 + k^2H^2$.

Element	Lowest Order Δt Term of $\mathbf{E} - e^{i\omega^+\Delta t}\mathbf{I}$ for FDVM$_1$
$E_{0,0} - e^{i\omega^+\Delta t}$	$\frac{\sqrt{3gH\beta} + 3U}{\beta}ik\Delta t$
$E_{0,1}$	$-\frac{3}{\beta}ik\Delta t$
$E_{1,0}$	$\left(-gH + \frac{3U^2}{\beta}\right)ik\Delta t$
$E_{1,1} - e^{i\omega^+\Delta t}$	$\frac{\sqrt{3gH\beta} - 3U}{\beta}ik\Delta t$

Table C.10: Lowest order Δt term of the Taylor series for the elements of $\mathbf{E} - e^{i\omega^+\Delta t}\mathbf{I}$ for FDVM$_1$ for all values of Fr. Here $\beta = 3 + k^2H^2$.

Element	Lowest Order Terms of $\mathbf{E} - e^{i\omega^+ \Delta t}\mathbf{I}$ for FDVM$_2$	
	Δx	Δt
$E_{0,0} - e^{i\omega^+ \Delta t}$	$-\frac{i\left(27 + 9H^2k^2 + H^4k^4\right)}{12\beta^2} U k^3 \Delta x^2$	$\frac{\sqrt{3gH\beta} + 3U}{\beta} ik\Delta t$
$E_{0,1}$	$\frac{3+\beta}{4\beta^2} ik^3 \Delta t \Delta x^2$	$-\frac{3}{\beta} ik\Delta t$
$E_{1,0}$	$-\left(gH + \frac{3U^2}{\beta} + \frac{9U^2}{\beta^2}\right)\frac{k^3}{12}\Delta t \Delta x^2$	$\left(-gH + \frac{3U^2}{\beta}\right) ik\Delta t$
$E_{1,1} - e^{i\omega^+ \Delta t}$	$\frac{-9 + H^2k^2\beta}{\beta^2}\frac{k^3}{12} iU\Delta t \Delta x^2$	$\frac{\sqrt{3gH\beta} - 3U}{\beta} ik\Delta t$

Table C.11: Lowest order terms of the Taylor series for the elements of $\mathbf{E} - e^{i\omega^+ \Delta t}\mathbf{I}$ for FDVM$_2$ for all values of Fr. Here $\beta = 3 + k^2H^2$.

Element	Lowest Order Δx Term of $\mathbf{E} - e^{i\omega^+\Delta t}\mathbf{I}$ for FDVM$_3$		
	$Fr < -1$	$-1 < Fr < 1$	$Fr > 1$
$E_{0,0} - e^{i\omega^+\Delta t}$	$\frac{1}{12}k^4U\Delta t\Delta x^3$	$-\frac{1}{12}\sqrt{gH}k^4\Delta t\Delta x^3$	$-\frac{1}{12}k^4U\Delta t\Delta x^3$
$E_{0,1}$	$\frac{1}{4\beta}iUk^5\Delta t^2\Delta x^3$	$\frac{\sqrt{gH}}{4\beta}ik^5\Delta t^2\Delta x^3$	$-\frac{1}{4\beta}iUk^5\Delta t^2\Delta x^3$
$E_{1,0}$	$\frac{1}{12}gHk^4\Delta t^2\Delta x^3$	$-\frac{1}{12}\sqrt{gH}k^4\Delta t\Delta x^3$	$-\frac{1}{12}gHk^4\Delta t^2\Delta x^3$
$E_{1,1} - e^{i\omega^+\Delta t}$	$\frac{1}{12}k^4U\Delta t\Delta x^3$	$-\frac{1}{12}\sqrt{gH}k^4\Delta t\Delta x^3$	$-\frac{1}{12}k^4U\Delta t\Delta x^3$

Table C.12: Lowest order Δx term of the Taylor series for the elements of $\mathbf{E} - e^{i\omega^+\Delta t}\mathbf{I}$ for FDVM$_3$. Here $\beta = 3 + k^2H^2$.

Element	Lowest Order Δt Term of $\mathbf{E} - e^{i\omega^+\Delta t}\mathbf{I}$ for FDVM$_3$
$E_{0,0} - e^{i\omega^+\Delta t}$	$\frac{\sqrt{3gH\beta} + 3U}{\beta}ik\Delta t$
$E_{0,1}$	$-\frac{3}{\beta}ik\Delta t$
$E_{1,0}$	$\left(-gH + \frac{3U^2}{\beta}\right)ik\Delta t$
$E_{1,1} - e^{i\omega^+\Delta t}$	$\frac{\sqrt{3gH\beta} - 3U}{\beta}ik\Delta t$

Table C.13: Lowest order Δt term of the Taylor series for the elements of $\mathbf{E} - e^{i\omega^+\Delta t}\mathbf{I}$ for FDVM$_3$ for all values of Fr. Here $\beta = 3 + k^2H^2$.

Element	Lowest Order Terms of $\mathbf{E}^{(2\times2)} - e^{i\omega^+\Delta t}\mathbf{I}$ for $\mathcal{D}$	
	Δx	Δt
$E_{0,0}^{(2\times2)} - e^{i\omega^+\Delta t}$	$\frac{ik^3}{3}U\Delta t\Delta x^2$	$\sqrt{\frac{3gH}{\beta}}2ik\Delta t$
$E_{0,1}^{(2\times2)}$	$\frac{iHk^3}{3}\Delta t\Delta x^2$	$-2Hik\Delta t$
$E_{1,0}^{(2\times2)}$	$\frac{ig\,(3+\beta)}{2\beta^2}k^3\Delta t\Delta x^2$	$-\frac{6igk}{\beta}\Delta t$
$E_{1,1}^{(2\times2)} - e^{i\omega^+\Delta t}$	$\frac{ik^3}{3}U\Delta t\Delta x^2$	$\sqrt{\frac{3gH}{\beta}}2ik\Delta t$

Table C.14: Lowest order terms of the Taylor series for the elements of $\mathbf{E}^{(2\times2)} - e^{i\omega^\pm\Delta t}\mathbf{I}$ for $\mathcal{D}$ for all values of Fr. Here $\beta = 3 + k^2H^2$.

Element	Lowest Order Terms of $\mathbf{E}^{(2\times2)} - e^{i\omega^+\Delta t}\mathbf{I}$ for $\mathcal{W}$	
	Δx	Δt
$E_{0,0}^{(2\times2)} - e^{i\omega^+\Delta t}$	$\frac{ik^3}{6}U\Delta t\Delta x^2$	$\sqrt{\frac{3gH}{\beta}}ik\Delta t$
$E_{0,1}^{(2\times2)}$	$\frac{iHk^3}{6}\Delta t\Delta x^2$	$-Hik\Delta t$
$E_{1,0}^{(2\times2)}$	$\frac{ig\,(3+\beta)}{2\beta^2}k^3\Delta t\Delta x^2$	$-\frac{6igk}{\beta}\Delta t$
$E_{1,1}^{(2\times2)} - e^{i\omega^+\Delta t}$	$\frac{ik^3}{3}U\Delta t\Delta x^2$	$\sqrt{\frac{3gH}{\beta}}2ik\Delta t$

Table C.15: Lowest order terms of the Taylor series for the elements of $\mathbf{E}^{(2\times2)} - e^{i\omega^+\Delta t}\mathbf{I}$ for $\mathcal{W}$ for all values of Fr. Here $\beta = 3 + k^2H^2$.

Appendix D

Publications

My research has resulted in the following publications in chronological order.

A Solution of the Conservation Law Form of the Serre Equations

Australia and New Zealand Industrial and Applied Mathematics Journal (2016)
C. Zoppou, S.G. Roberts and J. Pitt

Abstract:

The nonlinear and weakly dispersive Serre equations contain higher-order dispersive terms. These include mixed spatial and temporal derivative flux terms which are difficult to handle numerically. These terms can be replaced by an alternative combination of equivalent temporal and spatial terms, so that the Serre equations can be written in conservation law form. The water depth and new conserved quantities are evolved using a second-order finite-volume scheme. The remaining primitive variable, the depth-averaged horizontal velocity, is obtained by solving a second-order elliptic equation using simple finite differences. Using an analytical solution and simulating the dam-break problem, the proposed scheme is shown to be accurate, simple to implement and stable for a range of problems, including flows with steep gradients. It is only slightly more computationally expensive than solving the shallow water wave equations.

Numerical Solution of the Fully Non-Linear Weakly Dispersive Serre Equations for Steep Gradient Flows

Applied Mathematical Modelling (2017)

C. Zoppou, J. Pitt and S.G. Roberts

Abstract:

We demonstrate a numerical approach for solving the one-dimensional non-linear weakly dispersive Serre equations. By introducing a new conserved quantity the Serre equations can be written in conservation law form, where the velocity is recovered from the conserved quantities at each time step by solving an auxiliary elliptic equation. Numerical techniques for solving equations in conservative law form can then be applied to solve the Serre equations. We demonstrate how this is achieved. The system of conservation equations are solved using the finite volume method and the associated elliptic equation for the velocity is solved using a finite difference method. This robust approach allows us to accurately solve problems with steep gradients in the flow, such as those generated by discontinuities in the initial conditions.

The method is shown to be accurate, simple to implement and stable for a range of problems including flows with steep gradients and variable bathymetry.

Importance of Dispersion for Shoaling Waves

22nd International Congress on Modelling and Simulation (2017)
J. Pitt, C. Zoppou and S.G. Roberts

Abstract:

A tsunami has four main stages of its evolution; in the first stage the tsunami is generated, most commonly by seismic activity near subduction zones. The second stage is the tsunamis propagation through the ocean far from the coast, where variation in bathymetry is slight and gradual. The third stage is the shoaling and interaction of the tsunami with bathymetry as it approaches the coastline. Finally the tsunami reaches and inundates the shore. For our purposes the hydrodynamic models we are interested in deal with the final three stages of the evolution of a tsunami.

The propagation of a tsunami with wavelength λ through water that is H deep is well understood when $\lambda/H \leq 1/20$, which we call shallow water as noted by Sorensen (2006). The wavelengths for tsunamis range from a few to hundreds of kilometres, while the maximum water depth is $11km$ at the Marianas trench, so that most tsunamis occur in shallow water. This stage of tsunami behaviour is adequately modelled using the shallow water wave equations. Current research into tsunamis focuses around more complex approximations to the Euler equations for the third and fourth stages. In this paper we focused on the Serre equations as they are considered a very good model for fluid behaviour up to the shoreline, and they reduce to the shallow water wave equations for large wavelengths.

Although more complicated, the Serre equations provide a better description of the fluid behaviour than the shallow water wave equations and are therefore more computationally expensive to solve numerically. In particular for the methods of this work, we find that the Serre equations have a run-time 50% longer than our equivalent finite volume method for the shallow water wave equations in the one dimensional case. To simulate tsunamis as efficiently as possible it is important to know when using the more complicated Serre equations leads to more accurate predictions of the evolution of a tsunami than the shallow water wave equations. To investigate this we have numerically simulated a laboratory experiment of periodic waves propagating over a submerged bar, and the propagation of a small amplitude wave up a gradual linear slope using both the Serre and the shallow water wave equations.

The results of these simulations demonstrated that the Serre and shallow water

wave equations produce similar results for shoaling waves when the wavelength is large compared to the water depth. This is not surprising as this is the regime under which the shallow water wave equations are derived. However, outside this regime the shallow water wave equations are a poor model for wave shoaling and propagation, poorly approximating the shape and maximum height of waves. Furthermore we demonstrate that for steep waves generated by shoaling, the shallow water wave equations can underestimate the arrival time and amplitude of an incoming wave. These results suggest that for a tsunami it is sufficient to use the shallow water wave equations in stages two and some of stage three, even for large changes in bathymetry. Although dispersive equations such as the Serre equations are required to accurately capture fluid behaviour in stages three and four nearer to the coastline, particularly when wavelengths are short or waves are steep. Since the Serre equations represent only a moderate increase in run-times this suggests that our inundation models should be based on them.

Behaviour of the Serre Equations in the Presence of Steep Gradients Revisited

Wave Motion (2018)

J.P.A. Pitt, C. Zoppou and S.G. Roberts

Abstract:

We use numerical methods to study the short term behaviour of the Serre equations in the presence of steep gradients because there are no known analytical solutions for these problems. In keeping with the literature we study a class of initial condition problems that are a smooth approximation to the initial conditions of the dam-break problem. This class of initial condition problems allow us to observe the behaviour of the Serre equations with varying steepness of the initial conditions. The numerical solutions of the Serre equations are justified by demonstrating that as the resolution increases they converge to a solution with little error in conservation of mass, momentum and energy independent of the numerical method. We observe and justify four different structures of the converged numerical solutions depending on the steepness of the initial conditions. Two of these structures were observed in the literature, with the other two not being commonly found in the literature. The numerical solutions are then used to assess how well the analytical solution of the shallow water wave equations captures the mean behaviour of the solution of the Serre equations for the dam-break problem in the short term. Lastly the numerical solutions are compared to asymptotic results in the literature to approximate the depth and location of the front of an undular bore.

Bibliography

[1] L. Euler. Principes generaux du mouvement des fluides. *Mémoires de l'académie des sciences de Berlin*, 11:274–315, 1757.

[2] C.L.M.H. Navier. Mémoire sur les lois du mouvement des fluides. *Mémoires de l'Académie Royale des Sciences de l'Institut de France*, 6:389–440, 1823.

[3] G.G. Stokes. G.g. stokes, camb. trans. phil. soc. 8, 287 (1845). *Camb. Trans. Phil. Soc.*, 8:287, 1845.

[4] A.J. Chorin. The numerical solution of the Navier-Stokes equations for an incompressible fluid. *Bulletin of the American Mathematical Society*, 73(6): 928–931, 1967.

[5] C. Taylor and P. Hood. Numerical solution of the Navier-Stokes equations using the finite element technique. *Computers & Fluids*, 1:73–100, 1973.

[6] F. Bassi and S. Rebay. A high-order accurate discontinuous finite element method for the numerical solution of the compressible Navier-Stokes equations. *Journal of Computational Physics*, 131(2):267–279, 1997.

[7] D. Lannes and P. Bonneton. Derivation of asymptotic two-dimensional time-dependent equations for surface water wave propagation. *Physics of Fluids*, 21(1):16601, 2009.

[8] The Clawpack Development Team. Clawpack documentation, 2018. URL `http://www.clawpack.org/`.

[9] Xiaoming Wang. Comcot, 2009. URL `http://223.4.213.26/archive/tsunami/cornell/comcot.htm`.

[10] Stephen Roberts. ANUGA, 2018. URL `https://anuga.anu.edu.au/`.

[11] J. Grue, E.N. Pelinovsky, D. Fructus, T. Talipova, and C. Kharif. Formation of undular bores and solitary waves in the strait of Malacca caused by the 26 December 2004 Indian Ocean tsunami. *Journal of Geophysical Research: Oceans*, 113(C5):008, 2008.

[12] J.T. Kirby, F. Shi, B. Tehranirad, J.C. Harris, and S.T. Grilli. Dispersive tsunami waves in the ocean: Model equations and sensitivity to dispersion and coriolis effects. *Ocean Modelling*, 62:39–55, 2013.

[13] C. Zoppou. *Numerical Solution of the One-dimensional and Cylindrical Serre Equations for Rapidly Varying Free Surface Flows*. PhD thesis, Australian National University, Mathematical Sciences Institute, College of Physical and Mathematical Sciences, Australian National University, Canberra, ACT 2600, Australia, 2014.

[14] J.P.A. Pitt, C. Zoppou, and S.G. Roberts. Behaviour of the Serre equations in the presence of steep gradients revisited. *Wave Motion*, 76(1):61–77, 2018.

[15] C. Zoppou, J. Pitt, and S. Roberts. Numerical solution of the fully non-linear weakly dispersive Serre equations for steep gradient flows. *Applied Mathematical Modelling*, 48:70–95, 2017.

[16] Robert M. Sorensen. *Basic coastal engineering*. New York, NY Springer, 3rd edition, 2006.

[17] F. Serre. Contribtion à l'étude des écoulements permanents et variables dans les canaux. *La Houille Blanche*, 6:830–872, 1953.

[18] C.H. Su and C.S. Gardner. Korteweg-de Vries equation and generalisations. III. Derivation of the Korteweg-de Vries equation and Burgers equation. *Journal of Mathematical Physics*, 10(3):536–539, 1969.

[19] A.E. Green and P.M. Naghdi. A derivation of equations for wave propagation in water of variable depth. *Journal of Fluid Mechanics*, 78(2):237–246, 1976.

[20] F.J. Seabra-Santos, D.P. Renouard, and A.M. Temperville. Numerical and experimental study of the transformation of a solitary wave over a shelf or isolated obstacle. *Journal of Fluid Mechanics*, 176:117–134, 1981.

[21] E. Barthélemy. Nonlinear shallow water theories for coastal waves. *Surveys in Geophysics*, 25(3):315–337, 2004.

[22] P. Bonneton, F. Chazel, D. Lannes, F. Marche, and M. Tissier. A splitting approach for the fully nonlinear and weakly dispersive Green-Naghdi model. *Journal of Computational Physics*, 230(4):1479–1498, 2011.

[23] J.A. Liggett. *Fluid Mechanics*. McGraw-Hill civil engineering series. McGraw-Hill Inc., New York, 1994.

[24] O. Le Métayer, S. Gavrilyuk, and S. Hank. A numerical scheme for the Green-Naghdi model. *Journal of Computational Physics*, 229(6):2034–2045, 2010.

[25] M. Li, P. Guyenne, F. Li, and L. Xu. High order well-balanced CDG-FE methods for shallow water waves by a Green-Naghdi model. *Journal of Computational Physics*, 257(1):169–192, 2014.

[26] W. Choi and R. Camassa. Fully nonlinear internal waves in a two-fluid system. *Journal of Fluid Mechanics*, 396:1–36, 1999.

[27] J.D. Carter and R. Cienfuegos. The kinematics and stability of solitary and cnoidal wave solutions of the Serre equations. *European Journal of Mechanics-B/Fluids*, 30(3):259–268, 2011.

[28] Y.A. Li. Hamiltonian structure and linear stability of solitary waves of the Green-Naghdi equations. *Journal of Nonlinear Mathematical Physics*, 9:99–105, 2002.

[29] G.A. El, R.H.J. Grimshaw, and N.F. Smyth. Unsteady undular bores in fully nonlinear shallow-water theory. *Physics of Fluids*, 18(2):027104, 2006.

[30] D. Dutykh, D. Clamond, P. Milewski, and D. Mitsotakis. Finite volume and pseudo-spectral schemes for the fully nonlinear 1D Serre equations. *European Journal of Applied Mathematics*, 24(5):761–787, 2013.

[31] D. Mitsotakis, B. Ilan, and D. Dutykh. On the Galerkin/finite-element method for the Serre equations. *Journal of Scientific Computing*, 61(1): 166–195, 2014.

[32] D. Mitsotakis, D. Dutykh, and D. Carter. On the nonlinear dynamics of the traveling-wave solutions of the Serre system. *Wave Motion*, 70(1):166–182, 2017.

[33] J.S.A. do Carmo, J.A. Ferreira, L. Pinto, and G. Romanazzi. An improved Serre model: Efficient simulation and comparative evaluation. *Applied Mathematical Modelling*, 56:404–423, 2018.

[34] V.A. Dougalis, A. Duran, M.A. Lopez-Marcos, and D.E. Mitsotakis. Numerical study of the stability of solitary waves of the Bona–Smith family of Boussinesq systems. *Journal of Nonlinear Science*, 17(6):569–607, 2007.

[35] R. Cienfuegos, E. Barthélemy, and P. Bonneton. A fourth-order compact finite volume scheme for fully nonlinear and weakly dispersive Boussinesq-type equations. Part I: Model development and analysis. *International Journal for Numerical Methods in Fluids*, 51(11):1217–1253, 2006.

[36] S.F. Bradford and B.F. Sanders. Finite volume schemes for the Boussinesq equations. In *Ocean Wave Measurement and Analysis (2001)*, pages 953–962. American Society of Civil Engineers, 2002.

[37] A. G. Filippini, M. Kazolea, and M. Ricchiuto. A flexible genuinely nonlinear approach for nonlinear wave propagation, breaking and run-up. *Journal of Computational Physics*, 310:381–417, 2016.

[38] J. Pitt. *A Second Order Well Balanced Hybrid Finite Volume and Finite Difference Method for the Serre Equations*. Honour's thesis, Australian National University, Mathematical Sciences Institute, College of Physical and Mathematical Sciences, Australian National University, Canberra, ACT 2600, Australia, 2014.

[39] P.M. Prenter. *Splines and Variational Methods*. A Wiley-Interscience publication. Wiley, New York, 1975.

[40] K.E. Atkinson. *An introduction to numerical analysis*. John Wiley & Sons, Canada, 2nd edition, 1989.

[41] P.L. Roe. Characteristic-based schemes for the Euler equations. *Annual Review of Fluid Mechanics*, 18(1):337–365, 1986.

[42] B. Van Leer. Towards the ultimate conservative difference scheme. IV. A new approach to numerical convection. *Journal of Computational Physics*, 23(3):276–299, 1977.

[43] A. Harten. High resolution schemes for hyperbolic conservation laws. *Journal of Computational Physics*, 49(3):357–3935, 1983.

[44] P.J. Davis and P. Rabinowitz. *Methods of Numerical Integration*. Computer science and applied mathematics. Academic Press, London, 2nd edition, 1984.

[45] W.H. Press, S.A. Teukolsky, W.T. Vetterling, and B.P. Flannery. *Numerical Recipes in C*. Cambridge University Press, Melbourne, 2nd edition, 2002.

[46] A. Kurganov, S. Noelle, and G. Petrova. Semidiscrete central-upwind schemes for hyperbolic conservation laws and Hamilton-Jacobi equations. *Journal of Scientific Computing, Society for Industrial and Applied Mathematics*, 23(3):707–740, 2002.

[47] E. Audusse, F. Bouchut, M. Bristeau, R. Klein, and B. Perthame. A fast and stable well–balanced scheme with hydrostatic reconstruction for shallow water flows. *Journal of Scientific Computing, Society for Industrial and Applied Mathematics*, 25(6):2050–2065, 2004.

[48] S. Gottlieb, C. Shu, and E. Tadmor. Strong stability-preserving high-order time discretization methods. *Review, Society for Industrial and Applied Mathematics*, 43(1):89–112, 2001.

[49] R. Courant, K. Friedrichs, and H. Lewy. On the partial difference equations of mathematical physics. *IBM Journal of Research and Development*, 11(2): 215–234, 1967.

[50] A. Kurganov and G. Petrova. A second-order well-balanced positivity preserving central-upwind scheme for the Saint-Venant system. *Communications in Mathematical Sciences*, 5(1):133–160, 2007.

[51] S.D. Conte and C. De Boor. *Elementary numerical analysis: An algorithmic approach*. International Series in Pure and Applied Mathematics. McGraw-Hill Inc., New York, 3rd edition, 1980.

[52] P. Lax and R. Richtmyer. Survey of the stability of linear finite difference equations. *Communications on Pure and Applied Mathematics*, 9(2):267–293, 1956.

[53] A.T. Ippen and G. Kulin. The shoaling and breaking of the solitary wave. *Coastal Engineering Proceedings*, 1(5):4, 1954.

[54] N.J. Higham. *Accuracy and Stability of Numerical Algorithms*. Society for Industrial and Applied Mathematics, Philadelphia, 1996.

[55] J.L. Hammack and H. Segur. The Korteweg-de Vries equation and water waves. Part 3. oscillatory waves. *Journal of Fluid Mechanics*, 84(2):337–358, 1978.

[56] S. Beji and J.A. Battjes. Experimental investigation of wave propagation over a bar. *Coastal Engineering*, 19(1):151–162, 1993.

[57] S. Beji and J.A. Battjes. Numerical simulation of nonlinear wave propagation over a bar. *Coastal Engineering*, 23(1):1–16, 1994.

[58] D. Lannes. *The Water Waves Problem: Mathematical Analysis and Asymptotics*, volume 188 of *Mathematical Surveys and Monographs*. American Mathematical Society, Providence, 2013.

[59] J. Pitt, C. Zoppou, and S.G Roberts. Importance of dispersion for shoaling waves. *Modelling and Simulation Society of Australia and New Zealand*, 22 (1):1725–1730, 2017.

[60] Y. Zhang, A.B. Kennedy, N. Panda, C. Dawson, and J.J. Westerink. Boussinesq-Green-Naghdi rotational water wave theory. *Coastal Engineering*, 73(1):13–27, 2013.

[61] V. Roeber. *Boussinesq-type mode for nearshore wave processes in fringing reef environment*. PhD thesis, Department of Ocean and Resource Engineering, University of Hawaii, Manoa, Honolulu, HI, U.S.A, 2010.

[62] C.E. Synolakis. The runup of solitary waves. *Journal of Fluid Mechanics*, 185:523–545, 1987.

[63] A. Bollermann, S. Noelle, and M. Lukáčová-Medvidová. Finite volume evolution Galerkin methods for the shallow water equations with dry beds. *Communications in Computational Physics*, 10(2):371–404, 2011.